2014

Three-Dimensional Numerical Modeling Of Multiple-Sized Sediment Transport Modeling Under Current And Waves

Qianru Lin
University of Mississippi

THREE-DIMENSIONAL NUMERICAL MODELING OF MULTIPLE-SIZED SEDIMENT TRANSPORT UNDER CURRENT AND WAVES

A Dissertation
presented in partial fulfillment of requirements
for the degree of Doctor of Philosophy
at the National Center for Computational Hydroscience and Engineering
The University of Mississippi

Qianru Lin

September 2014

ABSTRACT

In this study, a three-dimensional numerical model of multiple-sized sediment transport under current and waves is developed. The coastal circulations are described by a three-dimensional hydrodynamic model, which is governed by the three-dimensional phase-averaged shallow water flow equations coupled with wave radiation stresses. Methods are also developed to determine the bed shear stress due to current only, waves only, and coexistence of current and waves, accounting for the nonlinear interaction of the current and waves on bed shear stresses. Meanwhile, empirical formulas for bed-load transport capacity, suspended-load transport capacity, and near-bed suspended-load concentration under current and waves are established for multiple-sized sediments. These formulas are used to close the sediment transport model. The flow and sediment transport equations are solved using a finite volume method on non-staggered grid. The computational mesh is composed of quadtree rectangular grid on the horizontal plane and sigma coordinate in the vertical direction. The SIMPLEC algorithm with Rhie and Chow's momentum interpolation is used to couple the flow velocity and water level. A coupled solution procedure is used to solve the discretized sediment transport, bed change and bed material sorting equations together.

The empirical formulas for bed-load and suspended-load transport rates and the near-bed suspended-load concentration have been tested intensively using a large volume of single- and multiple-sized sediment transport data under current and waves. Statistics show that more than

50% of the cases are predicted within a factor of 2 of the measured values and more than 80% of the cases are within a factor of 5. The hydrodynamic model has been validated using two laboratory cases and two field cases, which demonstrate the reliability of the flow model and its coupling with wave model. The multiple-sized sediment transport sediment transport model has been validated using three laboratory cases and one field case. The predications of the model are in good agreement with the measurements. Sensitivity analyses have also been conducted for the bed friction coefficient, suspended-load scale factor, Schmidt Number, bed-load adaptation length, and roughness height constant. The developed sediment model has been demonstrated its capability of predicting morphologic behavior through the test cases.

DEDICATION

This work is dedicated to my family.

ACKNOWLEDGMENTS

I would like to express my great appreciation to my previous advisor Dr. Weiming Wu, who already left Ole Miss to Clarkson University, for his endless guidance, support, inspiration, and patience during my entire Ph.D. study. I would also sincerely thank my advisor Dr. Mustafa S. Altinakar for his support and advice for this research. My gratitude are extended to my committee**,** Dr. Yafei Jia, Dr. Yan Ding, and Dr. Bing Wei for taking time to offer valuable insight and commentary into this work.

Special thanks to all the members at the National Center for Computational Hydroscience and Engineering for their assistant and friendship.

Finally, I would like to thank my family. This work could not be accomplished without their support and encouragement.

TABLE OF CONTENTS

LIST OF FIGURES

FIGURE PAGE

LIST OF TABLES

TABLES PAGE

CHAPTER I

INTRODUCTION

1.1 Motivations

Coastal and estuarine sediment dynamics, which includes a series of processes such as erosion, deposition, advection and diffusion, is traditionally one of the important engineering problems. The importance has been widely recognized due to 1) the impact of their natural processes on human, including discharge of sediment particles from estuarine runoffs, sediment transportation and dispersion to offshore deep waters, and beach erosion; and 2) increasing utilization of their resources by human, such as dredging of navigation channels and disposal of dredged materials. Therefore, it is of great importance to investigate the sediment dynamics in estuaries and coastal areas and have a better understanding of the sediment transport processes. Accurate predictions of the sediment transport processes are essential for not only assessing the impact of the natural processes on human, but also evaluating the influence of engineering projects on the environment. It is desirable to have the predictions as accurate as possible, which enables the potential for effective environmental management and planning policies to be considered, e.g., implementing the optimal dredging and navigational strategies.

1.2 Objectives of the Study

Physical model is traditionally used to study the coastal and estuarine sediment transport

processes. It is still being used. However, it does have drawbacks, such as high cost, limitations on temporal and spatial scales, difficulty of modifying and duplicating, and, the most serious one, the question of scaling. Computational modeling is clearly an alternative tool to predict the sediment transport in estuaries and coastal areas. Before 1980s, unfortunately, computational modeling was a very complicated task due to theoretical and technical difficulties, e.g., many fundamental questions in this field were unanswered. In recent decades, thanks to the advancement of computation technologies and the improved understanding of current-wave mechanics and sediment transport processes, numerical models have become increasingly attractive. Coastal management and engineering decisions rely heavily on predictions made by computational models of hydrodynamic and sediment-dynamic processes.

The sediment transport in coastal and estuarine waters is dependent on many variables, including waves, current, bottom stresses, turbulent intensity, sediment type, bottom erosion, and sediment settling. The process of advective and diffusive transport is a three-dimensional phenomenon, which should be described using three-dimensional models, although most currently used estuarine and coastal models primarily use a two-dimensional depth-averaged approach, of which the advantage is clearly the computational cost. However, the two-dimensional depth-averaged model precludes direct considerations of some of the important phenomena, such as undertow current and vertical nonuniformity of sediment concentration. Therefore, in order to have a realistic simulation of these complex features, it is required to develop a three-dimensional model. Furthermore, with the computer hardware and computation techniques development, such as multi-cores CPU, parallel computing, and GPU computing, the computational burden associated with the use of three-dimensional models becomes less and less.

Instead of relating the near-bed suspended-load concentration to the depth-averaged concentration in two-dimensional depth-averaged model, the three-dimensional model requires a more appropriate and accurate way of determining near-bed suspended-load concentration to calculate the sediment erosion or deposition. There exist quite a few near-bed concentration relationships in literature, for instance, Smith and McLean (1977), Van Rijn (1984a), Garcia and Parker (1991), and Camenen and Larson (2007), most of which were designed for uniform sediments or suitable for river applications only. As a result, it is necessary to have a reliable formula to predict the near-bed suspended-load concentration for multiple-sized sediment under the interaction of current and waves in a three-dimensional sediment transport model.

In some coastal management and engineering projects, the bed load and suspended load are assumed to instantaneously reach equilibrium state. Consequently, many coastal sediment transport models calculate the transport rate using empirical formulas. The tendency of many empirical formulas of coastal sediment transport, such as Bijker (1968), Van Rijn (1984b, 1993), Bailard (1981), Dibajnia and Watanabe (1992), Ribberink (1998), and Camenen and Larson (2007), is to assume uniform or homogeneous sediments (e.g. a well-sorted fine sand). Very few studies have concerned nonuniform sediment transport in coastal environments. Therefore, it is desirable to develop a reliable formula that can predict the equilibrium transport rate of nonuniform sediments to have a quick assessment for the engineering projects and support of predictive numerical models of morphology change and channel evolution in coastal areas.

In summary, the goal of this study is to develop a three-dimensional numerical model for multiple-sized sediment transport under current and waves. Meanwhile, empirical formulas for bed-load transport capacity, suspended-load transport capacity, and near-bed suspended-load

concentration under current and waves are developed and built into the three-dimensional numerical model.

1.3 Scope of the Study

The complete numerical modeling of sediment transport in coastal and estuarine areas consists of two elements: hydrodynamics and sediment transport. The coastal and estuarine flows can be described by a hydrodynamic model. The effects of the hydrodynamic forcing agents (the current and waves) on sediment dynamics take place primarily through the friction they exert on the bed. This is expressed in terms of bed shear stress. Consequently, for sediment transport, more attention should be paid to the bottom current field. Of particular interest is the bottom shear stress.

In order to achieve the objectives of this study, the following tasks will be carried out:

1) Interaction of the current- and wave-induced bed shear stresses is nonlinear, which is one of the difficult effects to estimate. It is necessary to seek methods to determine the bed shear stress due to current only, waves only, and coexistence of current and waves.

2) Develop sediment transport capacity formulas for bed-load and suspended-load moved by current, or by waves, or very commonly by both current and waves acting together, and propose a formula for estimating the near-bed suspended-load concentration considering the interaction between current and waves. These formulas should be capable of calculating the transport rates of multiple-sized sediment and taking into account the hiding and exposure effects among different sizes classes of sediment particles on the bed. The developed formulas are tested by a larger number of data sets.

3) Describe an implicit three-dimensional shallow water flow model which simulates the

current induced by short waves in coastal water by adopting the three-dimensional phase-averaged shallow water flow equations coupled with wave radiation stresses. Intensively test and verify the hydrodynamic model with laboratory and field measurements.

4) Establish a three-dimensional non-equilibrium sediment transport model to realistically simulate the sediment processes under current and waves. A finite volume method is adopted to solve the sediment transport governing equations. Experimental and field cases are used to verify the model performance.

1.4 Structure of the Dissertation

This dissertation includes six chapters. Chapter I states the motivations and objectives of this study. It also outlines the approaches to achieve the objectives. Chapter II describes the hydrodynamic and sediment transport processes in coastal and estuarine areas and reviews the past studies on numerical modeling of coastal hydrodynamics and sediment transport. Chapter III presents the newly-developed formulas for bed-load transport capacity, suspended-load transport capacity, and near-bed suspended-load concentration under current and waves. Methods to determine the bed shear stresses due to current, waves, or both current and waves are provided in this chapter. In addition, two new approaches to determine the Schmidt number are presented as well. Chapter IV describes and verifies a three-dimensional coastal hydrodynamic model which adopts the three-dimensional phase-averaged shallow water flow equations coupled with wave radiation stresses. Laboratory and field cases are used to test the model. Chapter V establishes a three-dimensional sediment transport model for multiple-sized sediment under current and waves, followed by test cases to demonstrate the model performance. Chapter VI gives conclusions.

CHAPTER II

LITERATURE REVIEW

2.1 Hydrodynamic Processes

The hydrodynamic processes in coastal waters are complex, which include current circulations, tidal currents, wind-induced currents, wave-current interactions, etc. The most important current motions are caused by tides, waves and winds, but the response of coastal waters to these forces varies widely, influenced by climate, geomorphology, and stratification.

Tides are the rise and fall of sea levels caused by the combined effects of the gravitational forces exerted by the Moon and the Sun and the rotation of the Earth. The currents caused by the rise and fall of the water level due to tides are called tidal currents. The tidal currents consist of two parts: a) flood flow, during which the current is coming from the sea to the shore; and b) ebb flow, during which the current is coming from shore and returning to the sea. The impacts of tidal currents on producing the coastal waters periodically in and out of the bay and harbor are crucial.

As the name implies, the wind-induced currents are created by the force of the wind blowing across a water body and hence exerting stress on the sea surface. This stress causes the surface water to move and the movement is transmitted to the underlying water to a depth that is dependent mainly on the strength and persistence of the wind. A wind-driven current does not flow in exactly the same direction as the wind, but is deflected by Earth's rotation, which can be quantitatively defined as Coriolis force, a fictitious force exerted on a body when it moves in a

rotating reference frame. The Coriolis force is greater at high latitudes and more effective in deep water. It is to the right of the wind direction in the Northern Hemisphere and to the left in the Southern Hemisphere.

Wave-current interaction, the interaction between surface gravity waves and a mean flow, is also regarded as one of the important processes in coastal hydrodynamics, particularly in the nearshore regions. It has a crucial impact on the coastal water exchanging, sediment transport, and pollutant diffusion, and shoreline changes. The interaction implies an exchange of energy, which is quantitatively described as radiation stress. Radiation stress is the excess shoreward directed momentum flux caused by the presence of the surface gravity waves. It describes the additional force due to the waves, which changes momentum in the fluid layer. As waves travel from deep water to shallow water, the combination effect of refraction, diffraction, shoaling, and breaking will take place, and the wave-induced nearshore currents will be formed and developed when waves break strongly in surf zones accordingly.

Attentions and interests have been greatly increased on the complex hydrodynamic processes since they are very essential to the coastal engineering and environment protecting, e.g. planning and monitoring of coastal construction activities, resource exploration, disposal of industrial and domestic waste water, dumping of dredged materials, etc. It is necessary to better understand and improve the prediction of the hydrodynamics processes to avoid a drastic impact on the environment. Therefore, coastal management and engineering decisions require a numerical model constructed with proper governing equations that can provide a realistic simulation and prediction of the hydrodynamics in coastal area.

The numerical models can be classified to three categories: one-dimensional (1-D), two-dimensional (2-D), and three-dimensional (3-D) models. The applications of 1-D models are focused on solving problems in lonshore direction, without considering the details over the cross-shore. A 2-D model is usually depth-averaged, which describes the flow in horizontal plane assuming vertical distributions in the vertical direction are uniform. Application examples are tidal flow in well-mixed estuaries and in seas, and wind-driven circulation in shallow lakes (Van Rijn 1993). Engineering projects sometimes involve flow field with significant variation in vertical direction, while the flow pattern in horizontal plane is also of great importance. Examples are salt intrusion in estuaries, fresh water discharges in bays, thermal stratification in lakes and seas, wind-driven circulations in lakes, seas, and oceans, flow near structures, etc. Even though depth-averaged 2-D models have been widely used with certain success, realistic simulation of these complex features requires a 3-D model, which can be based on the full 3-D Navier-Stokes equations or their simplification with shallow water assumption. The depth-averaged 2-D models and 3-D models are briefly discussed in the following sections.

2.1.1 Depth-averaged 2-D Hydrodynamic Models

The depth-averaged 2-D models are particularly useful for situations where the flow field shows no significant variation in vertical direction and where the fluid density is constant. The governing equations of a depth-averaged 2-D model are

$$\frac{\partial h}{\partial t}+\frac{\partial\left(hU_x\right)}{\partial x}+\frac{\partial\left(hU_y\right)}{\partial y}=0 \tag{2.1}$$

$$\frac{\partial(hU_x)}{\partial t}+\frac{\partial\left(hU_x^2\right)}{\partial x}+\frac{\partial\left(hU_xU_y\right)}{\partial y}=-gh\frac{\partial z_s}{\partial x}+\frac{1}{\rho}\frac{\partial(hT_{xx})}{\partial x}+\frac{1}{\rho}\frac{\partial\left(hT_{xy}\right)}{\partial y}+\frac{1}{\rho}(\tau_{sx}-\tau_{bx})+f_chU_y \tag{2.2}$$

$$\frac{\partial\left(hU_y\right)}{\partial t}+\frac{\partial\left(hU_xU_y\right)}{\partial x}+\frac{\partial\left(hU_y^2\right)}{\partial y}=-gh\frac{\partial z_s}{\partial y}+\frac{1}{\rho}\frac{\partial\left(hT_{yx}\right)}{\partial x}+\frac{1}{\rho}\frac{\partial\left(hT_{yy}\right)}{\partial y}+\frac{1}{\rho}\left(\tau_{sy}-\tau_{by}\right)-f_chU_x \tag{2.3}$$

where t is the time; x and y are the horizontal coordinates; h is the local water depth; U_x and U_y are the depth-averaged flow velocities in x, y directions; ρ is the fluid density; T_{ij} (i, j = x, y) are the stresses, which include both viscous and turbulent effects; τ_{sx} and τ_{sy} are the forces acting on the water surface in x, y directions, which can be wave radiation stresses, wind driving forces, or the combination of both; τ_{bx} and τ_{by} are the bed shear stresses in x, y directions; f_c is the Coriolis force coefficient. Eq. (2.1) is the mass balance equation. Eqs. (2.2) and (2.3) are the momentum balance equations in x, y directions, respectively.

Walters and Cheng (1979) developed a finite element 2-D depth-averaged hydrodynamic model which computes the tidal and residual currents in an estuary. FESWMS (Finite Element Surface Water Modeling System) is another finite element hydrodynamic model that simulates two-dimensional, depth-integrated, steady or unsteady surface-water flow in rivers, lakes, estuaries, reservoirs, and coastal areas. It supports both super and subcritical flow analyses, and area wetting and drying (Froehlich 1989). MIKE 21, developed by Danish Hydraulic Institute (DHI), is one of the popular modeling systems for 2-D free-surface flows in lakes, estuaries, bays, coastal areas, and seas where stratification can be neglected. It can be applied to a wide range of

hydraulic phenomena, including tidal currents, storm surges, secondary circulations (eddies and vortices), dam-breaks, and tsunamis (DHI, 2007a). Wu et al. (2011) proposed an implicit finite-volume flow model, which computes the depth-averaged 2-D shallow water flow, accounting for the effects of wave radiation stresses and turbulent diffusion induced by currents, waves, and wave breaking.

2.1.2 3-D Hydrodynamic Models

3-D models once are considered as impractical in the economic view. However, with the computer hardware and computational techniques development, for instance, multi-cores CPU, parallel computing, GPU computing, etc., the computational burden associated with the use of 3-D models becomes much less. Therefore, the developments and applications of 3-D hydrodynamic models increase rapidly. In 3-D models, the flow field is determined by the Reynolds-averaged continuity Eq. (2.4) and Navier-Stokes equations Eq. (2.5), which are written as follows:

$$\frac{\partial u_i}{\partial x_i} = 0 \tag{2.4}$$

$$\frac{\partial u_i}{\partial t} + \frac{\partial \left(u_i u_j \right)}{\partial x_j} = F_i - \frac{1}{\rho}\frac{\partial p}{\partial x_i} + \frac{1}{\rho}\frac{\partial \tau_{ij}}{\partial x_j} \tag{2.5}$$

where u_i (i = 1, 2, 3) are the components of mean flow velocity; F_i are the components of external forces, such as gravity and Coriolic force, per unit volume; p is the mean pressure; and τ_{ij} are the stresses, including both viscous and turbulent effects.

However, solving the 3-D Navier-Stokes equations to compute the long and short waves or current and waves together in detail is very time-consuming and impractical in the time being,

even with the ever-increasing capacity of computing technologies. The often used alternative approach is the phase-averaged model in which only the long wave or current is simulated using a phase-averaged 3-D shallow water flow equations that include the radiation stresses generated by short waves. The short wave characteristics and radiation stresses are determined by a spectral wave model that solves the wave action balance equation. This phase-averaged modeling approach can be much cheaper than the full 3-D model solving the Navier-Stokes equations.

CH3D-WES (Curvilinear Hydrodynamics in 3-Dimensions - Waterways Experiment Station) is a time-varying 3-D numerical hydrodynamic model developed in 1996. It makes hydrodynamic computations on a curvilinear or boundary-fitted planform grid. Physical processes impacting circulation and vertical mixing that are modeled include tides, wind, density effects (salinity and temperature), freshwater inflows, turbulence, and the effect of the earth's rotation (Chapman et al. 1996). DHI also developed a hydrodynamic model MIKE 3 which solves the Reynolds-averaged Navier-Stokes equations and are suitable for studying phenomena like tidal flows, storm surges, wave-driven flows, oceanographic circulations, and density-driven flows. The user can choose between a hydrostatic pressure assumption and a generalized sigma coordinate transformation, and a non-hydrostatic pressure formulation and a z-level coordinate formulation (DHI 2007b). Chen et al. (2003) proposed an unstructured grid, finite-volume, 3-D primitive equation ocean model for studying the coastal oceanic and estuarine circulations. The model consists of momentum, continuity, temperature, salinity, and density equations and is closed physically and mathematically using the Mellor and Yamada leve-2.5 turbulent closure submodel. The irregular bottom slope is represented using a σ-coordinate transformation and the horizontal grids comprise unstructured triangular cells. ROMS (Regional Ocean Modeling

System) is a 3-D, free surface, terrain-following numerical model that solves finite-difference approximations of Reynolds-averaged Navier-Stokes equation using the hydrostatic and Boussinesq assumptions (Chassignet et al. 2000, Haidvogel et al. 2000). Warner et al. (2008) modified it to include physical processes that are important in nearshore regions by adding 3-D radiation-stress terms in the momentum equations based on Mellor (2003, 2005), along with effects of a surface wave roller model. The modified ROMS model is applicable for fluvial, estuaries, shelf, and nearshore environments. Delft3D-FLOW, developed by Delft Hydraulics (2010), is 3-D hydrodynamic simulation program which calculates unsteady flow phenomena that result from tidal and meteorological forcing on a rectilinear or a curvilinear, boundary fitted grid. The hydrodynamic conditions calculated in the Delft3D-FLOW can be used as input to the other modules of Delft3D suite to carry out simulations of flows, sediment transport, waves, water quality, morphological development, and ecology in river, estuarine, and coastal areas.

2.1.3 Wave Radiation Stress

In a coastal circulation model, wave-current interaction is necessary to be considered in the hydrodynamic processes. Mathematically, an additional force due to waves should be introduced into the momentum equations. This momentum flux, referred to radiation stress, has been studied by Longuet-Higgins and Stewart (1964) (LHS), which is a vertically integrated formula, successfully explain the wave setup and setdown inside and outside the surface zone. The development of this concept provided a better understanding of wave-induced circulation. With the additional force due to waves, the momentum equation (2.5) is written as

$$\frac{\partial u_i}{\partial t} + \frac{\partial \left(u_i u_j \right)}{\partial x_j} = F_i - \frac{1}{\rho}\frac{\partial p}{\partial x_i} + \frac{1}{\rho}\frac{\partial \tau_{ij}}{\partial xj} - \frac{1}{\rho}\frac{\partial S_{ij}}{\partial x_i} \tag{2.6}$$

where the extra term S_{ij} added to the right hand side is the radiation stress. Recent studies have used 3-D circulation models and LHS to study wave-induced circulation and obtained vertically varying currents, eddy coefficients, and reasonably accurate wave-induced circulation (Xie et al 2001, Sheng and Alymov 2002, Sheng et al. 2010a and 2010b). Mellor (2003 and 2008) and Xia et al (2004) questioned the accuracy of the vertically uniform LHS and developed depth-dependent radiation stress formulations: M03 (Mellor 2003), X04 (Xia et al 2004), and M08 (Mellor 2008), which are based on linear wave theory. Both M03 and M08 consider the wave effects on three-dimensional questions of motion. M03 contains error and fails to produce radiation stress of LHS when vertically integrated (Ardhuim et al 2008). Later Mellor (2008) revised the formula and proposed M08, whose vertically integrated form is consistent with LHS. Xia et al (2004) developed a depth-dependent radiation stress (X04) by a simplistic approach which invokes the small amplitude approximation in part of the LHS to allow interchange of the time integration and vertical integration.

2.2 Sediment Transport Processes

In recent years, there has been a growing interest in the sediment transport processes involved in estuarine and coastal water management, including erosion, deposition, advective and diffusive transport, long term geomorphological processes, estuarine and coastal inlet stability, and transport of heavy metals and toxic waste via adsorption of contaminants on sediment particles. The various physical processes that can affect the distribution of sediment in a coastal

environment are shown in Fig. 2.1. In a river, the driving force of the sediment movement is the flow itself. In the nearshore region, however, the driving forces are not only currents but waves as well. Transporting mechanisms such as wave breaking, onshore or offshore currents in the vicinity of sea bottom and oscillatory fluid motion in the swash zone are characteristics of the coastal region. Therefore, estuarine and coastal sediment dynamics is very complex and quantitative understanding of these various processes is crucial to coastal engineering projects and management.

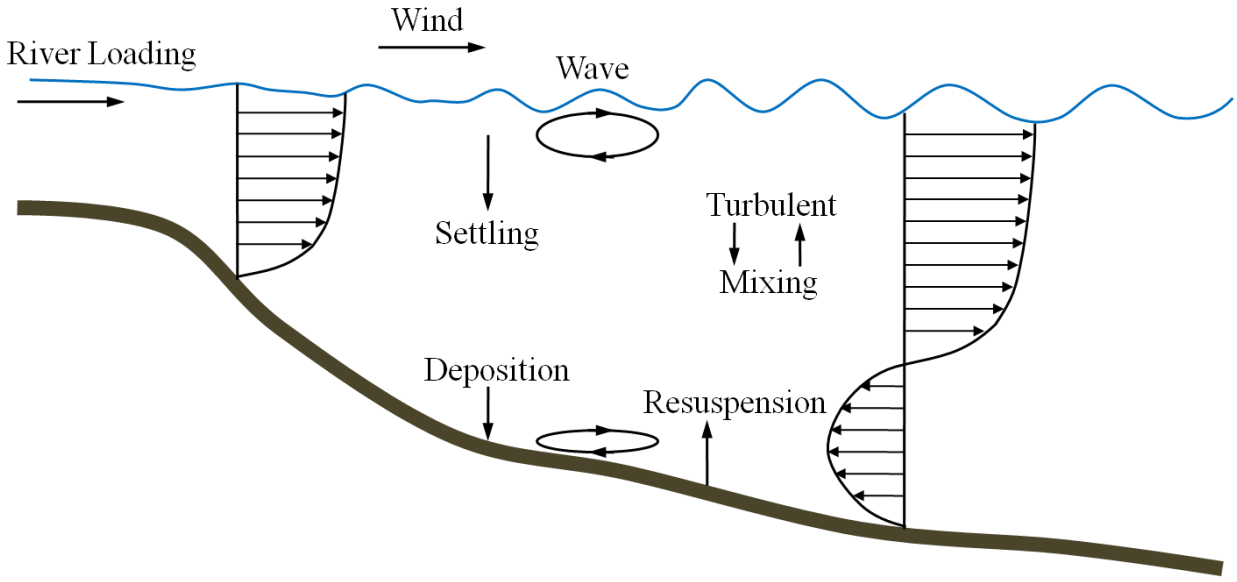

Figure 2.1 Schematics of Dominant Mechanisms Affecting Sediment Distribution in Shallow Coastal Waters (after Sheng and Bulter 1982)

In the coexistence of waves and currents, the bed shear stress is contributed by wave-related and current-related bed shear stresses and the combination of two is not in a simple linear relation. It has been shown that wave motion can generate sediment suspensions with large

concentrations in the near-bed region. The basic mechanism is the entrainment of particles by the stirring wave action and the transport of particles by the current motion. The transport of bed material particles can be in the form of bed-load and suspended load, depending on the size of the bed material particles and the hydrodynamic conditions. The suspended load may also contain some wash load which is governed by the upstream supply other than the composition and properties of the bed material. When the value of the bed-shear velocity just exceeds the critical value for initiation of motion, the particles will be rolling and sliding or both in continuous contact with bed. For increasing the values of the bed-shear velocity, the particles will be moving along the bed by more or less regular jumps, which are called saltations. When the values of the bed-shear velocity exceeds the settling velocity of the particles, the sediment particles can be lifted to a level at which the upward turbulent forces will be comparable with or of higher order than the submerged weight of the particles and as results the particles may go in suspension (Van Rijn 1993). The sediment transport capacity or the capacity of flow-carrying sediment is defined as the quantity of sediment that can be carried by the flow without net erosion or deposition at an equilibrium state in a steady, uniform flow. In such case, the sediment transport rate is a function of flow conditions and sediment properties and can be estimated by various empirical formulas in literature (Wu 2007). The empirical sediment transport capacity formulas are reviewed in Section 2.3. However, in conditions of unsteady and non-uniform flow, the actual sediment transport rate may be smaller or larger than the transport capacity resulting in net erosion or deposition assuming sufficient availability of bed-material. The bed-load transport in unsteady and non-uniform flow can be modeled by a formula type of approach because the adjustment of the transport of sediment particles close to the bed proceeds rapidly to the new hydraulic conditions. Suspended load

transport, however, does not have such a behavior because it takes time to transport the particles upward and downward over the depth and therefore it is necessary to model the vertical convection-diffusion process (Van Rijn 1993). Therefore, the modeling of sediment transport rate under unsteady and non-uniform flow conditions is necessary to provide prediction with sufficient accuracy.

Numerous models of varying complexity aim to describe sediment processes in coastal regions. From the dimensional viewpoint, the sediment models are simply categorized into 1-D, 2-D, and 3-D models. Even though 1-D models are sometimes used for longshore sediment transport, most of the widely used coastal models are primarily 2-D depth-averaged and 3-D.

2.2.1 2-D Depth-averaged Sediment Transport Model

The 2-D depth-averaged models solve the depth-averaged sediment transport equations to describe the governing suspended sediment transport processes. In 2-D depth-averaged sediment transport model, the near-bed suspended sediment concentration, which is required to compute sediment deposition rate, can be related to the depth-averaged concentration by analytical relationships for the equilibrium (steady-state) vertical concentration profiles (O'Connor and Nicholson 1988). Therefore, a depth-averaged 2-D model can adequately reproduce the erosion and deposition processes in many situations and it is still very useful for many practical engineering applications due to less requirements of data and computer resources in comparison with a 3-D model.

The governing equation of 2-D depth-averaged sediment transport model is

$$\frac{\partial}{\partial t}\left(\frac{hc_k}{\beta_{sk}}\right)+\frac{\partial\left(hU_x c_k\right)}{\partial x}+\frac{\partial\left(hU_y c_k\right)}{\partial y}=\frac{\partial}{\partial x}\left(E_{s,x}h\frac{\partial c_k}{\partial x}\right)+\frac{\partial}{\partial y}\left(E_{s,y}h\frac{\partial c_k}{\partial y}\right)+\alpha\omega_{sk}\left(c_{*k}-c_k\right)\quad\left(k=1,2,...,N\right) \tag{2.7}$$

where c_k and c_{*k} are the actual and equilibrium concentrations of the kth size class of the suspended load, respectively; ω_{sk} is settling velocity of the kth size class of the sediment particle; $E_{s,x}$ and $E_{s,y}$ are the horizontal effective diffusion (mixing) coefficients of sediment in x, y directions, respectively; α is the adaptation or recovery coefficient; β_{sk} is a correction factor for suspended load:

$$\beta_{sk}=\int_{z_b+\delta}^{\bar{\eta}}uc_k dz\Big/\left(U\int_{z_b+\delta}^{\bar{\eta}}c_k dz\right)\quad\left(k=1,2,...,N\right) \tag{2.8}$$

where $\bar{\eta}$ is the water surface elevation; z_b is the bed elevation, and δ is the thickness of the bed-load zone.

Ariathurai (1974) developed a 2-D finite element sediment transport model for both cohesive and non-cohesive sediments. Hayter and Mehta (1986) developed a finite element cohesive sediment transport model (CSTM-H), which is a depth-averaged 2-D model using the Galerkin weighted residual numerical scheme. Andersen et al. (1988) presented a 2-D morphological model for coastal waters, where the sediment transport is computed by a formula taking into account the effect of waves. Letter et al. (1998) developed a 2-D finite element model for depth-averaged sediment transport in rivers, lakes, reservoirs, estuaries, and coastal areas. Cookman and Flemings (2001) developed a 2-D sediment transport model for steady-state, wind- and wave-driven coastal circulation model. Ding et al. (2004) introduced the formulations of sediment transport rate under combination of wave and current to the CCHE2D-Coast, which is

based on a non-orthogonal mesh system, to simulate the sediment transport and seabed morphological changes in different coasts with complex bathymetries and shorelines. Sanchez and Wu (2011) developed a depth-averaged sediment transport model with emphasis on morphodynamic processes near coastal inlets and navigation channels. The model solves the depth-averaged two-dimensional non-equilibrium transport equation of total-load sediment, considering bed-material hiding and exposure, avalanching and sediment transport over hard bottoms.

2.2.2 3-D Sediment Transport Model

The accuracy of 2-D sediment transport models may not be sufficient for siltation and erosion quantities in situations dominated by 3-D flow patterns, such as in harbor entrances due to flow separation, near-shore wave-induced currents, wind and density currents (O'Connor and Nicholson 1988). In addition, one should notice some disadvantages of 2-D models, such as approximation of the near-bed suspended sediment concentration. Consequently, a 3-D sediment transport model, which solves the complete 3-D advection-diffusion equation for suspended sediment concentration, is generally desirable from a physics point of view. In 3-D models, both the horizontal and vertical components of the sediment transport processes are considered.

The governing equations of the 3-D sediment transport model is

$$\frac{\partial c_k}{\partial t}+\frac{\partial\left[\left(u_i-\omega_{sk}\delta_{i3}\right)c_k\right]}{\partial x_i}=\frac{\partial}{\partial x_i}\left(\varepsilon_s\frac{\partial c_k}{\partial x_i}\right)\quad\left(k=1,2,...,N\right) \tag{2.9}$$

where δ_{i3} is the Kronecker delta and ε_s is the turbulent diffusivity of sediment.

An early 3-D model of suspended sediment transport, based on a probabilistic approach

was developed by Chiu (1967) but the verification tests indicated that large computer operating requirements render this type of scheme uneconomical at that time. Later, Wechsler and Cogley (1977) established a 3-D model with a mixed analytical and finite difference approach. Van Rijn (1987) developed a 3-D mathematical model (SUTRENCH-3D) to study the morphological processes in case of suspended sediment transport. O'Conner and Nicholson (1988) developed a 3-D sediment transport model which is based on a splitting technique and a mixed characteristics and finite difference approach. Wu et al. (2000a) developed a 3-D numerical model for sediment transport model in open channel. In this model, the suspended-load transport is simulated through the general convection-diffusion equation with an empirical settling-velocity term, bed-load transport is simulated with a nonequilibrium method and the bed deformation is obtained from an overall mass-balance equation. Olsen (2003) proposed a 3-D CFD model to compute the formation of the meandering pattern in an initially straight alluvial channel. The sediment transport was computed as bed load in addition to solving the convection-diffusion equation for suspended sediment transport. The bed changes were calculated and the grid was altered during the computation as channel erosion and deposition caused wetting and drying. Examples of some of the most widely used 3-D models are: NOPP community sediment transport model, a 3-D model implements algorithms for an unlimited number of user-defined sediment classes and for the evolution of the bed morphology. It is incorporated in a ROMS with a two-way coupling between a wave model and the sediment transport module (Warner et al. 2008); DELFT3D, a sediment module implements algorithms for up to five different classes, which have to be specified as either mud or sand (Van Rijn and Walstra 2003); and ECOM-SED, a model commercialized by Hydroqual (Hydroqual 2002) aiming to model sediment transport for both cohesive and

non-cohesive sediments, however, only two size classes of each are allowed.

2.3 Formulas for Sediment Transport Rate under Current and Waves

2.3.1 Bed-load Sediment Transport Rate

In general, there exist two main approaches for calculating the bed-load sediment transport capacity. The first one is called “stochastic concepts” proposed by Einstein (1942), who carefully observed the motion of sand particles under unidirectional flow and found that a specific sand particle entrained or picked up by the flow remained in motion for a certain distance defined stochastically, stopped to reside on the bottom for a certain period, and then repeated the “pick-up” and “reside” process. Based on this observation he concluded that the pick-up rate of sand particles is closely related to the time period during which the lift force acting on the particle is greater than its immersed weight and introduced a well-known formula for calculating sediment transport under unidirectional flow. However, the transport of sediment particles is very complex, not only affected by the pick-up rate of a particle as introduced by Einstein (1942), but also based on many additional hypotheses. As a result, this approach has barely been applied to estimate the sediment transport rate in coastal area.

Later after Einstein (1942), Bagnold (1963) suggested a different approach that the sediment transport rate is closely related to the fluid energy, or power, generated by the fluid motion in the vicinity of the bed. Thus, this concept is called “power model”, which assumes that the number of sediment particles in motion is related to the bottom shear stress and that the particles move at a certain speed according to the flow. This approach is conceptually and mathematically simpler than the stochastic approach, and several sediment transport formulas

(Dou 1964, Yalin 1972, Van Rijn 1984a, and Wu 2000b) developed so far have been based on the power model. In addition, many formulas developed to calculate the bed-load sediment transport rate under coexistence of current and waves are related to the bottom bed shear stress. Several bed-load sediment transport formulas that consider both current and wave effects are described below.

Based on Bagnold's (1966) energetics-based sediment transport model for streams, Bailard and Inman (1981) derived a formula for the time-varying transport of bed load over a plane sloping bed. It can take into account the effect of the instantaneous velocity profile from current and waves combined. The formula can be written as

$$\vec{q}_{sb} = \frac{1}{2}\frac{f_{cw}}{g(s-1)}\frac{\varepsilon_b}{\tan\varphi}\left\langle |\vec{u}|^2 \vec{u} \right\rangle \tag{2.10}$$

where $\vec{q}_{sb}$ is the volumetric bed-load sediment transport rate; s is the specific gravity of sediment; $\vec{u}$ is the instantaneous velocity vector; ε is the angel between wave and current directions; ε_b is the bed-load efficiency; and < > represents the average overall several wave periods.

Dibajnia and Watanabe (1992) established a transport rate formula to calculate sheet sand transport rate under asymmetric oscillations and superimposed steady current. The formula divides the sediment transport into two half-cycles due to the presence of waves. During the first half-cycle, sediment moves in the direction of wave propagation, and then it moves in the opposite direction during the second half-cycle. An advantage of the formula is that it takes into account a possible quantity of sand still in suspension after each half-cycle that moves in the opposite direction, which is referred to as a "phase leg". The volumetric sediment transport rate is given as

$$\vec{q}_{sb} = 0.001\omega_s d \frac{\vec{\Gamma}}{\Gamma}\Gamma^{0.55} \tag{2.11}$$

where Γ is a parameter defined as

$$\Gamma = \frac{u_c T_c \left(\Omega_c^3 + \Omega_t'^3\right) - u_t T_t \left(\Omega_t^3 + \Omega_c'^3\right)}{\left(u_c + u_t\right) T} \tag{2.12}$$

where the subscript *c* and *t* represent the first (crest) and second (trough) wave cycles, respectively; *u* is the equivalent sinusoidal velocity amplitude; *T* is the wave period; Ω represents the amount of sand entrained and settled during the half-period; and Ω' represents the amount of suspended sand remaining from one half cycle to the next half cycle. The following relations are used to estimate the values of Ω and Ω':

$$\begin{cases} \text{if } \omega_c \le 1 \begin{cases} \Omega_c = \omega_c \dfrac{\omega_s T_c}{d} \\ \Omega_c' = 0 \end{cases} \\ \text{if } \omega_c > 1 \begin{cases} \Omega_c = \dfrac{\omega_s T_c}{d} \\ \Omega_c' = \left(\omega_c - 1\right)\dfrac{\omega_s T_c}{d} \end{cases} \\ \text{if } \omega_t \le 1 \begin{cases} \Omega_t = \omega_t \dfrac{\omega_s T_t}{d} \\ \Omega_t' = 0 \end{cases} \\ \text{if } \omega_t > 1 \begin{cases} \Omega_t = \dfrac{\omega_s T_t}{d} \\ \Omega_t' = \left(\omega_t - 1\right)\dfrac{\omega_s T_t}{d} \end{cases} \end{cases} \tag{2.13}$$

where ω_c and ω_t are defined as

$$\omega_j = \frac{1}{2}\frac{u_j^2}{sg\omega_s T_j} \quad \left(j = c \text{ or } t\right) \tag{2.14}$$

Dibajnia and Watanabe (1996) extended their bed-load transport rate formula (Dibajnia and Watanabe 1992) to mixed sand transport. The extended formula has been verified by using sand mixture composed of a find sand with media diameter of 0.2 mm and a coarse sand with median diameter of 0.87 mm. In the extended formula, Eq. (2.14) above was modified as

$$\omega_j = \frac{1}{2}\frac{u_j^2}{sg\omega_s T_j} \mathrm{p}_{bk}{}^{1/\alpha_k} \quad \left(j = c \text{ or } t\right) \tag{2.15}$$

where p_{bk} is the fraction of the kth size class in the sediment and a_k is empirical parameter depending on the ratio of the mean diameter of the kth size class of sediment particle to that of the other size classes.

Ribberink (1998) proposed a bed-load transport formula for steady unidirectional flows, oscillatory flows, and oscillatory flows with superimposed net current. The formula assumes the instantaneous solid flux is a function of the difference between the actual time-dependent bed shear stress and the critical bed shear stress. It has been tested over 150 laboratory experiments including more than 75 bed-load transport measurements in oscillating water tunnels. The Ribberink (1998) formula is written as

$$\vec{q}_{sb} = 11\sqrt{(s-1)gd^3}\left\langle \left(\left|\vec{\theta}(t)\right| - \theta_{cr}\right)^{1.65} \frac{\vec{\theta}(t)}{\left|\vec{\theta}(t)\right|} \right\rangle \tag{2.16}$$

where $\vec{\theta}(t) = 0.5 f_{cw} \left|\vec{u}(t)\right| \vec{u}(t) / \left[(s-1)gd\right]$ is the time-dependent Shields parameter and θ_{cr} is the critical Shields parameter.

Hassan et al. (2001) applied Ribberink's (1998) bed-load transport formula to calculate the transport rate of nonuniform material under oscillatory sheet-flow with considering the hiding and exposure effects. Comparing the experimental results with the predicted values, they found that the

formula led to better prediction by multiplying the Shields parameter in Eq. (2.16) by a hiding/exposure correction factor ξ_{eff} of Day (1980):

$$\xi_{eff} = \left[\frac{0.4}{\left(d_k / d_A \right)} \right] \quad \text{and} \quad \frac{d_A}{d_{50}} = 1.6 \left(\frac{d_{84}}{d_{16}} \right) \tag{2.17}$$

Van Rijn (2007a) extended a bed-load transport formula in steady river flow to coastal flow applying an intrawave approach together with a method to predict bed roughness under current and waves. The formula is expressed as

$$q_{sb} = 0.5 \rho_s f_{silt} d_{50} D_*^{-0.3} \left(\tau'_{b,cw} / \rho \right)^{0.5} \left(\frac{\tau'_{b,cw} - \tau_{b,cr}}{\tau_{b,cr}} \right) \tag{2.18}$$

where $\tau'_{b,cw}$ is the instantaneous grain-related bed shear stress due to both current and wave; $\tau_{b,cr}$ is the critical bed shear stress according to the Shields; $D_* = d_{50} \left[\left(s-1 \right) g / \nu^2 \right]^{1/3}$ is the dimensionless particle size; ν is the kinematic viscosity coefficient; and $f_{silt} = d_{sand} / d_{50}$ is the silt factor with $f_{silt} = 1$ for $d_{50} > d_{sand}$. Van Rijn (2007c) also investigated four methods to take into account the hiding and exposure effect over graded bed in river and coastal flows, in which the dimensionless bed shear stress parameter T_τ, defined as $T_\tau = \left(\theta' - \theta_{cr} \right) / \theta_{cr} = \left(\tau'_b - \tau_{b,cr} \right) / \tau_{b,cr}$ for uniform sediment, is modified. Thus, the bed-load transport formula is capable to apply for nonuniform sediment transport in both river and coastal flows with the following four approaches:

$$\begin{aligned}
&\text{Method A:} \quad T_{\tau,k} = \lambda_k \left[\tau'_b - \xi_k \left(d_k / d_{50} \right) \tau_{b,cr,d_{50}} \right] / \left(d_k / d_{50} \right) \tau_{b,cr,d_{50}} \\
&\text{Method B:} \quad T_{\tau,k} = \left[\theta'_k - \xi_k \theta_{cr,d_{50}} \right] / \theta_{cr,d_{50}} \\
&\text{Method C:} \quad T_{\tau,k} = \left[\theta'_k - \xi_k \theta_{cr,d_k} \right] / \theta_{cr,d_k} \\
&\text{Method B:} \quad T_{\tau,k} = \left[\theta'_k - \theta_{cr,d_k} \right] / \theta_{cr,d_k}
\end{aligned} \tag{2.19}$$

where τ_b' is the effective bed shear stress due to current and waves; $\tau_{b,cr,d_{50}}$ is the critical shear stresses based on d_{50}; $\theta_k' = \tau_b' / \left[(\rho_s - \rho) g d_k \right]$ and $\theta_{cr,d_k}' = \tau_{b,cr,d_k}' / \left[(\rho_s - \rho) g d_k \right]$ are the effective mobility parameters based on d_k, respectively; $\xi_k = \left[\log(19) / \log(19 d_k / d_{50}) \right]^2$ is the hiding-exposure factor according to Egiazaraoff (1965); $\lambda_k = (d_k / d_{50})^{0.25}$ is the correction factor of effective grain shear stress. Method B is similar to Method A but the λ correction is not applied. Method C is based on the fraction diameters without roughness correction. Method D is also based on the fraction diameters, but no correction is applied.

Camenen and Larson (2007) developed a formula for bed-load transport under coexistence of current and waves based on the Meyer-Peter and Muller (1948) formula. The developed formula has been validated against a large set of data of uniform sediment under current only, waves only, and coexistence of current and waves. The Camenen and Larson (2007) bed-load formula is expressed as follows:

$$q_{sb} = a_w \sqrt{(s-1) g d_{50}^3} \frac{\theta_{cw,net}}{\sqrt{|\theta_{cw,net}|}} \theta_{cw,m} \exp\left(-b \frac{\theta_{cr}}{\theta_{cw}} \right) \tag{2.20}$$

where a_w and b are empirical coefficients; $\theta_{cw,net}$, $\theta_{cw,m}$, and θ_{cw} are the net, mean, and maximum Shields parameters due to wave-current interaction, respectively. The detailed methods to calculated $\theta_{cw,net}$, $\theta_{cw,m}$, and θ_{cw} can be referred to the original publication.

Most recently, van der A et al. (2013) developed a sand transport formula for non-breaking waves and currents. The formula is especially developed for cross-shore sand transport under wave-dominated conditions and is based on the semi-unsteady, half wave-cycle concept, with bed shear stress as the main forcing parameter. It also takes account into the unsteady phase-lag

between velocities and concentrations and the effect on the net transport rate related to flow acceleration skewness. The van der A et al. (2013) formula is written as,

$$\vec{\Phi} = \frac{\vec{q}_{sb}}{\sqrt{(s-1)gd_{50}^3}} = \frac{\sqrt{|\theta_c|}T_c\left(\Omega_{cc} + \frac{T_c}{2T_{cu}}\Omega_{tc}\right)\frac{\vec{\theta}_c}{|\theta_c|} + \sqrt{|\theta_t|}T_t\left(\Omega_{tt} + \frac{T_t}{2T_{tu}}\Omega_{ct}\right)\frac{\vec{\theta}_t}{|\theta_t|}}{T} \tag{2.21}$$

where $\vec{\theta}$ is the Shields parameter with the subscripts "*c*" and "*t*" implying the "crest" and "trough" half cycle respectively; T_{cu} and T_{tu} are the durations of accelerating flow within the crest and trough half cycles, respectively; Ω_{cc} represents the sand load that is entrained during the wave crest period and transported during the crest period; Ω_{tc} represents the sand load that is entrained during the wave crest period and transported during the trough period; Ω_{tt} represents the sand load that is entrained during the wave trough period and transported during the trough period; and Ω_{tc} represents the sand load that is entrained during the wave trough period and transported during the crest period. The details of calculating Ω_{cc}, Ω_{tc}, Ω_{tt}, and Ω_{tc} can be referred to van der A et al. (2013). The net bed load transport rate for graded sand conditions is calculated as follows:

$$\vec{\Phi} = \frac{\vec{q}_{sb}}{\sqrt{(s-1)gd_{50}^3}} = \sum_{k=1}^{N} p_{bk}\frac{\vec{q}_{sb,k}}{\sqrt{(s-1)gd_k^3}} \tag{2.22}$$

The correction factor $\lambda_k = (d_k / d_{50})^{0.25}$ defined by van Rijn (2007c) is applied to the effective Shields parameter to account for the hiding and exposure effect among different size fractions.

2.3.2 Suspended-load Sediment Transport Rate

Similar to bed-load transport formulas, some of the suspended-load formulas are based on the "power model" proposed by Bagnold (1966). Using the concept of "power model" as for the

bed-load transport, Bailard (1981) proposed a formula for suspended load under coexistence of current and waves

$$\vec{q}_{sb} = \frac{1}{2}\frac{f_{cw}}{g(s-1)}\frac{\varepsilon_s}{\omega_s}\left\langle |\vec{u}|^3 \vec{u} \right\rangle \tag{2.23}$$

where ε_s is the suspended load efficiency.

In addition to "power concept", if one assumes the suspended particles move at the same speed as the fluid, the suspended-load sediment transport rate can be evaluated by integrating the product between vertical distributions of the suspended sediment concentration and velocity. In order to obtain the solution of the suspended sediment transport rate, the sediment concentration at a certain reference level must be specified. This sediment concentration is called reference concentration or near-bed suspended-load concentration. The vertical distributions of velocity and suspended-load concentration are also needed to specify in order to calculate the suspended-load transport rate.

2.3.2.1 Vertical Distribution of Velocity

In the presence of current only, the vertical distribution of current velocity can be approximated by two common methods. One is the power-law distribution of velocity,

$$u(z) = \frac{m+1}{m}\left(\frac{z}{h}\right)^{1/m} U_c \tag{2.24}$$

where z is the vertical coordinate above the bed, U_c is the depth-averaged current velocity and m is empirical coefficient with a value of 6 (Shamov 1959) or 7 (Zhang 1961). The other approach is the logarithmic distribution of velocity,

$$u(z) = \frac{U_*}{\kappa} \ln\left(\frac{z}{z_0}\right) \tag{2.25}$$

where U_* is the bed shear velocity, κ is the constant of Von Karman with a value of 0.4, z_o is the zero-velocity level at which u = 0.

Nikuradse (1993) found that the logarithmic velocity profile over a bed of closely packed spheres of diameter d goes through zero at $z_0 = d/30$. Based on this observation, Nielsen (1992) defined the equivalent Nikuradse bed roughness as $k_s = 30z_0$. Applying the Nikuradse bed roughness, logarithmic velocity profile Eq. (2.25) can also be written as

$$u(z) = 5.75U_* \log\left(30\frac{z}{k_s}\right) \tag{2.26}$$

In the coastal environment, waves and current are present at the same time. The changes to the current profile induced by waves should be considered in coastal sediment transport calculations. The effect of presence of waves on the current is intimately related to the processes taking place within the wave boundary layer. Although the thickness of the wave turbulent boundary layer is quite small when compared to the water depth, it still plays a very important role in determining the rate of water fluxes and sediment transport. As a consequence of near-bottom wave–current interaction, the prediction of the near-bottom wave–current velocity profile is sensitive to the presence of waves. This influence of the wave induced turbulence on the mean current can be schematized by introducing an ‘‘apparent’’ bed roughness, which is larger than the physical bottom roughness (Madsen 1991). Lundgren (1972) realized that waves change the current profile by increasing the eddy viscosity inside a thin layer ($z < L$) near the bed. Outside this layer, the waves do not introduce any mixing so the outer current profile has the usual logarithmic

form but with a larger zero intercept of z_1 which is written as

$$u(z) = \frac{U_*}{\kappa} \ln\left(\frac{z}{z_1}\right) \quad \text{for} \quad z > L \tag{2.27}$$

The wave effect on the outer current profile amounts to a constant shift,

$$\Delta u = \frac{U_*}{\kappa} \ln\left(\frac{z_0}{z_1}\right) \quad \text{for} \quad z > L \tag{2.28}$$

or an apparent roughness increase from $30z_0$ to $30z_1$ (Nielsen 1992). Inside the thin layer $z < L$, the current profile is

$$u(z) = \frac{U_*}{\kappa F} \ln\left(z / z_0 - 1\right) \quad \text{for} \quad z < L \tag{2.29}$$

where F = L/z_0.

Van Rijn (1993) also proposed a two-layer system to account for the wave effects in the near-bed layer,

$$u(z) = \begin{cases} \dfrac{U_c \ln\left(90\delta_w / k_a\right) \ln\left(30z / k_{s,c}\right)}{\ln\left(90\delta_w / k_{s,c}\right)\left[-1 + \ln\left(30h / k_a\right)\right]} & \text{for} \quad z < 3\delta_w \\ \dfrac{U_c \ln\left(30z / k_a\right)}{-1 + \ln\left(30h / k_a\right)} & \text{for} \quad z \geq 3\delta_w \end{cases} \tag{2.30}$$

where $k_{s,c}$ is the current-related bed roughness, k_a is the apparent roughness related to wave-current interaction equal to $k_{s,c} \min\left[10, \exp\left(\gamma u_w / U_c\right)\right]$, $r = 0.8 + \varphi - 0.3\varphi^2$ in which is the wave angle, δ_w is the maximum thickness of wave boundary layer equal to $0.072A_w(A_w/k_{s,w})^{-0.25}$ in which $k_{s,w}$ is the wave-related bed roughness.

2.3.2.2 Vertical Distribution of Suspended-load Concentration

In the riverine system, the vertical distribution of suspended-load concentration usually can be expressed as the Rouse distribution,

$$\frac{c(z)}{c_{b*}} = \left(\frac{h/z - 1}{h/\delta - 1} \right)^{\frac{\sigma_s \omega_s}{\kappa U_*}} \tag{2.31}$$

where c_{b*} is the near-bed suspended-load concentration, δ is the reference level, ω_s is the settling velocity, k is von Karman constant with a value of 0.4, and σ_s is the Schmidt number, related to sediment size, concentration, etc.

Van Rijn (1984c) proposed a two-layer system concentration profile,

$$\frac{c(z)}{c_{b*}} = \begin{cases} \left(\dfrac{h/z - 1}{h/\delta - 1} \right)^{\frac{\sigma_s \omega_s}{\kappa U_*}} & \text{for} \quad \dfrac{z}{h} < 0.5 \\ \left(\dfrac{1}{h/\delta - 1} \right)^{\frac{\sigma_s \omega_s}{\kappa U_*}} \exp\left[-4\left(\sigma_s \omega_s / \kappa U_* \right)\left(z/h - 0.5 \right) \right] & \text{for} \quad \dfrac{z}{h} \geq 0.5 \end{cases} \tag{2.32}$$

The concentration profile for z<0.5h is exactly the Rouse distribution.

Williams et al. (1999) developed a concentration distribution which was validated using measured data under combined waves and current, which can be used in the coastal environment. The distribution can be expressed as

$$\frac{c(z)}{c_{b*}} = \left(\frac{z + L_s \alpha_{wc}}{\delta + L_s \alpha_{wc}} \right)^{-\alpha_{wc}} \tag{2.33}$$

Where $\alpha_{wc} = \omega_s \Big/ \left[\kappa \left(\overline{U}_{*wcR} + U_{*wG} \right) \right]$, $\overline{U}_{*wcR}$ is the time-averaged bed-shear velocity for ripple-scale roughness, U_{*wG} is the peak wave-only bed-shear velocity for grain-scale roughness, and L_s is the vertical length scale for the suspended-load concentration distribution defined by

Nielsen (1992), which is determined as

$$L_s = \begin{cases} 0.075\Delta_r \, A_w\omega/\omega_s & \text{for } A_w\omega/\omega_s < 18 \\ 1.4\Delta_r & \text{for } A_w\omega/\omega_s \geq 18 \end{cases} \tag{2.34}$$

The parameters $\overline{U}_{*wcR}$ and U_{*wG} are calculated following Williams et al. (1999).

Van Rijn (2007b) investigated the suspended sediment transport by current and waves and suggested the vertical distribution of concentrations can be represented by the equation as follows

$$\frac{dc}{dz} = -\frac{(1-c)^5 \, c\omega_s}{\varepsilon_{s,cw}} \tag{2.35}$$

where c is the mean volume concentration at elevation z; $(1\text{-}c)^5$ corresponds to the decrease in the settling velocity for large concentrations; and $\varepsilon_{s,cw}$ is the mixing coefficient for the wave-current interaction. The reference concentration close to the bed is given by

$$c_{b*} = 0.015 \, f_{silt} \frac{d_{50}}{\delta} \frac{T_\tau^{1.5}}{D_*^{0.3}} \tag{2.36}$$

where δ is defined as the maximum value of half the wave-related and half the current-related bed roughness with a minimum value of 0.01 m. With the methods defined in Eq. (2.19), Van Rijn's suspended load formula can be applied to nonuniform material.

Camenen and Larson (2007) assumed an exponential concentration profile for the sediment (an exponential profile for the concentration converges to a physical value when $z \to 0$). The suspended load transport can be written as

$$q_{ss} = U_c c_{b*} \frac{\varepsilon}{\omega_s} \left[1 - \exp\left(-\frac{\omega_s h}{\varepsilon} \right) \right] \tag{2.37}$$

where ε is the sediment diffusivity related to the energy dissipation D:

$$\varepsilon = \left(\frac{D}{\rho}\right)^{1/3} h \quad \text{and} \quad D = k_b^3 D_b + k_c^3 D_c + k_w^3 D_w \tag{2.38}$$

where D_b, D_c, and D_w, are the energy dissipation from wave breaking, bottom friction due to current, and bottom friction due to waves; k_b, k_c, and k_w are coefficients. The reference concentration in Eq. (2.37) is defined as

$$c_{b*} = A_{cR}\theta_{cw,m} \exp\left(-4.5\frac{\theta_{cr}}{\theta_{cw}}\right) \tag{2.39}$$

where $A_{cR} = 3.5\times10^{-3}\exp\left(-0.3D_*\right)$.

There exist a few more reference concentration formulas in literature. The expression proposed by Smith and Mclean (1977) is

$$c_{b*} = C_0 \frac{\gamma_0 T_r}{1+\gamma_0 T_r} \tag{2.40}$$

where $\gamma_0 = 2.4 \times 10^{-3}$ is a constant, and $C_0 = 0.65$ is the maximum permissible concentration. Some other formulas are similar in form to that of Smith and McLean (1977), e.g. Garcia and Parker (1991) and Zyserman and Fredsoe (1994). These formulas follow the form of

$$c_{b*} = \frac{AX^n}{1+\frac{AX^n}{c_m}} \tag{2.41}$$

where A, c_m, and n are constants, and X is a combination of the appropriate dimensionless variables (such as the Shields parameter θ). In the formula of Garcia and Parker (1991), $X = u_* R_p^{0.6} / \omega_s$, $R_p = d_{50}\sqrt{(s-1)gd_{50}}/\nu$, $A = 1.3 \times 10^{-7}$, $c_m = 0.3$, and $n = 5$. Zyserman and Fredsoe (1994) defined $X = \theta - \theta_{cr}$, $A = 0.331$, $c_m = 0.46$, and $n = 1.75$.

CHAPTER III

NONUNIFORM SEDIMENT TRANSPORT CAPACITY AND NEAR-BED SUSPENDED SEDIMENT CONCENTRATION UNDER CURRENT AND WAVES

Quantitatively predicting sediment transport and morphologic evolution in coastal areas is necessary in support of engineering activities and studies. It is desirable to develop reliable formulas that can predict the equilibrium sediment transport rate to have a quick assessment for the engineering projects and support the predictive numerical models of morphology change and channel evolution in coastal areas. In addition, capturing the details of the near-bed sediment processes in coastal models is essential to predict the bottom change caused by waves and current, the entrainment of bed sediment into suspension, etc.

The influence of nonuniform or heterogeneous sediment properties on coastal processes is commonly underestimated due to the difficulty in characterizing and quantifying these types of sediments (Holland and Elmore, 2008). The tendency of many empirical formulas of coastal sediment transport, such as Bijker (1968), Van Rijn (1984b, 1993), Bailard (1981), Dibajnia and Watanabe (1992), Ribberink (1998), and Camenen and Larson (2007), is to assume uniform or homogeneous sediments (e.g. a well-sorted fine sand). There exist quite a few near-bed concentration relationships in literature, for instance, Smith and McLean (1977), Van Rijn (1984b), Garcia and Parker (1991), and Camenen and Larson (2007), which were designed for uniform sediments as well. Extensive databases have been established for single-sized sediment

transport based on the past laboratory and field measurements (SEDMOC, 1999; Camenen and Larson, 2007). In contrast, very few studies have concerned nonuniform sediment transport in coastal environments. Dibajnia and Watanabe (1996) extended their bed-load transport rate formula (Dibajnia and Watanabe, 1992) to mixed sand transport. Hassan et al. (2001) applied Ribberink's (1998) bed-load transport formula to calculate the transport rate of nonuniform material under oscillatory sheet flow. Van Rijn (2007a, b, c) extended his bed-load and suspended-load transport formulas in steady river flow to coastal flow under currents and waves and investigated the hiding/exposure correction factors for computing multiple-sized sediment transport. Recently a nonuniform sand transport formula was developed by van der A et al. (2013), considering the hiding and exposure effect through a correction factor, as well as the skewed, asymmetric waves. In recent years, laboratory experiments on mixed sediment transport under coexisted currents and waves have been conducted by several groups (Inui et al., 1995; Dibajnia and Watanabe, 2000; Jacobs and Dekker, 2000; Sistermans, 2001; Ahmed, 2002; De Meijer et al., 2002; O'Donoghue and Wright, 2004; Hassan and Ribberink, 2005) and can be used to validate multiple-sized sediment transport formulas.

Nonuniform sediment transport exhibits difference from uniform sediment, even when the mean grain size is the same for both cases. The hiding, exposure, and armoring among different size classes in the nonuniform bed material may significantly affect sediment transport, morphological change, bed roughness, wave dissipation, etc. For example, it is often observed that bed sediment coarsening can affect the navigation channel near a coastal inlet, and a model prediction based on the assumption of single-sized sediment often overpredicts the channel depth there. It is necessary to develop multiple-sized sediment transport capacity formula and a near-bed

suspended sediment concentration formula to improve the accuracy and reliability of analysis methods and models for coastal sedimentation. In this chapter, the Wu et al. (2000b) bed-load and suspended-load formulas are extended to multiple-sized sediment transport under non-breaking waves and currents for coastal applications. A new formula to predict the near-bed suspended-load concentration under current and waves is also proposed. Methods are developed to determine the bed shear stress due to waves only and combined current and waves, and in turn applied to compute the bed-load and suspended-load transport rates. Different methods in literature have been tested and chosen to determine the edge of the bed-load layer, i.e., the reference level.

3.1 Extension of the Wu et al. Formula to Nonuniform Sediment Transport under Current and Waves

Wu et al. (2000b) related the bed-load transport rate to the non-dimensional excess grain shear stress and the suspended-load transport rate to the rate of energy available in the flow system. Through dimensional analysis and calibration using available measurement data, the relations for the fractional transport rates of non-uniform bed load and suspended load were derived as

$$\frac{q_{b*k}}{p_{bk}\sqrt{(\gamma_s/\gamma-1)gd_k^3}} = 0.0053\left(\frac{\tau_b'}{\tau_{cri,k}}-1\right)^{2.2} \tag{3.1}$$

$$\frac{q_{s*k}}{p_{bk}\sqrt{(\gamma_s/\gamma-1)gd_k^3}} = 0.0000262\left[\left(\frac{\tau}{\tau_{cri,k}}-1\right)\frac{U}{\omega_{sk}}\right]^{1.74} \tag{3.2}$$

where q_{b*k} and q_{s*k} are the bed-load and suspended-load transport rates of sediment size class k by volume per unit time and width (m^2s^{-1}); d_k is the representative diameter of size class k of the sediment mixture; p_{bk} is the fraction of sediment size class k in the bed material; g is the gravitational acceleration; γ_s and γ are the specific weights of sediment and water, respectively; τ is the shear stress on the wetted perimeter of the cross-section including bed and banks; τ_b' is the bed shear stress corresponding to grain roughness; $\tau_{cri,k}$ is the critical shear stress for the incipient motion of sediment size k on the bed; ω_{sk} is the settling velocity; and U is the depth-averaged flow velocity.

The Wu et al. (2000b) formula has been extensively tested by its developers using a large set of measurement data. It has been recommended independently by international peers (e.g., Ribberink et al., 2002) as one of the top choices in literature for determining the nonuniform sediment transport under current. Its advantages include: a) the formulations are simple but well proven in sediment transport theory; b) it relates the bed-load transport to the grain shear stress and the suspended-load transport to the energy of the flow system, which are commonly accepted concepts in sedimentation engineering; c) it considers the effect of bed material size composition in the hiding and exposure correction factor, which is omitted in many other existing formulas; and d) it has been tested using extensive data sets of single-sized and multiple-sized sediment transport in rivers.

In most coastal processes, the sediment transport is simultaneously influenced by both current and waves. However, the interaction of the current and wave induced bed shear stresses is nonlinear, which is one of the difficult effect to estimate (Fig. 3.1). To apply Eqs. (3.1) and (3.2) to sediment transport under current and waves in coastal context, the most important step is to

determine the bed shear stress. In river systems, the flow is usually quasi-steady, so that the bed shear stress is often estimated through measurement of energy slope. For oscillatory flows or combined quasi-steady and oscillatory flows, the energy slope is not easy to be measured directly, and thus the bed shear stress must be estimated through the theoretical or empirical models of the bed roughness. For a sediment bed with sand grains and bed forms (such as sand, ripples, and dunes), the bed shear stress is composed of two contributions: the grain shear stress due to the drag on individual sand grains, and the form shear stress due to the pressure field acting on the ripples or larger bedforms,

$$\tau_b = \tau_b' + \tau_b'' \tag{3.3}$$

where τ_b, τ_b', and τ_b'' are the total, grain, and form shear stresses, respectively. The methods used in the extended Wu et al. sediment transport formula to determine the bed shear stress due to current only, waves only and combined current and waves are described below.

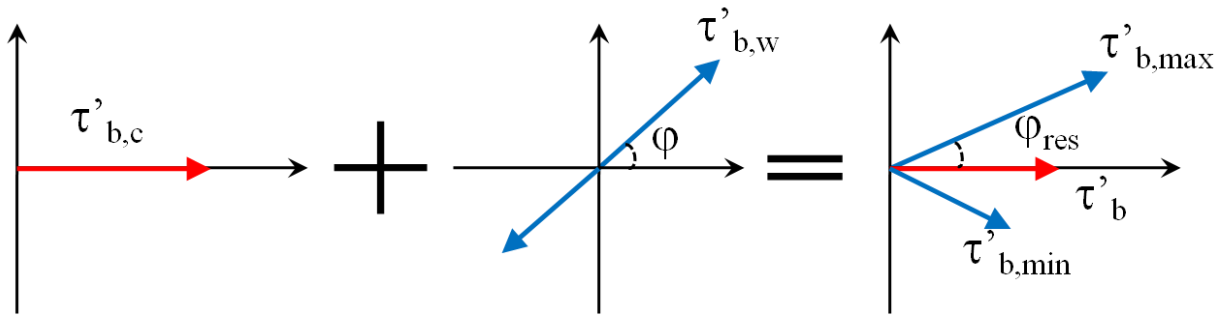

Figure 3.1 Schematic diagram for nonlinear interaction between current and waves bed shear stresses (after Soulsby 1997)

3.1.1 Bed Shear Stress due to Current

The bed shear stress due to current is still related to the depth-averaged current velocity through the Manning equation,

$$\tau_{b,c} = \frac{\rho g n^2}{h^{1/3}} U_c^2 \tag{3.4}$$

where $\tau_{b,c}$ is bed shear stress due to current; U_c is the depth-averaged current velocity; and n is the Manning roughness coefficient. The Manning roughness coefficient is converted from the equivalent bed roughness height estimated using empirical formulas or specified according to the flow and bed conditions. Using the relation between Manning roughness coefficient and Chezy coefficient, the Manning roughness coefficient is determined herein as

$$n = \frac{h^{1/6}}{18\log(12h/k_s)} \tag{3.5}$$

where k_s is the equivalent roughness height, which consists of grain roughness k_s' and ripple roughness k_s'',

$$k_s = k_s' + k_s'' \tag{3.6}$$

Note that some scientists (e.g., Camenen and Larson, 2007; van der A et al., 2013) include the roughness due to sediment transport when calculating the total equivalent bed roughness in Eq. (3.6), whereas others (e.g., Einstein, 1950; van Rijn, 1984a, b) do not. The present study chooses not to include the roughness due to sediment transport since it is usually much smaller than the form (ripple) roughness.

The grain roughness height has been given different values in literature. When the bed friction is determined using the Manning equation, the grain roughness height is often set as the median sediment size d_{50} (Strickler, 1923; Wu and Wang, 1999), d_{65} (Patel and Ranga Raju, 1996), or d_{90} (Meyer-Peter and Mueller, 1948). When the logarithmic formula is used to determine the bed friction, k_s' is given as $2d_{50}$ (Camenen and Larson, 2007) and $3d_{90}$ (van Rijn, 1984a). In this study, k_s' has a possible range of $1.5d_{90}$ to $3d_{90}$, with the default value as $3d_{90}$.

The bed forms considered in the coastal context usually are sand ripples. The ripple roughness height is estimated using the method of Soulsby (1997),

$$k_s'' = A_r \frac{\Delta_r^2}{\lambda_r} \tag{3.7}$$

where Δ_r and λ_r are the ripple height and length, respectively; and A_r is a coefficient which varies from 5.0 to 40.0. Nielsen (1992) suggested A_r=8.0, and van Rijn (1993) proposed A_r=20.0. The default A_r is set as 12.0 in this study.

In the presence of current only, the ripple height and length are determined using the method of Raudkivi (2006):

$$\lambda_r = 245 d_{50}^{0.35} \tag{3.8}$$

$$\Delta_r = 0.074 d_{50}^{-0.253} \lambda_r \tag{3.9}$$

where d_{50} is the sediment diameter in mm. The units of Δ_r and λ_r in Eqs. (3.8) and (3.9) are mm.

The bed shear stress due to current in Eq. (3.4) is used for suspended load, whereas in the bed-load calculation, one should use the grain shear stress due to current, which is determined by

$$\tau'_{b,c} = \left(\frac{n'}{n}\right)^{3/2} \tau_{b,c} \tag{3.10}$$

where $\tau'_{b,c}$ is the grain shear stress due to current; and n' is the Manning roughness coefficient due to grain roughness, which is calculated as $n' = d_{50}^{1/6}/20$. For convenience, Eq. (3.10) can also be written as

$$\tau'_{b,c} = \frac{1}{2}\rho f'_c U_c^2 \tag{3.11}$$

where f'_c is the friction coefficient for grain bed shear stress, expressed as

$$f'_c = 2\left(\frac{n'}{n}\right)^{1.5} \frac{gn^2}{h^{1/3}} \tag{3.12}$$

3.1.2 Bed Shear Stress due to Waves

The bed shear stress due to non-breaking waves is determined using the formula of Jonsson (1966):

$$\tau_{b,wm} = \frac{1}{4}\rho f_w U_w^2 \tag{3.13}$$

where $\tau_{b,wm}$ is the mean bottom wave stress averaged over a wave cycle, U_w is the amplitude of wave orbital velocity near the bed at the edge of wave boundary layer, and f_w is the bed friction coefficient of waves, which is determined using the Soulsby (1997) formula:

$$f_w = 0.237\left(A_w / k_s\right)^{-0.52} \tag{3.14}$$

where A_w is the wave excursion $A_w = U_w T_w / 2\pi$, with T_w being the wave period.

The mean grain shear stress due to waves is calculated as

$$\tau'_{b,wm} = \frac{1}{4}\rho f'_w U_w^2 \tag{3.15}$$

where $\tau'_{b,wm}$ is the mean grain shear stress due to waves averaged over a wave cycle and f'_w is the bed skin friction factor determined by

$$f'_w = 0.237\left(A_w / k'_s\right)^{-0.52} \tag{3.16}$$

The equivalent roughness height is determined using Eqs. (3.6) and (3.7). The height and length of ripples in the case of only waves are determined using the method of Soulsby and Whitehouse (2005):

$$\lambda_r = \frac{A_w}{1.0 + 0.00187\dfrac{A_w}{d_{50}}\left\{1.0 - \exp\left[-\left(0.0002\dfrac{A_w}{d_{50}}\right)^{1.5}\right]\right\}} \tag{3.17}$$

$$\Delta_r = 0.15\lambda_r\left\{1.0 - \exp\left[-\left(5000\frac{d_{50}}{A_w}\right)^{3.5}\right]\right\} \tag{3.18}$$

For asymmetric waves shown in Fig. 3.2, the second-order Stokes theory is applied, i.e. the instantaneous wave velocity is described as

$$u_w(t) = U_w\left(\cos\omega t + r_w \cos 2\omega t\right) \tag{3.19}$$

where ω is the angular frequency of wave $\omega = 2\pi / T_w$, and r_w is the wave asymmetry coefficient defined as $r_w = u_{w,max} / U_w - 1$. Note that the wave asymmetry coefficient r_w is different from the one

$R_w = u_{w,max} / (2U_w)$ used in several references (e.g., Inui et al., 1995; Dibajnia and Watanabe, 2000; Ahmed, 2002).

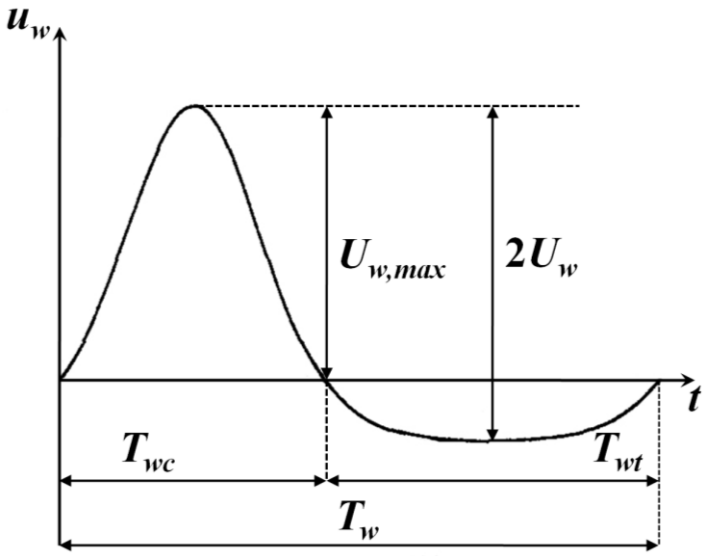

Figure 3.2 Sketch of Asymmetric Wave

The bed grain shear stresses averaged in the crest (onshore) and trough (offshore) half wave cycles, denoted as $\tau'_{b,wm.on}$ and $\tau'_{b,wm.off}$, are derived as (Camenen, 2002)

$$\tau'_{b,wm.on} = \frac{1}{2}\rho f'_w \frac{U_w^2}{2}\left(1 + r_w^2 + \frac{13}{6} r_w \frac{\sin a_c}{a_c} + \frac{1}{6}\frac{\sin 2a_c}{2a_c}\right) \tag{3.20}$$

$$\tau'_{b,wm.off} = \frac{1}{2}\rho f'_w \frac{U_w^2}{2}\left(-1 - r_w^2 + \frac{13}{6} r_w \frac{\sin a_t}{a_t} - \frac{1}{6}\frac{\sin 2a_t}{2a_t}\right) \tag{3.21}$$

where $a_c = \pi T_{wc} / T_w$ and $a_t = \pi T_{wt} / T_w$, with $T_{wc} = \frac{T_w}{\pi} \arccos\left(\frac{\sqrt{\Delta U} - 1}{4 r_w} \right)$, $T_{wt} = T_w - T_{wc}$, and $\Delta U = 1 + 8 r_w^2$. The bed skin friction coefficient f_w' is determined using Eq. (3.16).

3.1.3 Bed Shear Stress due to Combined Current and Waves

In the case of combined current and waves, the velocity diagram is shown in Fig. 3.3. For the onshore half cycle, the angle between current and waves is denoted as φ. Thus, the angle in the offshore half cycle is π-φ. The onshore and offshore resultant grain shear stresses due to the combined current and waves are expressed as

$$\tau'_{b,on} = \frac{1}{2} \rho f'_{cw} \left(U_c^2 + U_{wm,on}^2 + 2 U_c U_{wm,on} \cos\varphi \right) \tag{3.22}$$

$$\tau'_{b,off} = \frac{1}{2} \rho f'_{cw} \left(U_c^2 + U_{wm,off}^2 + 2 U_c U_{wm,off} \cos(\pi - \varphi) \right) \tag{3.23}$$

where f'_{cw} is the friction coefficient of grain bed shear stress under combined current and waves, and $U_{wm,on}$ and $U_{wm,off}$ are the root-mean-square values of the wave velocity over the onshore and offshore half cycles, respectively. $U_{wm,on}$ and $U_{wm,off}$ may be derived from Eqs. (3.20) and (3.21) using $U_{wm,on}^2 = \tau'_{b,wm,on} / \left(\frac{1}{2} \rho f'_w \right)$ and $U_{wm,off}^2 = \tau'_{b,wm,off} / \left(\frac{1}{2} \rho f'_w \right)$. The friction coefficient f'_{cw} is computed as

$$f'_{cw} = X_u f'_c + (1 - X_u) f'_w \tag{3.24}$$

with $X_u = U_c^2 \Big/ \left(U_c^2 + 0.5U_w^2\right)$. The grain friction coefficients of only current and only waves, f_c' and f_w' are determined using Eqs. (3.12) and (3.16), respectively.

The grain shear stress in Eqs. (3.22) and (3.23) are used in the bed-load transport formula. For the suspended-load transport formula, one may also derive similar formulations to determine the total bed shear stress. Actually, the following simple formulation of the total shear stress is found to be adequate in the suspended-load transport formula presented in the next section:

$$\tau_b = \sqrt{\tau_{b,c}^2 + \tau_{b,wm}^2 + 2\tau_{b,c}\tau_{b,wm}\cos\varphi} \tag{3.25}$$

where $\tau_{b,c}$ and $\tau_{b,wm}$ are determined using Eqs. (3.4) and (3.13), respectively.

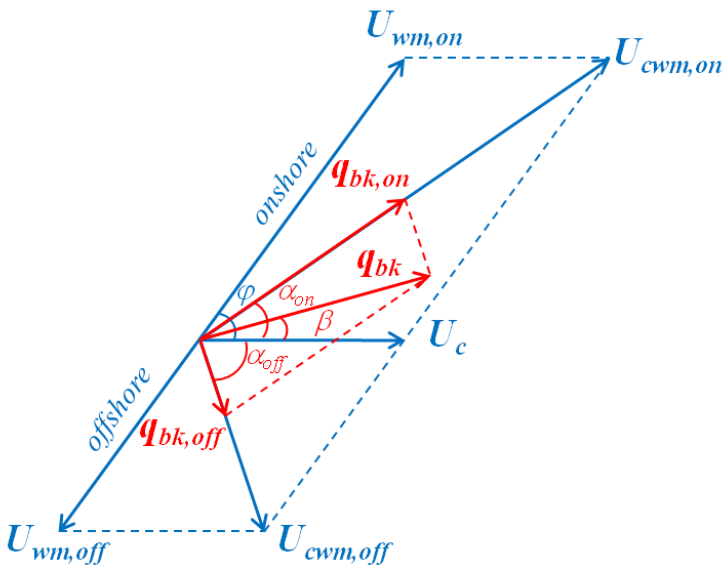

Figure 3.3 Sketch of Waves and Current Interaction

3.1.4 Multiple-Sized Sediment Transport Rate under Current and Waves

The onshore and offshore bed-load transport rates, $q_{b*k,on}$ and $q_{b*k,off}$, are determined respectively using Eq. (3.1) as follows:

$$q_{b*k,on} = 0.0053 p_{bk} \sqrt{(\gamma_s / \gamma - 1) g d_k^3} \left(\frac{\tau'_{b,on}}{\tau_{cri,k}} - 1 \right)^{2.2} \tag{3.26}$$

$$q_{b*k,off} = 0.0053 p_{bk} \sqrt{(\gamma_s / \gamma - 1) g d_k^3} \left(\frac{\tau'_{b,off}}{\tau_{cri,k}} - 1 \right)^{2.2} \tag{3.27}$$

The onshore and offshore bed-load transport directions are assumed to be along the resultant onshore and offshore velocities as shown in Fig. 3.3. The net transport rate is thus calculated by summing the two vectors corresponding to the onshore and offshore bed-load transport rates:

$$\vec{q}_{b*k} = \frac{T_{wc}}{T_w} \vec{q}_{b*k,on} + \frac{T_{wt}}{T_w} \vec{q}_{b*k,off} \tag{3.28}$$

The magnitude and angle of the bed-load transport are calculated as

$$q_{b*k} = \sqrt{\left(\frac{T_{wc}}{T_w} q_{bk,on} \right)^2 + \left(\frac{T_{wt}}{T_w} q_{bk,off} \right)^2 + 2 \frac{T_{wc} T_{wt}}{T_w^2} q_{bk,on} q_{bk,off} \cos(\alpha_{on} + \alpha_{off})} \tag{3.29}$$

$$\beta = \alpha_{on} - \arccos \left\{ \left[\frac{T_{wc}}{T_w} q_{bk,on} + \frac{T_{wt}}{T_w} q_{bk,off} \cos(\alpha_{on} + \alpha_{off}) \right] \Big/ q_{bk} \right\} \tag{3.30}$$

where α_{on}, α_{off}, and β are the onshore, offshore, and resultant bed-load transport angles with respect to the current direction, respectively, as shown in Fig. 3.3. α_{on} and α_{off} are calculated as

$$\alpha_{on} = \arccos\left(\frac{U_c + U_{wm,on}\cos\varphi}{\sqrt{U_c^2 + U_{wm,on}^2 + 2U_c U_{wm,on}\cos\varphi}}\right) \tag{3.31}$$

$$\alpha_{off} = \arccos\left(\frac{U_c + U_{wm,off}\cos(\pi-\varphi)}{\sqrt{U_c^2 + U_{wm,off}^2 + 2U_c U_{wm,off}\cos(\pi-\varphi)}}\right) \tag{3.32}$$

Certainly it is desirable to differentiate the onshore and offshore suspended-load transport rates, but this is not done in this study due to the limit of data availability. The net transport rate of the *k*th size class of suspended load along the current direction is computed as

$$q_{s*k} = 0.0000262\, p_{bk}\sqrt{(\gamma_s/\gamma - 1)g d_k^3}\left[\left(\frac{\tau_b}{\tau_{cri,k}} - 1\right)\frac{U_c}{\omega_{sk}}\right]^{1.74} \tag{3.33}$$

where τ_b is determined using Eq. (3.25), U_c is the depth-averaged current velocity, and ω_{sk} is the settling velocity calculated using the Zhang (1961) formula (see Wu, 2007).

3.1.5 Test of the Enhanced Wu et al. Formula against Measurement Data

Camenen and Larson (2007) compiled a wide range of existing data sets of single-sized bed-load and suspended-load under current and waves, which are used to test the developed sediment transport formula in this study. Several sets of data on nonuniform or multiple-sized bed-load and suspended-load collected from other literature are also used. In addition, the developed formulas are also compared with several existing formulas. The test and comparison results are presented in the following subsections.

3.1.5.1 Test Using Uniform Bed-Load Transport Data

Table 3.1 summarizes the current and wave conditions and sediment properties for the data sets of single-sized bed load under only waves and combined currents and waves compiled by Camenen and Larson (2007). Here, "single-sized" does not mean "uniform", because the sediments in a few cases are actually quite nonuniform as indicated by the sediment standard deviation, σ_g, in Table 3.1. Even though the Wu et al. formulas are often used for multiple-sized sediment mixtures, it can be used for single-sized cases by setting the number of size classes as 1.

Most of the data sets in Table 3.1 were from oscillating water tunnels (OWT), some early experiments used oscillating trays (OT, i.e. oscillating bed in a tank of still water), and some recent ones were conducted in large wave flumes (LWF). Abou-Seida (1965), Ahilan and Sleath (1987), Horikawa et al. (1982), Kalkanis (1964), King (1991), Sawamoto and Yamashita (1986), and Sleath (1977) measured the bed-load transport in a half wave cycle. These data sets are used to test the onshore (half-cycle average) bed-load transport rate calculated using Eq. (3.26). The remaining data in Table 3.1 consider a full wave cycle and are used to test the net bed-load transport rate calculated using Eq. (3.28).

Table 3.1 Data Summary for Uniform Bed-load Transport Experiments
(Courtesy to Camenen and Larson, 2007)

Author(s)	Exp. facility	Cycle	No. of runs	s	d_{50} (mm)	U_c (m/s)	σ_g	U_w (m/s)	T_w (s)
Abou-Seida (1965)	OT	Half	9 37	2.23 2.65	0.70 0.14-2.61	0 0		0.41-0.80 0.35-1.28	2.0-4.8 1.7-5.1
Ahilan and Sleath (1987)	OWT	Half	5 4	1.14 1.44	4.0 4.3	0 0		0.32-0.51 1.10-1.22	3.6-3.7 4.7-4.9
Horikawa et al. (1982)	OWT	Half	6	2.66	0.20-0.70	0		0.76-1.27	2.6-6.0
Kalkanis (1964)	OT	Half	27	2.63	1.68-2.82	0		0.28-0.71	3.2-6.2
King (1991)	OWT	Half	178	2.65	0.14-1.10	0		0.30-1.21	2.0-12.0

Sawamoto and Yamashita (1986)	OWT	Half	7 15	1.58 2.65	1.50 0.2-1.8	0 0		0.44-1.25 0.74-1.25	3.8 3.8
Sleath (1977)	OT	Half	12 8 14	1.14 2.58 2.61	3.04 1.89 4.24	0 0 0		0.08-0.17 0.31-0.37 0.27-0.67	1.3-9.0 0.6-2.0 0.5-2.7
Dibajnia and Watanabe (1992)	OWT	Full	25 76	2.65 2.65	0.20 0.20	0 -0.26-0.22		0.63-1.00 0.64-1.00	1.0-4.0 1.0-4.0
Watanabe and Isobe (1990)	OWT	Full	12 51	2.65 2.65	0.18, 0.87 0.18, 0.87	0 -0.30-0.25		0.27-0.43 0.27-0.43	3.0, 6.0 3.0, 6.0
Ahmed and Sato (2003)	OWT	Full	15	2.65	0.21-0.74	0		0.97-1.54	3.0
Ribberink and Chen (1993)	OWT	Full	4 4	2.65 2.65	0.13 0.13	0 0.02-0.06	1.38	0.64-1.23 0.64-1.23	6.5 6.5
Ribberink and Al Salem (1994)	OWT	Full	10 30	2.65 2.65	0.21 0.21	0 -0.11-0.56	1.52	0.95-1.87 0.37-1.37	5.0-12.0 5.0-12.0
Dohmen-Janssen and Hanes (2002)	LWF	Full	4	2.65	0.24	-0.05 ~ -0.03	1.33	0.89-1.05	6.5, 9.1
Dohmen-Janssen (1999)	OWT	Full	27	2.65	0.13-0.32	0.23-0.45		0.46-1.70	4.0-12.0
Ramadan (1994)	OWT	Full	5	2.65	0.21	0.02-0.47	1.52	0.81-0.84	6.5
Ribberink (1995)	OWT	Full	5	2.65	0.21	-0.45-0.45	1.52	0.86-1.27	6.5
Katopodi et al. (1994)	OWT	Full	4	2.65	0.21	0.18-0.43	1.52	0.95-1.69	7.2
Janssen et al. (1996)	OWT	Full	12	2.65	0.13	0.23-0.43	1.42	0.49-1.47	4.0-12.0
Van der Hout (1997)	OWT	Full	11	2.65	0.21, 0.32	0.23-0.45	1.44–1.52	0.46-1.70	4.0-12.0
Cloin (1998)	OWT	Full	5	2.65	0.19	0.01-0.41	2.09	0.83-1.49	6.4-7.2
Hassan et al. (1999)	OWT	Full	3	2.65	0.24	0.03	4.13	0.83-1.22	6.5

Figs. 3.4 and 3.5 compare the predicted and measured transport rates of uniform bed-load with waves only and combined current and waves, respectively. In the figures, the solid line is a line with slope of 45°, which means the predicted transport rates have a perfect agreement with the measurement; the dashed lines indicate the predicted transport rates are within a factor of 2 of the

measurements, which is half or twice as the measured values; and the dashed dotted lines are the lien with a factor of 5, which indicates the predicated values are 1/5 or 5 times as the meausurements. One can see that the predicted and measured rates match reasonably well, even though some scatter occurs. The errors can be from both formulation and measurement. In addition, the bed shear stress is difficult to measure when waves are included, and it has to be estimated using empirical models which may add uncertainties in the predicted sediment transport rates.

Tables 3.2 show the performance statistics for predicted uniform bed-load transport rates with waves only and combined current and waves. One type of performance statistics used is the percentages of test cases in which the ratio of predicted to measured transport rates, *r*, is in error ranges of 0.8–1.25, 0.667–1.5, 0.5–2.0, and 0.2–5.0. For both waves only and combined current and waves, about 50% of the cases are predicted within a factor of 2 of the measured values, and more than 75% of the cases are within a factor of 5. The other statistics used are the logarithmic root-mean-square error (E_{rms}) and bias defined as

$$\log\left(E_{rms}\right)=\sqrt{\frac{1}{N}\sum_{i=1}^{N}\left[\log\left(\frac{q_{b,predicted}}{q_{b,measured}}\right)\right]^2} \tag{3.34}$$

$$\log\left(bias\right)=\frac{1}{N}\sum_{i=1}^{N}\log\left(\frac{q_{b,predicted}}{q_{b,measured}}\right) \tag{3.35}$$

The logarithmic root-mean-square errors are 0.429 and 0.515 for the cases of waves only and combined current and waves, respectively. The logarithmic bias are -0.067 and 0.017 for cases of waves only and combined current and waves, respectively.

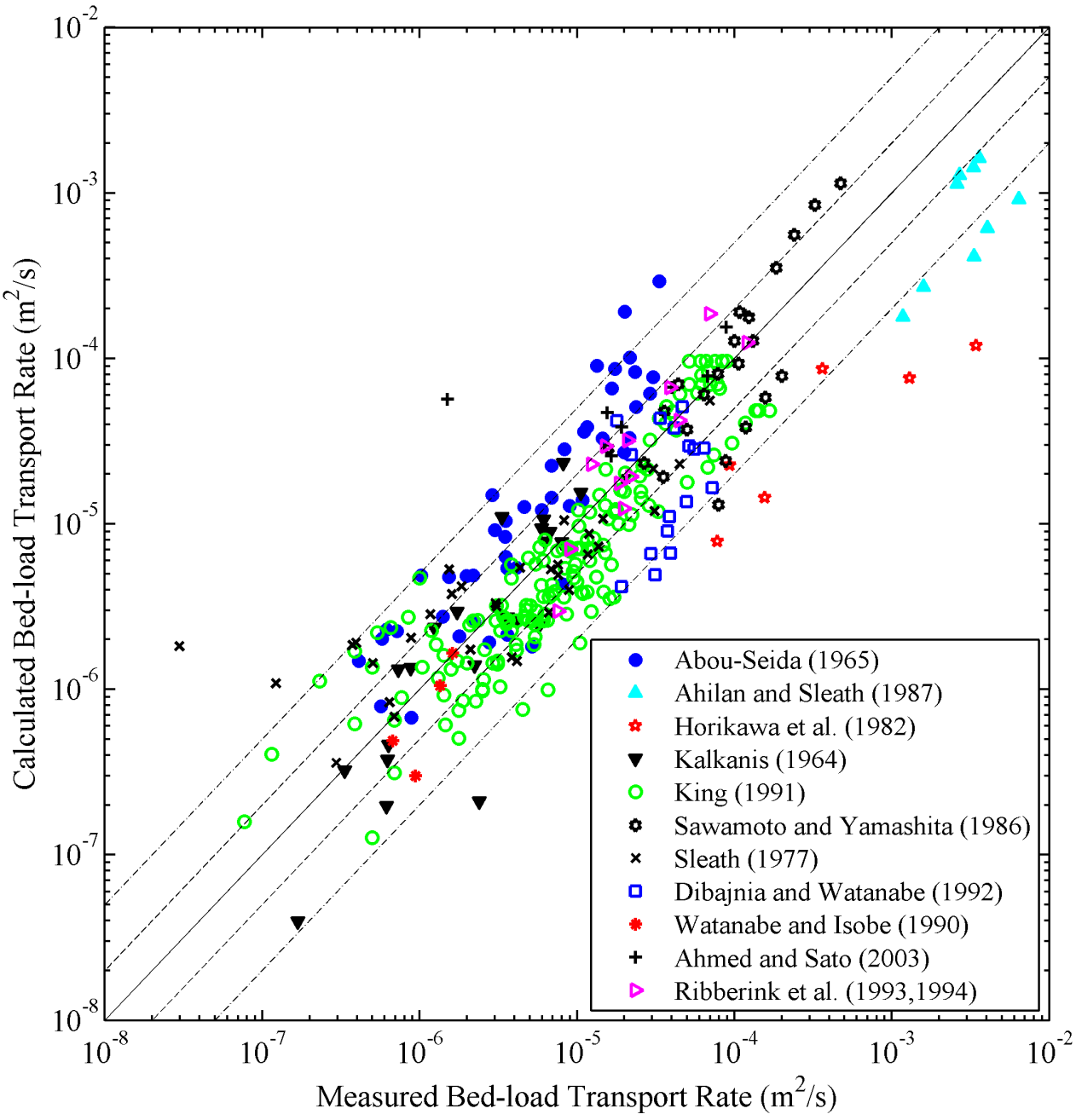

Figure 3.4 Comparison of Predicted and Measured Transport Rates of Uniform Bed Load with Waves Only (Solid line – Perfect agreement; Dashed lines – factor 2; Dashed dotted lines – factor 5)

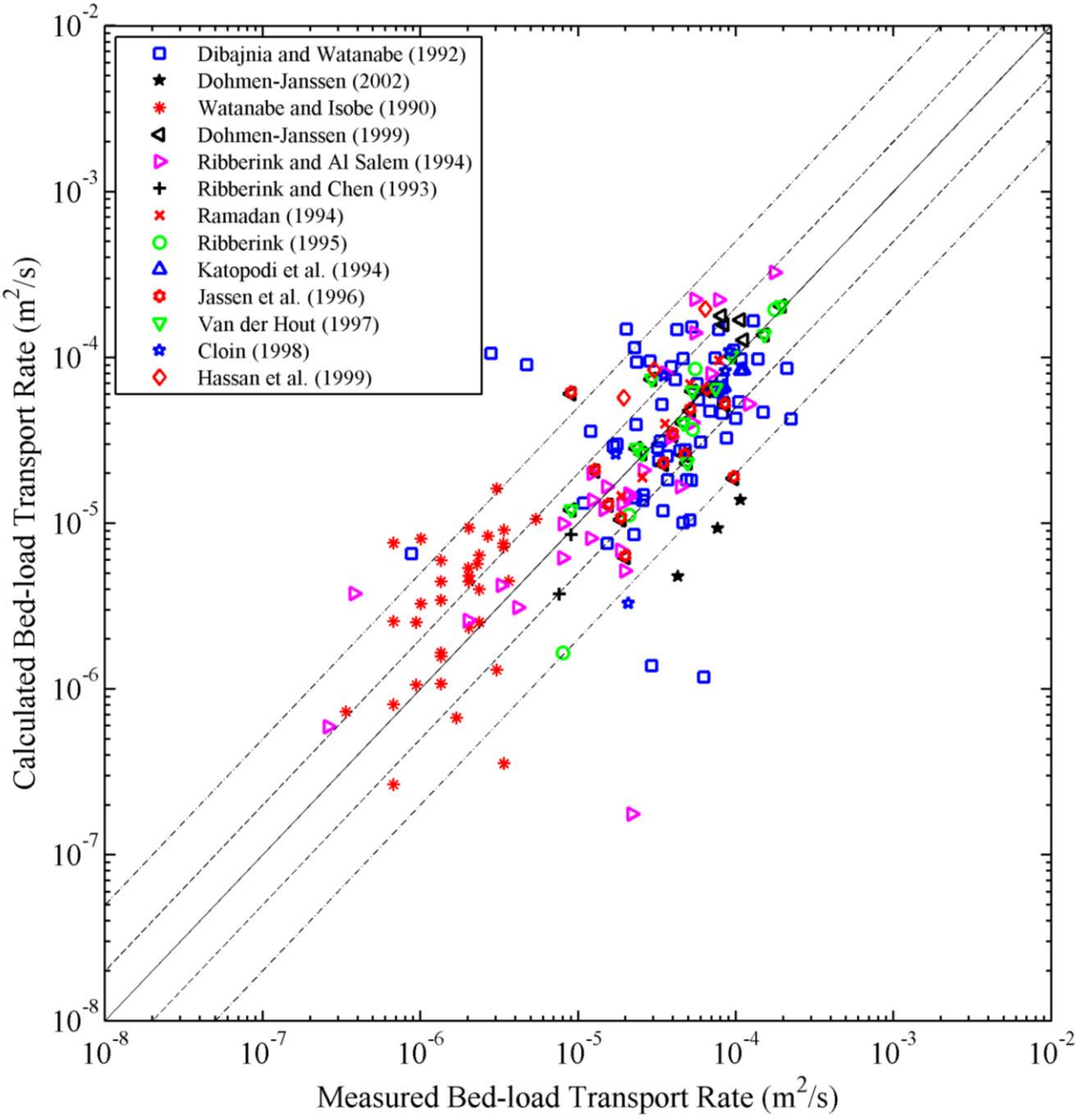

Figure 3.5 Comparison of Predicted and Measured Transport Rates of Uniform Bed Load with Combined Current and Waves

Table 3.2 Statistics for Predicted Transport Rate of Uniform Bed Load

Conditions	% of Calculated Transport Rates in Error Range				Log(E_{rms})	Log(*bias*)
	0.8-1.25	0.67-1.5	0.5-2.0	0.2-5.0		
Uniform, Waves only	17.1	34.7	52.8	86.5	0.429	-0.067
Uniform, Current and Waves	23.2	34.2	48.5	75.1	0.515	0.017

3.1.5.2 Test Using Nonuniform Bed-Load Transport Data

Table 3.3 summarizes data sets for multiple-sized bed load measured by Inui et al. (1995), Dibajnia and Watanabe (2000), Ahmed (2002), O'Dononghue and Wright (2004), and Hassan and Ribberink (2005) under waves and measured by de Meijer et al. (2002) under combined current and waves. These experiments were conducted in oscillating water tunnels (OWT) or oscillating flow tunnels (OFT). The number of size classes was 2 or 3, which implies that narrowly graded sediment mixtures were used in the experiments. Each size class is represented by the average value of its lower and upper bound diameters.

The key parameters in the developed bed-load formula have been carefully assessed. It is found that the grain roughness height k_s' is one of the most important parameters. In previous section, it is found that $k_s' = 3d_{90}$ gives overall adequate bed-load transport rate values for the uniform bed-load test cases. However, the value of $3d_{90}$ for k_s' significantly overpredicts the transport rates for these nonuniform bed-load experiments, as shown in Figs. 3.6. After trial and error, it is found that $k_s' = 1.5d_{90}$ provides better predictions, as shown in Figs. 3.7. The difference in k_s' for uniform and nonuniform cases might be owing to that d_{50} is used to represent the sediment mixture size in the uniform cases whereas a mean size-class diameter is used to represent each size class in the nonuniform cases. Table 3.4 shows the statistics for the predicted fractional

bed-load transport rates with different values of k_s'. The accuracy when using $1.5d_{90}$ for k_s' is generally good. About 60% of the cases are predicted within a factor of 2 of the measured values, and more than 75% of the cases are within a factor of 5. The logarithmic root-mean-square errors and bias are 0.307 and 0.051, respectively.

Table 3.3 Data Summary for Nonuniform Bed-load Transport Experiments

Author(s)	Exp. Facil.	Cycle	No. of runs	No. of sizes	s	d_{50} (mm)	σ_g	U_c (m/s)	U_w (m/s)	T_w (s)
Ahmed (2002)	OWT	Full	4 15	2 3	2.65 2.51-2.59	0.37-0.47 0.23-0.59	1.36–1.9	0 0	1.32-1.67 1.17-1.50	3.0 3.0
Hassan and Ribberink (2005)	OWT	Full	5 5	2 3	2.65 2.65	0.15, 0.19 0.24	1.85–4.21	0 0	0.82-1.20 0.64-1.27	6.5 12.0
O'Dononghue and Wright (2004)	OFT	Full	2 4	2 3	2.65 2.65	0.28 0.19, 0.28	1.85	0 0	1.20 1.20	5.0, 7.5 5.0, 7.5
De Meijer et al. (2002)	OWT	Full	1 1	3 3	2.65 2.65	0.19 0.19		0.192 0.371	1.45 0.95	7.20 7.20
Inui et al. (1995)	OFT	Full	16	2	2.65	0.37-0.70		0	0.24-0.77	3.0, 5.0
Dibajnia and Watanabe (2000)	OFT	Full	18	2	2.65	0.29-0.51		0	0.97-1.54	3.0

Table 3.4 Statistics for Predicted Fractional Transport Rate of Nonuniform Bed-load

Conditions	k_s'	% of Calculated Transport Rates in Error Range				Log(E_{rms})	Log(*bias*)
		0.8-1.25	0.67-1.5	0.5-2.0	0.2-5.0		
Nonuniform, Waves only, or Cuurent and Waves	$3d_{90}$	4.0	14.1	33.6	64.4	0.623	0.445
	$1.5d_{90}$	23.5	38.3	57.0	75.2	0.307	0.051

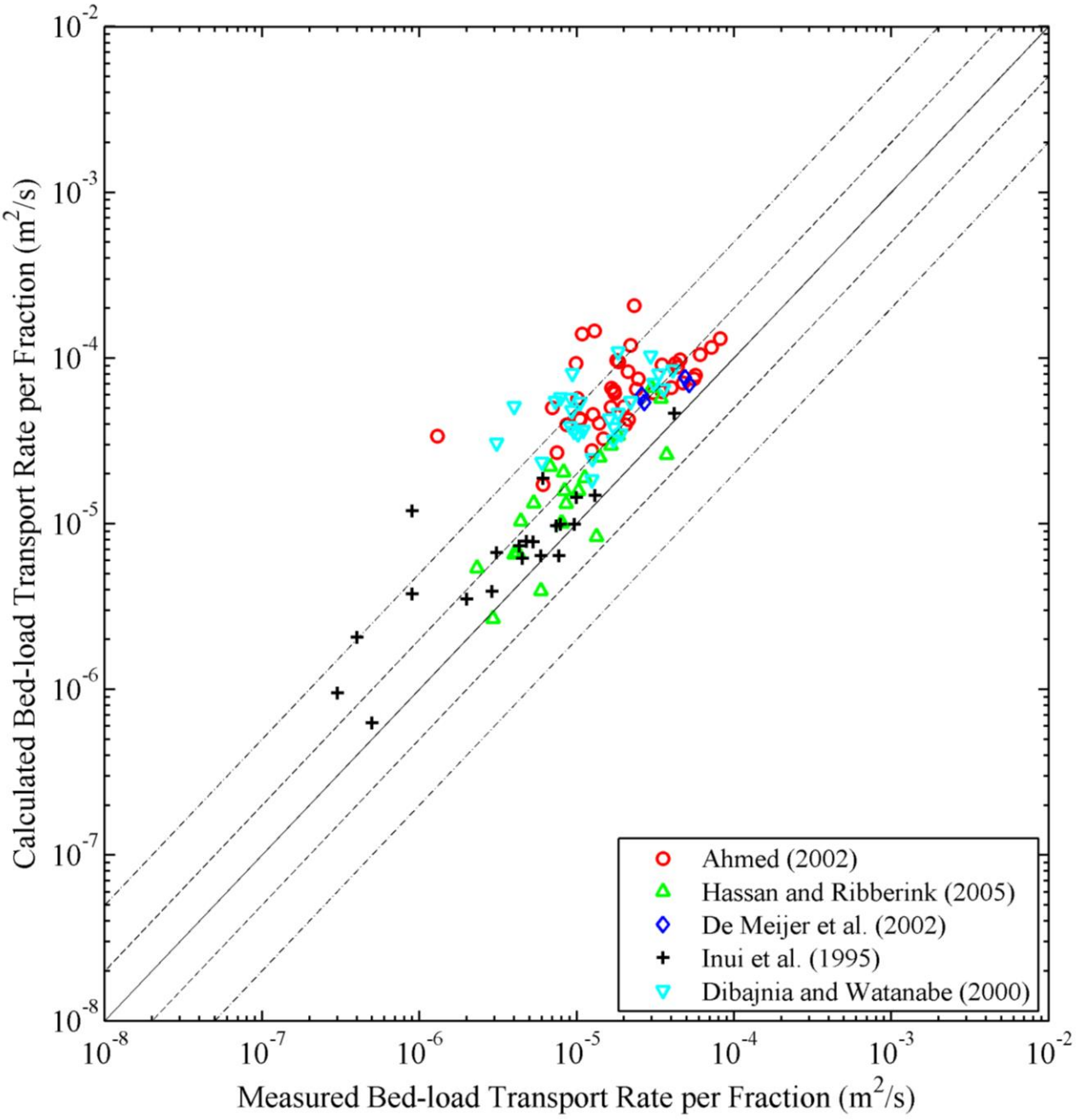

Figure 3.6 Comparison of Predicted and Measured Fractional Transport Rates of Nonuniform Bed Load ($k_s' = 3d_{90}$)

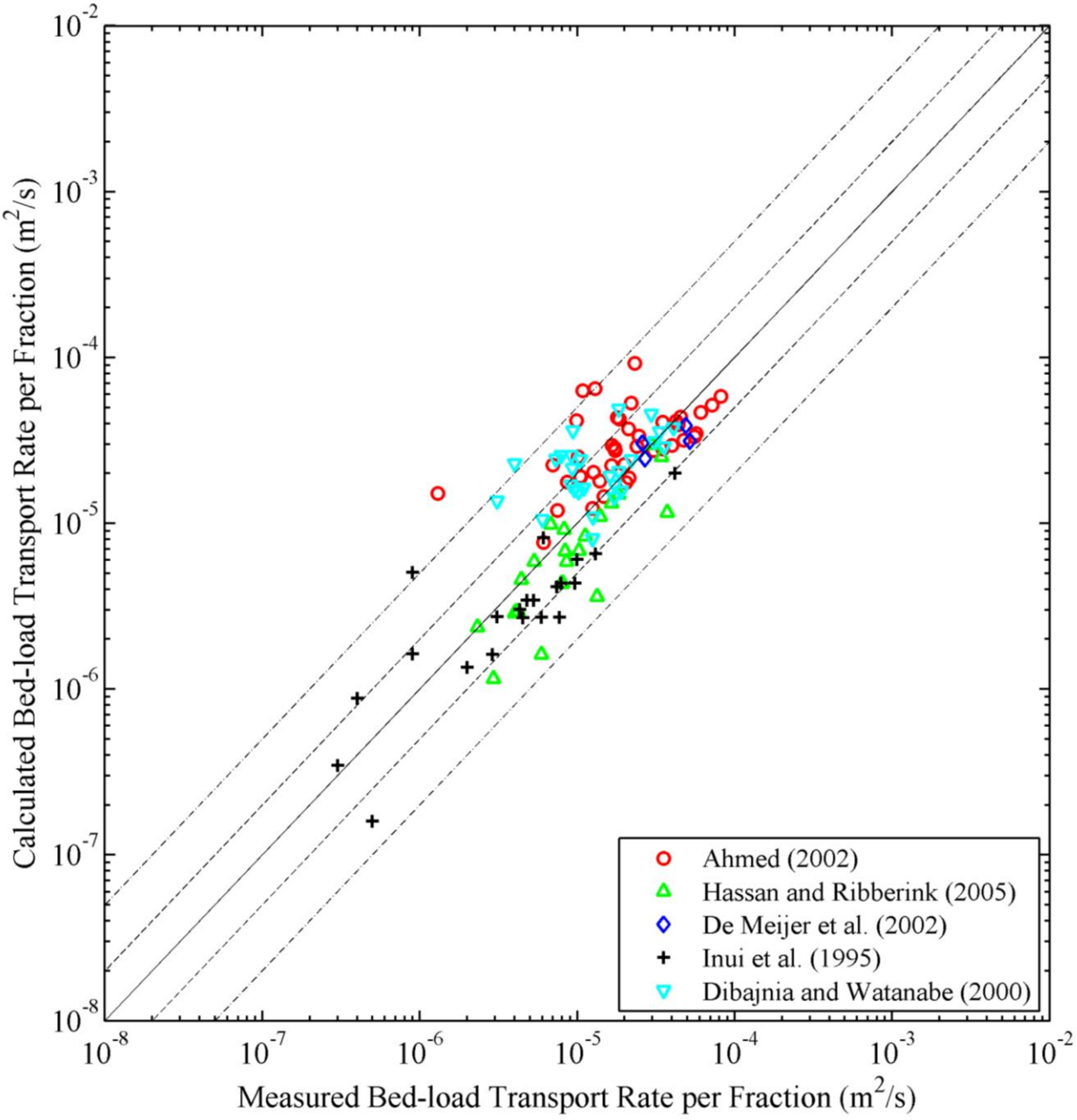

Figure 3.7 Comparison of Predicted and Measured Fractional Transport Rates of Nonuniform Bed Load ($k_s' = 1.5d_{90}$)

3.1.5.3 Test Using Uniform Suspended-Load Transport Data

The data sets compiled by Camenen and Larson (2007) for uniform or single-sized suspended-load transport are used to validate the present suspended-load transport capacity formula. Table 3.5 summarizes the current and wave conditions and sediment properties. Most of the data were measured in wave flumes or basin, and the data by Nielsen (1984) are obtained from field campaigns. All the data consider current and waves combined.

Table 3.5 Data Summary for Uniform Suspended-load Transport Experiments (Courtesy to Camenen and Larson, 2007)

Author(s)	Exp. facility	No. of runs	d_{50} (mm)	σ_g	h (m)	U_c (m/s)	H_{sig} (m)	T_w (s)
Nielsen (1984)	Field	27	0.16-0.49		0.80-1.58	0.04-0.54	0.42-0.80	5.3-12.9
Bosman (1982)	Wave flume	16	0.10	1.43	0.34-0.56	-0.34-0.32	0.18-0.28	1.7-2.0
Roelvink (1987)	Large Scale Flume	11	0.22-0.24	1.09–1.3	0.71-2.72	-0.11-0.01	0.47-0.73	5.12
Steetzel (1987)	Large Scale Flume	8	0.21	1.27	0.78-1.63	-0.18 ~ -0.07	0.65-1.10	5.4
Nieuwjaar and Kaaij (1987)	Flume	22	0.20-0.22	1.34–1.55	0.49-0.52	-0.45-0.45	0.07-0.19	2.4-2.6
Havinga (1992)	Basin	27	0.10	1.3	0.40- 0.43	0.10-0.32	0.07-0.14	2.1-2.3
Grasmeijer and Sistermans (1995)	Flume	46	0.10	1.38	0.29-0.32	-0.04-0.25	0.10-0.17	2.3
Sistermans (2002)	Flume	15	0.16-0.19	1.34–1.49	0.50-0.53	0.20-0.36	0.12-0.19	2.5-2.8

Fig. 3.8 compares the predicted and measured transport rates of uniform suspended load, and Table 3.6 shows the statistics of comparison. Unlike the developed bed-load transport Eq.

(3.28), the developed suspended-load transport rate Eq. (3.33) is not sensitive to the grain roughness height, whereas the coefficient A_r in Eq. (3.7) is an important parameter. The predictions of all cases are obtained using the default parameters in the formula described in Section 3.1.1, such as the grain roughness $k_s' = 3d_{90}$ and the coefficient A_r in Eq. (3.7) set as 12.0. The agreement between predictions and measurements is generally good, with 59% of the cases within a factor of 2 and 97% of the cases being predicted within a factor of 5 of the measured values. The logarithmic root-mean-square errors and bias are 0.329 and 0.068, respectively.

Table 3.6 Statistics for Predicted Transport Rate of Uniform Suspended Load

Conditions	% of Calculated Transport Rates in Error Range				Log(E_{rms})	Log(*bias*)
	0.8-1.25	0.67-1.5	0.5-2.0	0.2-5.0		
Uniform, Current and Waves	21.4	40.5	58.9	97.0	0.329	0.068

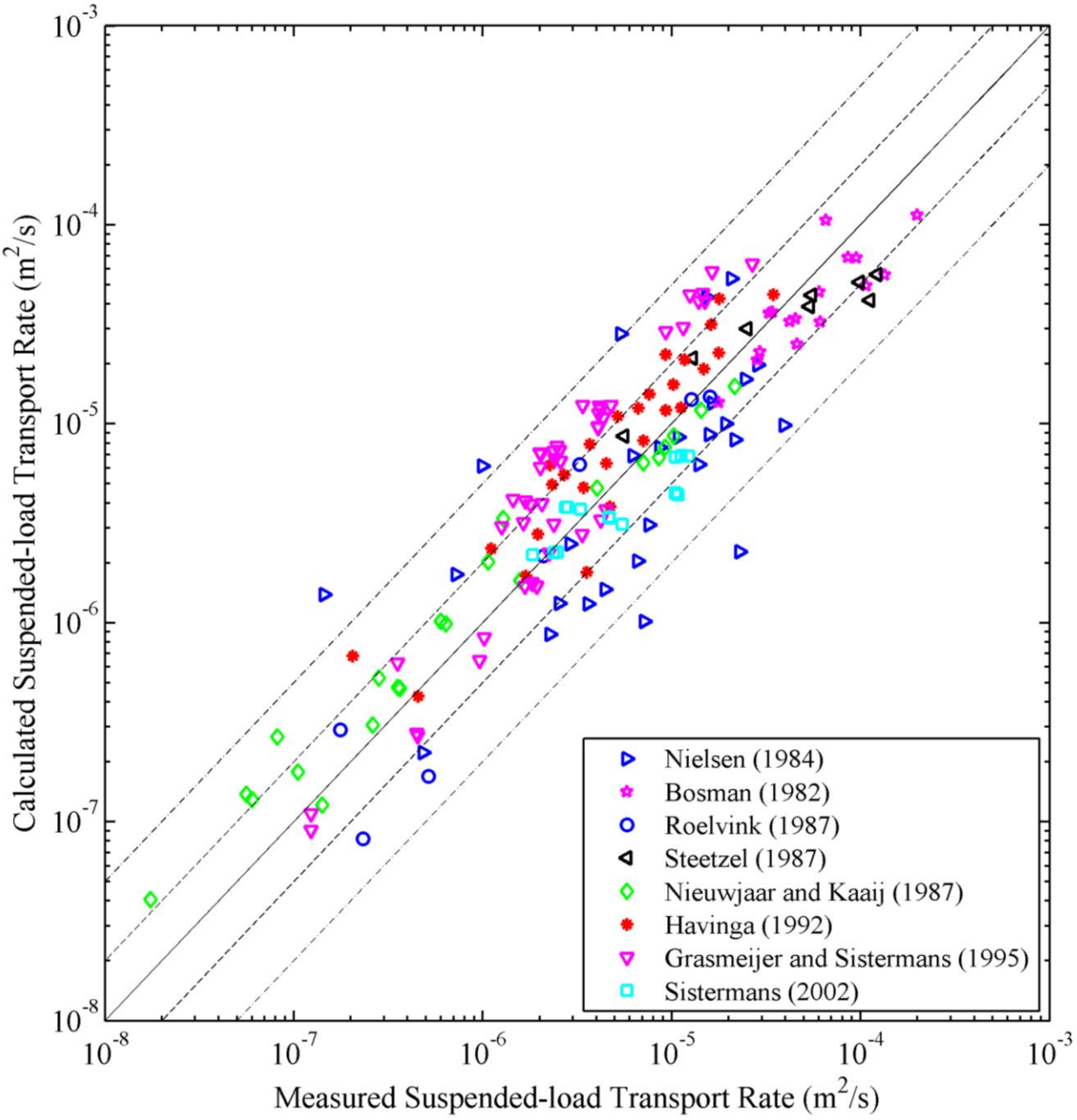

Figure 3.8 Comparison of Predicted and Measured Transport Rates of Uniform Suspended Load

3.1.5.4 Test Using Nonuniform Suspended-Load Transport Data

Due to limited data availability, only two sets of experiment data on nonuniform or multiple-sized suspended-load transport measured by Jacobs and Dekker (2000) and Sistermans (2001) are used to test the developed formula. Table 3.7 lists the current and wave conditions and sediment properties. Both sets of experiments were conducted in flumes. Each set had three runs, and all considered current and waves combined. The experiments of Sistermans (2001) used 13 size classes, all of which are used in this study. The experiments of Jacobs and Dekker (2000) used 9 size classes of bed sediment, but several coarse size classes were rarely moving so that 7 size classes are used here.

Table 3.7 Data Summary for Nonuniform Suspended-load Transport Experiments

Author(s)	Exp. facility	No. of runs	No. of sizes	d_{50} (mm)	σ_g	h (m)	U_c (m/s)	H_{sig} (m)	T_w (s)
Jacobs and Dekker (2000)	Flume	3	7	0.23 0.26 0.26	1.75 1.57 1.62	0.52 0.49 0.52	0.18 0.19 0.16	0.13 0.15 0.20	2.7 2.8 2.9
Sistermans (2001)	Flume	3	13	0.18 0.22 0.21	2.13 1.78 1.83	0.52 0.53 0.52	0.22	0.15 0.19 0.12	2.6 2.7 2.5

Fig. 3.9 compares the predicted and measured fractional transport rates of nonuniform suspended load. Table 3.8 shows the related statistics. The predictions for all cases are obtained using the default parameters of the formula described in Section 3.1.1, such as the grain roughness $k_s' = 3d_{90}$ and the coefficient A_r in Eq. (3.4) set as 12.0. The agreement between predictions and measurements is generally good, with about half of the cases being predicted within a factor of 2 of the measured values, and 85% of the cases within a factor of 5. The logarithmic root-mean-square

errors and bias are 0.435 and 0.058, respectively. The accuracy is reasonably good, considering that nonuniform sediment transport is much harder to maintain at equilibrium state for all size classes during the experiments than uniform sediment transport.

Table 3.8 Statistics for Predicted Fractional Transport Rate of Nonuniform Suspended Load

Conditions	% of Calculated Transport Rates in Error Range				Log(E_{rms})	Log(*bias*)
	0.8-1.25	0.67-1.5	0.5-2.0	0.2-5.0		
Nonuniform, Current and Waves	20.0	28.3	50.0	85.0	0.435	0.062

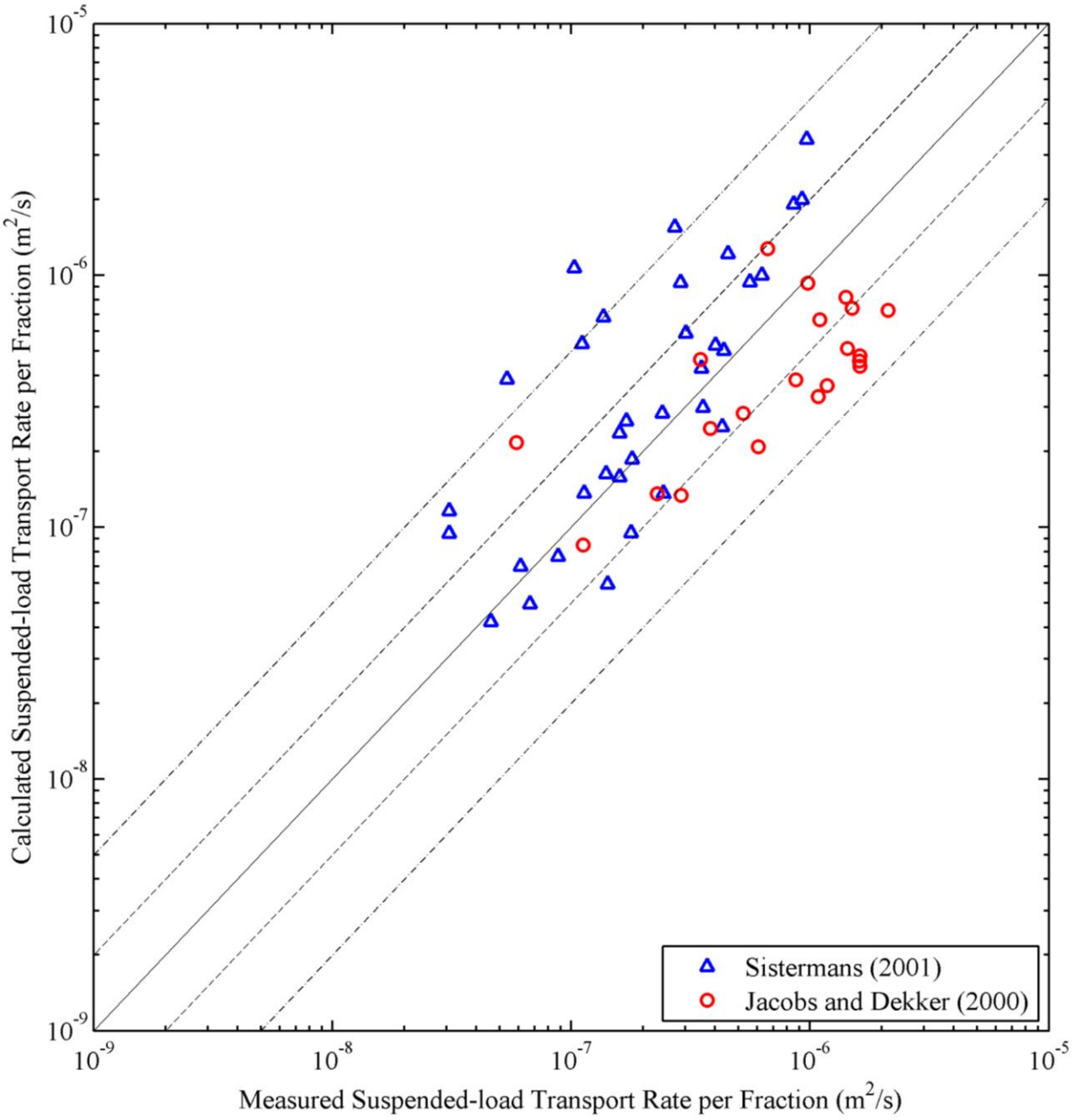

Figure 3.9 Comparison of Predicted and Measured Fractional Transport Rates of Nonuniform Suspended Load

3.2 Development of a New Formula for Near-bed Suspended Sediment Concentration

In order to quantitatively evaluate the bottom change and the entrainment rate of bed sediment into suspension caused by current and waves in coastal applications, it is more appropriate and accurate to use a 3-D model in which the local sediment is directly related to the near-bed suspended sediment concentration. Most of the formulas for near-bed suspended-load concentration have been developed for uniform material or suitable for river applications only. In this section, a new formula for near-bed suspended-load concentration under combined current and waves is presented.

3.2.1 Definition of Near-bed Suspended-load Concentration

The near-bed concentration of suspended load is defined as the sediment concentration at the upper bound of the bed-load layer or the interface between the bed-load and suspended-load layers, as shown in Fig. 3.10. It is often used to determine the near-bed sediment exchange flux or set as a reference for the sediment concentration profile along the water depth. Because the bed-load layer is usually very thin, the sediment concentration in the bed-load layer can be assumed approximately constant and equal to the near-bed concentration of suspended load. Therefore, the near-bed concentration of suspended load can be related to the bed-load transport rate, layer thickness, and velocity as follows (Einstein, 1950; van Rijn, 1984b; Wu, 2007),

$$c_{b*k} = \frac{q_{b*k}}{\delta U_{b,k}} \tag{3.36}$$

where c_{b*k} is the near-bed concentration of suspended load, δ is the bed-load layer thickness, and $U_{b,k}$ is the bed-load velocity. Methods to calculate the bed-load transport rate, layer thickness, and

velocity are discussed in the following subsections.

3.2.2 Bed-load Sediment Transport Rate

The bed-load transport rate can be calculated using existing empirical formulas. In this study, the bed-load transport rate formula of Wu *et al.* (2000b) (Eq. 3.1) is chosen because of its advantages over other formulas in literature, which has been listed in Section 3.1. In addition, it has been extended to multiple-sized sediment transport with current and waves for coastal applications and shown reliable predictions over all the test cases, which has been discussed in detail in the previous section.

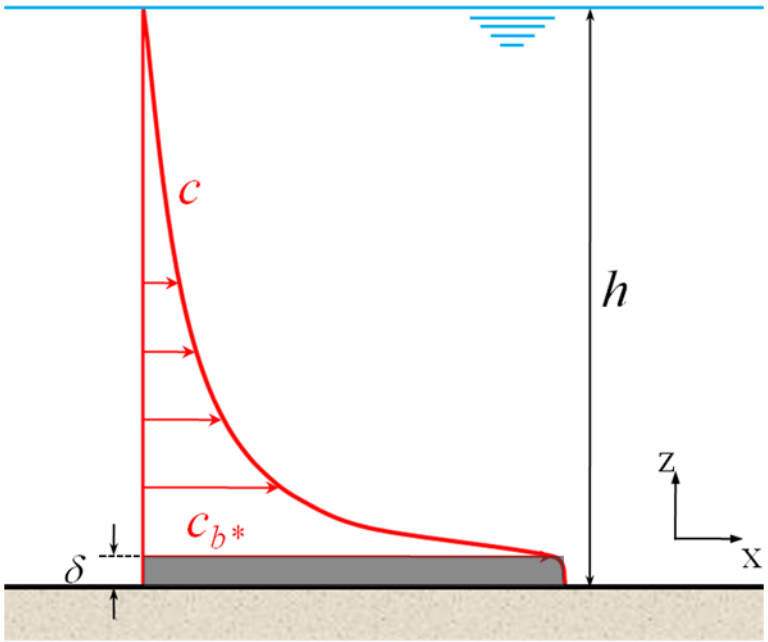

Figure 3.10 Definition of Near-bed Concentration

It is desirable to differentiate the onshore (Eq. 3.26) and offshore (Eq. 3.27) bed-load transport rates, then use Eq. (3.29) to calculate the net bed-load transport rate. However, due to the limit of data available and for simplicity, Eq. (3.1) is used to estimate the net bed-load transport rate without considering the onshore and offshore direction. Therefore, the total grain bed shear stress due to current and waves in Eq. (3.1) is calculated in the way similar to the total shear stress in Eq. (3.25):

$$\tau_b' = \sqrt{\tau_{b,c}'^2 + \tau_{b,wm}'^2 + 2\tau_{b,c}'\tau_{b,wm}'\cos\varphi} \tag{3.37}$$

where τ_b' is the total grain shear stress due to current and waves; $\tau_{b,c}'$ and $\tau_{b,wm}'$ are determined using Eqs. (3.11) and (3.15), respectively.

3.2.3 Reference Level

The reference level, also known as bed-load layer thickness, is the edge of the bed-load layer. The reference level is usually related to the sediment size, water depth, or bed form height. Most recently, van Rijn (2007c) suggested the reference level is the maximum value of half the wave-related and half the current-related bed roughness values with a minimum value of 0.01m.In this study, the reference level is defined as,

$$\delta = \max\left(2.0d_{50}, 0.01h, 0.5\Delta_r\right) \tag{3.38}$$

where the ripple height is calculated using the method of Raudkivi (2006) in the presence of current only, and the method of Soulsby and Whitehouse (2005) in the presence of only waves, and set as the larger value between the two methods in the case of currents and waves coexisted.

3.2.4 Bed-load Velocity

For simplicity, one can assume the bed-load velocity equals to the current velocity. However, lag exists between flow and bed-load transport. Bed load usually moves by rolling, sliding, and saltating, depending on flow and sediment conditions. Saltation is the dominant mode of bed-load transport, while rolling occurs only near the threshold of entrainment and between individual saltation jumps (Bridge and Dominic 1984). Van Rijn (1984a) investigated the characteristics of particle saltation and developed an empirical formula for the bed-load velocity. Wu (2007) recalibrated it using several sets of experiment data and revised it as follows

$$\frac{u_b}{\sqrt{(\rho_s/\rho-1)gd_k}}=1.64T_\tau^{0.5} \tag{3.39}$$

where T_τ is the non-dimensional excess bed shear stress defined as $T_\tau=\tau_b'/\tau_{cri,k}-1$. Eq. (3.39) was validated using data measured in cases of currents only. It is extended in this study to the cases of waves and currents coexisted.

3.2.5 Derivation of Near-bed Concentration

With the bed-load transport rate calculated by Eq. (3.1) and the bed-load velocity determined by Eq. (3.39), the near-bed concentration calculated by Eq. (3.36) can be simplified as

$$c_{b*k}=0.0032\frac{p_{bk}d_k}{\delta}\left(\frac{\tau_b'}{\tau_{cri,k}}-1\right)^{1.7} \tag{3.40}$$

where c_{b*k} is the volumetric concentration of suspended load at the reference level, and τ_b' is determined using Eq. (3.37).

3.2.6 Suspended Sediment Transport Rate

Due to the lack of measurement data for the near-bed sediment concentration which is usually in the unmeasured zone, it is difficult to validate directly the accuracy of the developed near-bed suspended-load concentration Eq. (3.40). However, there are a number of laboratory and field measurements of the suspended-load depth-averaged concentration or transport rate, as shown in the previous subsection. Therefore, one of the feasible ways to verify the accuracy of the developed near-bed concentration formula is to compare the measured suspended-load transport rate to that calculated by integrating the product between the suspended sediment concentration and current velocity along the vertical from the reference level (edge of bed-load layer) to the water surface (Fig. 3.11),

$$q_{s*k} = \int_{\delta}^{h} c_k u dz \tag{3.41}$$

where c_k and u are the local suspended-load concentration and current velocity, respectively, and z is the vertical coordinate above the bed.

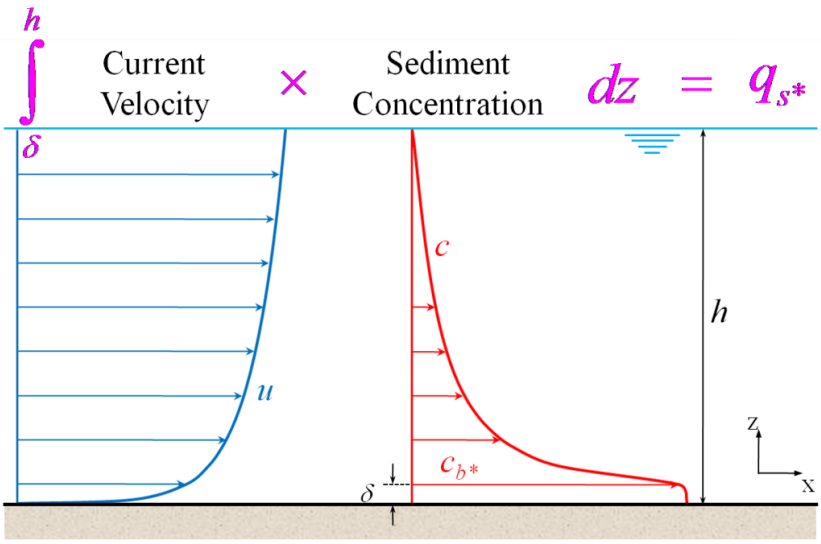

Figure 3.11 Definition of Suspended-load Transport Rate

3.2.6.1 Vertical Distribution of Current Velocity

In the presence of current only, the vertical distribution of current velocity can be approximately determined with two common methods. One is the power-law distribution of velocity,

$$u(z) = \frac{m+1}{m}\left(\frac{z}{h}\right)^{1/m} U_c \tag{3.42}$$

where z is the vertical coordinate above the bed and U_c is the depth-averaged current velocity. The other approach is the logarithmic distribution of velocity,

$$u(z) = 5.75 U_* \log\left(30.2\frac{z}{k_s'}\right) \tag{3.43}$$

where U_* is the bed shear velocity, which can be related to the depth-averaged current velocity by integrating Eq. (3.43) along the bed to the water surface,

$$U_* = \frac{(h - z_0)U_c}{5.75\int_{z_0}^{h} \log\left(30.2\frac{z}{k_s'}\right)dz} \tag{3.44}$$

where z_0 is the level at which the flow velocity is zero.

In the presence of waves, it should consider the effect of waves, e.g., an increase in the apparent roughness, in the current velocity profile. Van Rijn (1993) suggested a two-layer logarithmic distribution, which considers the effect of bed-form roughness inside the near-bed mixing layer (which is three times the thickness of wave boundary layer) and the effect of apparent roughness outside the near-bed mixing layer.

$$u(z)=\begin{cases}\dfrac{U_c \ln(30z/k_a)}{-1+\ln(30h/k_a)} & \text{for} \quad z \geq 3\delta_w \\ \dfrac{U_c \ln(90\delta_w/k_a)\ln(30z/k_{s,c})}{\ln(90\delta_w/k_{s,c})\left[-1+\ln(30h/k_a)\right]} & \text{for} \quad z < 3\delta_w \end{cases} \tag{3.45}$$

where $k_{s,c}$ is the current-related bed roughness, k_a is the apparent roughness related to wave-current interaction defined as $k_a = k_{s,c} \min\left[10, \exp(\gamma u_w / U_c)\right]$ with $\gamma = 0.8 + \varphi - 0.3\varphi^2$, δ_w is the maximum thickness of wave boundary layer equals to $0.072 A_w \left(A_w / k_{s,w}\right)^{-0.25}$ and $k_{s,w}$ is the wave-related bed roughness.

3.2.6.2 Vertical Distribution of Suspended-load Concentration

In this study, three existing distributions of suspended-load concentration, including Rouse (1937), van Rijn (1984b), and Williams et al. (1999) are used, among which the distribution of Williams et al. (1999) was validated by its developers using measured data under combined waves and currents.

The Rouse distribution can be expressed as,

$$\frac{c(z)}{c_{b*}} = \left(\frac{h/z - 1}{h/\delta - 1}\right)^{\frac{\sigma_s \omega_s}{\kappa U_*}} \tag{3.46}$$

where ω_s is the settling velocity, κ is von Karman constant with a value of 0.4, and σ_s is the Schmidt number, related to sediment size, concentration, etc. Several existing methods and new approaches to determine the Schmidt number are discussed in the following section.

The concentration profile proposed by van Rijn (1984b) is

$$\frac{c(z)}{c_{b*}} = \begin{cases} \left(\dfrac{h/z-1}{h/\delta-1}\right)^{\frac{\sigma_s\omega_s}{\kappa U_*}} & \text{for} \quad \dfrac{z}{h} < 0.5 \\ \left(\dfrac{1}{h/\delta-1}\right)^{\frac{\sigma_s\omega_s}{\kappa U_*}} \exp\left[-4\left(\sigma_s\omega_s/\kappa U_*\right)\left(z/h-0.5\right)\right] & \text{for} \quad \dfrac{z}{h} \geq 0.5 \end{cases} \tag{3.47}$$

The concentration profile for z<0.5h is exactly the Rouse distribution.

The distribution of Williams et al. (1999) can be expressed as

$$\frac{c(z)}{c_{b*}} = \left(\frac{z + L_s\alpha_{wc}}{\delta + L_s\alpha_{wc}}\right)^{-\alpha_{wc}} \tag{3.48}$$

where $\alpha_{wc} = \omega_s \Big/ \left[\kappa\left(\overline{U}_{*wcR} + U_{*wG}\right)\right]$, $\overline{U}_{*wcR}$ is the time-averaged bed-shear velocity for ripple-scale roughness, U_{*wG} is the peak wave-only bed-shear velocity for grain-scale roughness, and L_s is the vertical length scale for the suspended-load concentration distribution defined by Nielsen (1992), which is determined as

$$L_s = \begin{cases} 0.075\Delta_r\, A_w\omega/\omega_s & \text{for } A_w\omega/\omega_s < 18 \\ 1.4\Delta_r & \text{for } A_w\omega/\omega_s \leq 18 \end{cases} \tag{3.49}$$

The parameters $\overline{U}_{*wcR}$ and U_{*wG} are calculated following Williams et al. (1999).

3.2.6.3 New Approaches to Determine the Schmidt Number

There are several existing methods in literature to determine the Schmidt number. Brush et al. (1962), Matyukhin and Prokofyev (1996), and Majumdar and Carstens (1967) experimentally showed that $\sigma_s \cong 1$ for fine particles and $\sigma_s > 1$ for coarse particles. Einstein and Chien (1954) suggested that σ_s should be smaller than 1 and calculated as

$$\frac{\sigma_s \omega_s}{\kappa U_*} = \frac{\omega_s / \kappa U_*}{\exp\left[-L^2 \left(\omega_s / \kappa U_*\right)^2 / \pi\right] + \left(\omega_s / \kappa U_*\right) \frac{2L}{\sqrt{2\pi}} \int_0^{\sqrt{2\pi} L(\omega_s / \kappa U_*)} e^{-x^2/2} dx} \tag{3.50}$$

where L = log (1+BK) with BK = 0.3. Van Rijn (1984b) also proposed a formula to determine the Schmidt number,

$$\frac{1}{\sigma_s} = \begin{cases} 1.02 & \omega_s / U_* \le 0.1 \\ 1 + 2\left(\omega_s / U_*\right)^2 & \text{for} \quad 0.1 < \omega_s / U_* < 1 \\ 3 & \omega_s / U_* \ge 1 \end{cases} \tag{3.51}$$

Einstein and Chien (1954) obtained a relation between $\omega_s/(\kappa U_*)$ and $\sigma_s \omega_s/(\kappa U_*)$ shown in Fig. 3.12. Based on the experimental data, through the linear and nonlinear regressions, a linear and a polynomial curve are proposed respectively to fit the data. The linear fitting curve is expressed as

$$\frac{\sigma_s \omega_s}{\kappa U_*} = 0.8258 \frac{\omega_s}{\kappa U_*} + 0.054 \tag{3.52}$$

Thus the Schmidt number can be calculated as

$$\sigma_s = 0.054 \frac{\kappa U_*}{\omega_s} + 0.8258 \tag{3.53}$$

The polynomial fitting curve is only valid with $0.02 \le \omega_s/U_* \le 2.04$ and expressed as

$$\frac{\sigma_s \omega_s}{\kappa U_*} = -0.0073 \left(\frac{\omega_s}{\kappa U_*}\right)^3 + 0.937048 \left(\frac{\omega_s}{\kappa U_*}\right) - 0.03969 \tag{3.54}$$

where the ratio between $\omega_s/(\kappa U_*)$ and $\sigma_s \omega_s/(\kappa U_*)$ is assumed to be constant with $\omega_s/U_* < 0.0169$ or $\omega_s/U_* > 2.04$. According to this relation, the Schmidt number can be determined as

$$\sigma_s = \begin{cases} 0.14323 & \omega_s / U_* < 0.02 \\ -0.0072\left(\omega_s / \kappa U_*\right)^2 - 0.03969\left(\omega_s / \kappa U_*\right)^{-1} + 0.937048 & \text{for } 0.02 \le \omega_s / U_* \le 2.04 \\ 0.73939 & \omega_s / U_* > 2.04 \end{cases} \quad (3.55)$$

These two new approaches will be compared with the methods of Einstein and Chien (1954) and Van Rijn (1984b) in Section 3.2.7.

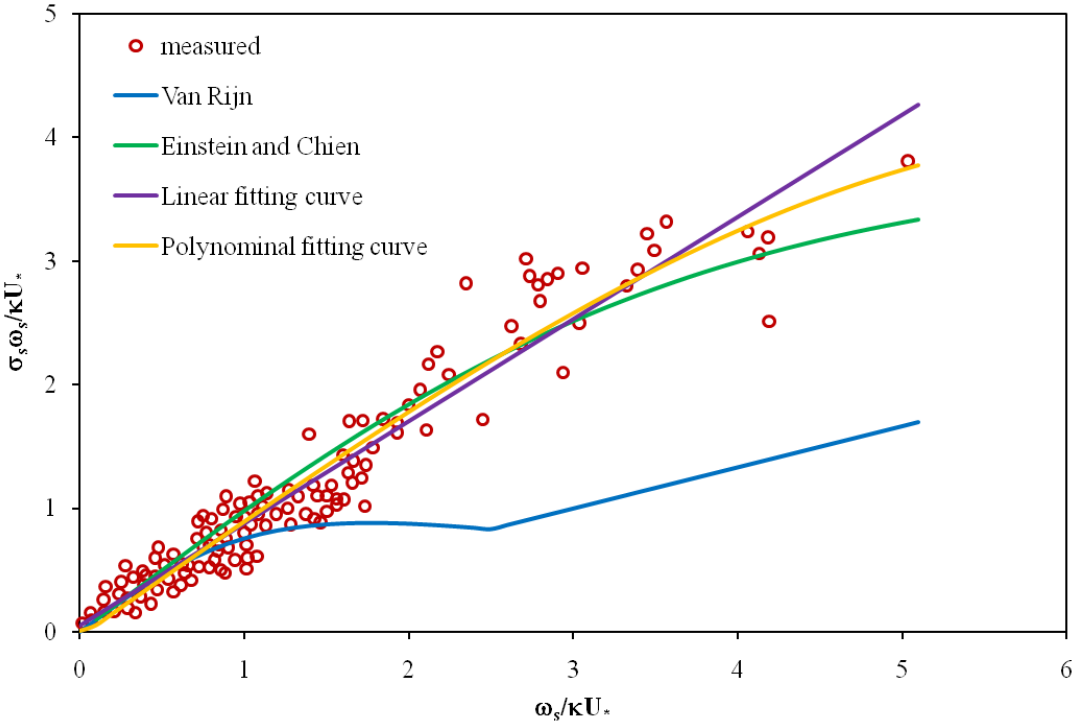

Figure 3.12 Relation between $\omega_s/(\kappa U_*)$ and $\sigma_s\omega_s/(\kappa U_*)$

3.2.7 Test of the Developed Formula

In this section, the suspended-load transport rates are calculated using Eq. (3.41) with the developed near-bed concentration formula and compared with the measurement data. The dataset includes single- and multiple-sized suspended sediment transport data under current only and

current-waves coexisted situations collected from literature.

3.2.7.1 Test Using Suspended-load Transport Data under Current Only

A large set of uniform total-load data was selected form Brownlie's (1981) compilation to test the developed formula. The non-uniform sediment data collected by Toffaletti (1968) were also used to test the formula, including experimental data observed by Nomicos, Einstein-Chien, and Vanoni-Brooks, and field data in the Rio Grande, Middle Loup, Niobrara, and Mississippi Rivers. Because the measurement data are total load instead of suspended load only, the suspended-load transport rate calculated by the developed formula was combined with the bed-load transport rate calculated by Eq. (3.1) to obtain the total load. The power-law current velocity distribution in Eq. (3.42), the Rouse (1937) distribution of suspended-load concentration in Eq. (3.46), and the near-bed suspended-load concentration in Eq. (3.40) are used in calculating the suspended-load transport rate with Eq. (3.41). The polynomial fitting curve Eq. (3.55) is used to determine the Schmidt number.

Figs. 3.13 and 3.14 compare the predicated and measured transport rates of uniform and non-uniform total load under current only, respectively. Table 3.9 shows the statistics of comparison. For uniform cases, about 77% of the test cases are predicted within a factor of 2 of the measured values and about 95% of the cases are within a factor of 5. For nonuniform cases, about 48% of the test cases are predicted within a factor of 2 of the measured values and about 85% of the cases are within a factor of 5. The logarithmic root-mean-square errors are 0.353 and 0.559 for uniform and nonuniform cases, respectively. The logarithmic bias are 0.087 and 0.131 for uniform and nonuniform cases, respectively. The results of nonuniform cases are not as good as those of

uniform cases but reasonable because of the complex interaction among different size classes.

Table 3.9 Statistics for Predicted Transport Rate of Total Load under Current Only

Conditions	% of Calculated Transport Rates in Error Range				Log(E_{rms})	Log(*bias*)
	0.8-1.25	0.67-1.5	0.5-2.0	0.2-5.0		
Uniform, Current only	29.5	55.3	77.3	94.7	0.353	0.087
Nonuniform, Current only	18.2	30.7	48.4	84.5	0.559	0.131

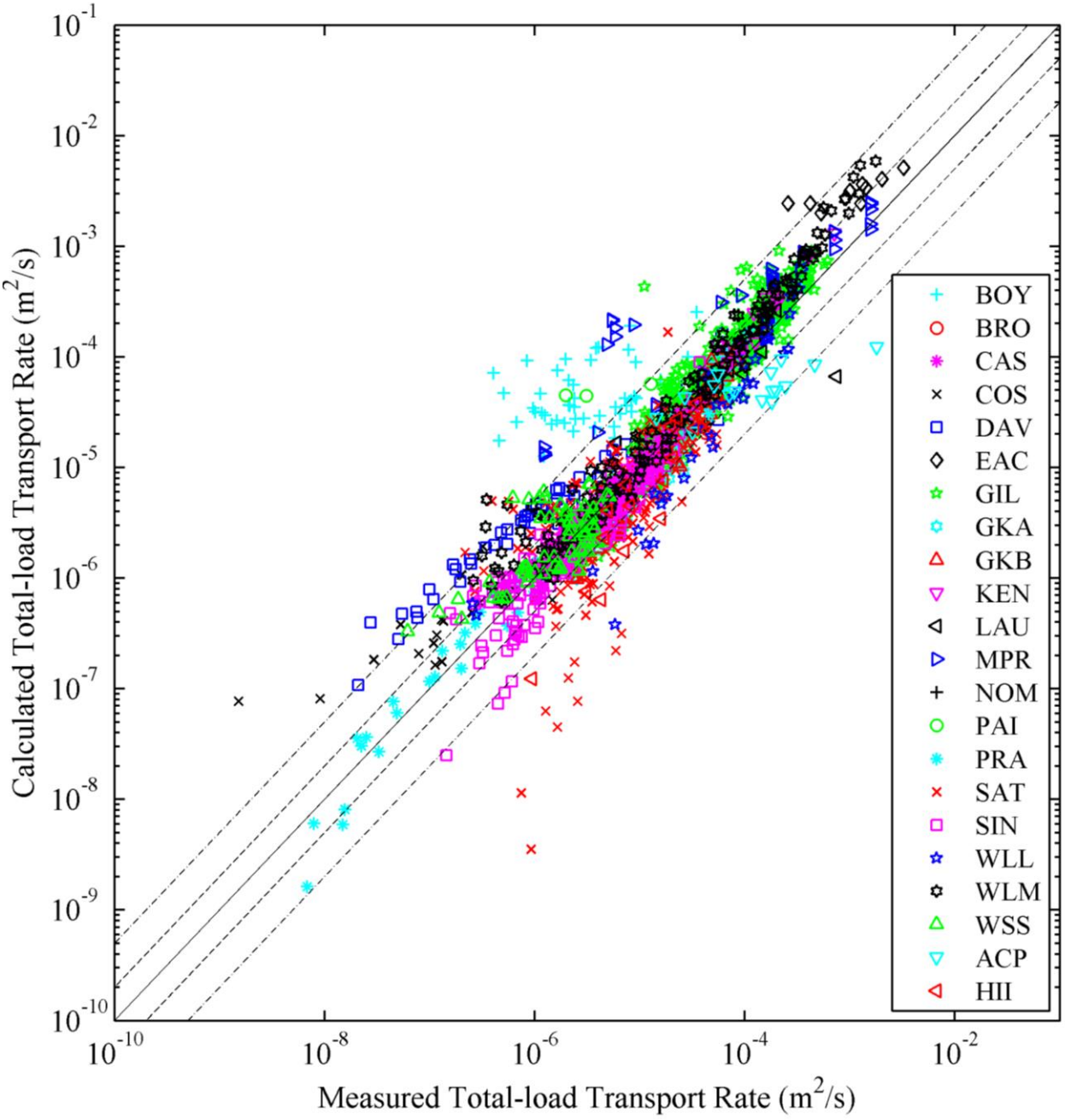

Figure 3.13 Comparison of Predicted and Measured Transport Rates of Uniform Total Load under current only

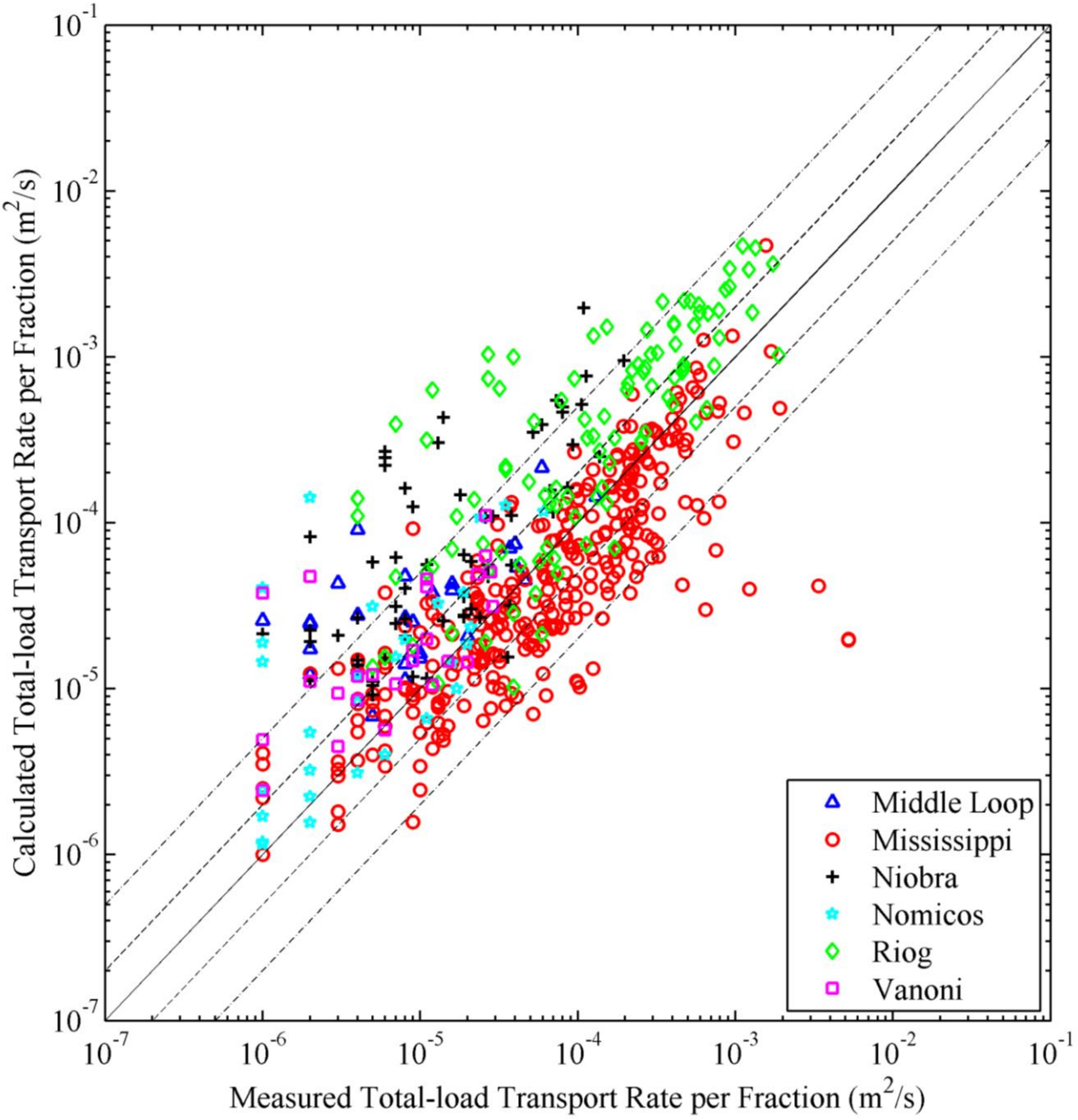

Figure 3.14 Comparison of Predicted and Measured Fractional Transport Rates of Non-uniform Total Load under current only

3.2.7.2 Test Using Suspended-load Transport Data under Combined Current and Waves

The data sets compiled by Camenen and Larson (2007) for uniform suspended-load transport listed in Table 3.5 are used to validate the present near-bed suspended-load concentration formula. Due to limited data availability, only two sets of experiment data on nonuniform suspended-load transport measured by Jacobs and Dekker (2000) and Sistermans (2001) listed in Table 3.7 are used to test the performance of the developed formula on nonuniform sediment transport. In the results presented below, the van Rijn's (1993) current velocity distribution in Eq. (3.44), the suspended-load concentration distribution of William et al. (1999) in Eq. (3.48), and the near-bed suspended-load concentration in Eq. (3.40) are used in calculating the suspended-load transport rate in Eq. (3.41).

Figs. 3.15 and 3.16 show the comparisons of predicated and measured transport rates of uniform and non-uniform suspended load under combined current and waves, respectively. Table 3.10 shows the performance statistics. The coefficient A_r in Eq. (3.7) is set as 12.0 for all the test cases. Because the near-bed suspended-load concentration is related to the bed load, the calculated suspended-load transport rate is also related to the grain roughness height. The overall best value of grain roughness is $3d_{90}$ for all the uniform and nonuniform cases. For uniform cases, more than 70% of the test cases are predicted within a factor of 2 of the measured values and more than 90% of the cases are within a factor of 5. For nonuniform cases, about 47% of the test cases are predicted within a factor of 2 of the measured values and about 87% of the cases are within a factor of 5. For uniform cases, the logarithmic root-mean-square errors and bias are 0.386 and -0.036, respectively. For nonuniform cases, the logarithmic root-mean-square errors and bias are 0.404 and 0.121, respectively. This accuracy is generally acceptable for sediment transport, particularly

under current and waves, which are very complex and little understood. Additional errors are from the bed shear stress, which is difficult to measure when waves are included and has to be determined using empirical models of bed roughness. On the other hand, the data sets of nonuniform sediment transport under combined current and waves are very limited. Only two sets of experiment data are found from literature to test the developed formula. It is absolutely meaningful to test the developed formula with more laboratory and field experiments of nonuniform sediment transport under various conditions of current and waves in order to obtain a more reliable statistical analysis.

Table 3.10 Statistics for Predicted Transport Rate of Suspended Load under Combined Current and Waves

Conditions	% of Calculated Transport Rates in Error Range				Log(E_{rms})	Log(*bias*)
	0.8-1.25	0.67-1.5	0.5-2.0	0.2-5.0		
Uniform, Current +Waves	24.8	51.5	72.7	93.3	0.386	-0.036
Nonuniform, Current + Waves	16.7	31.7	46.7	86.7	0.404	0.121

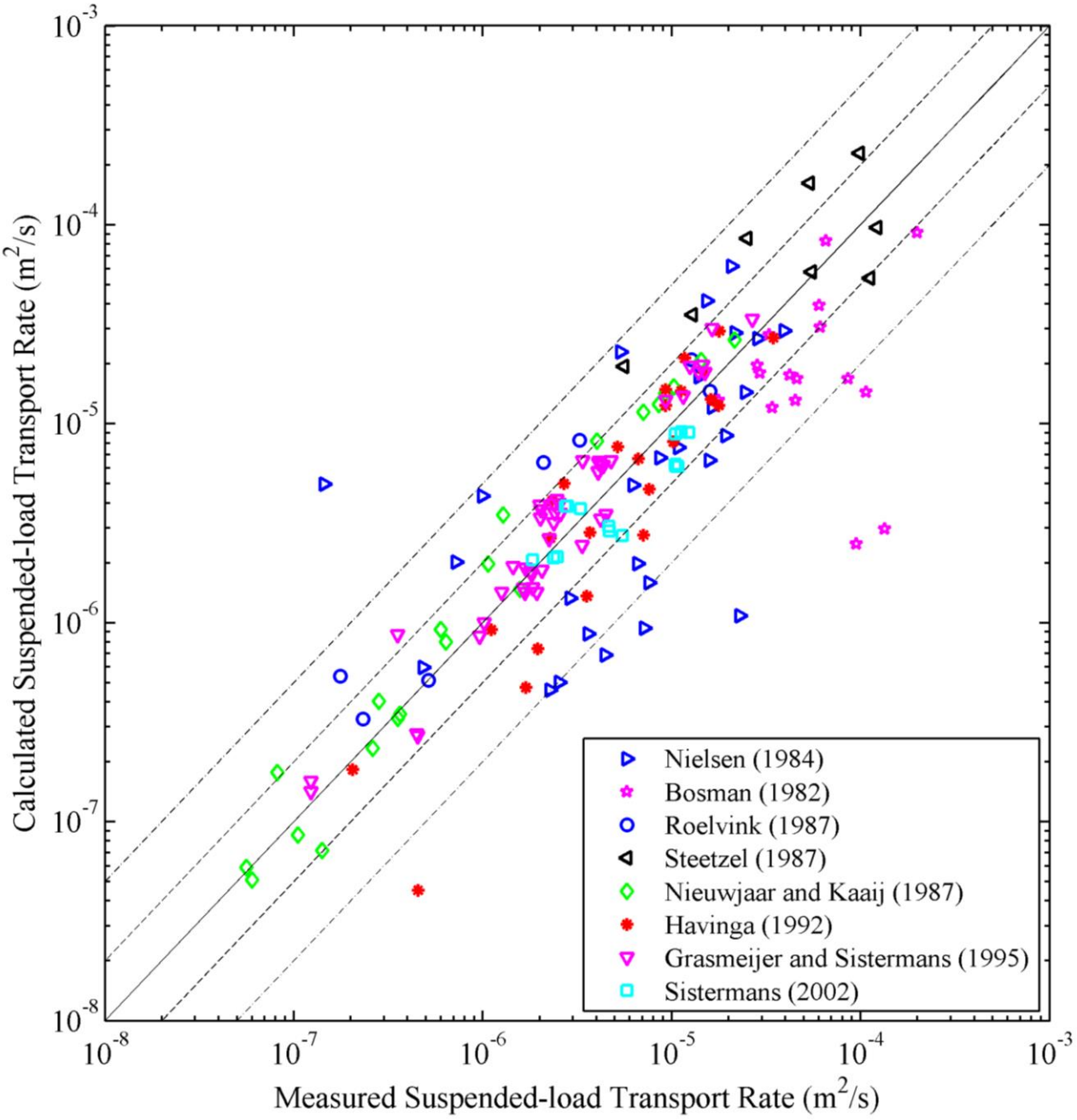

Figure 3.15 Comparison of Predicted and Measured Transport Rates of Uniform Suspended Load under Combined Current and Waves

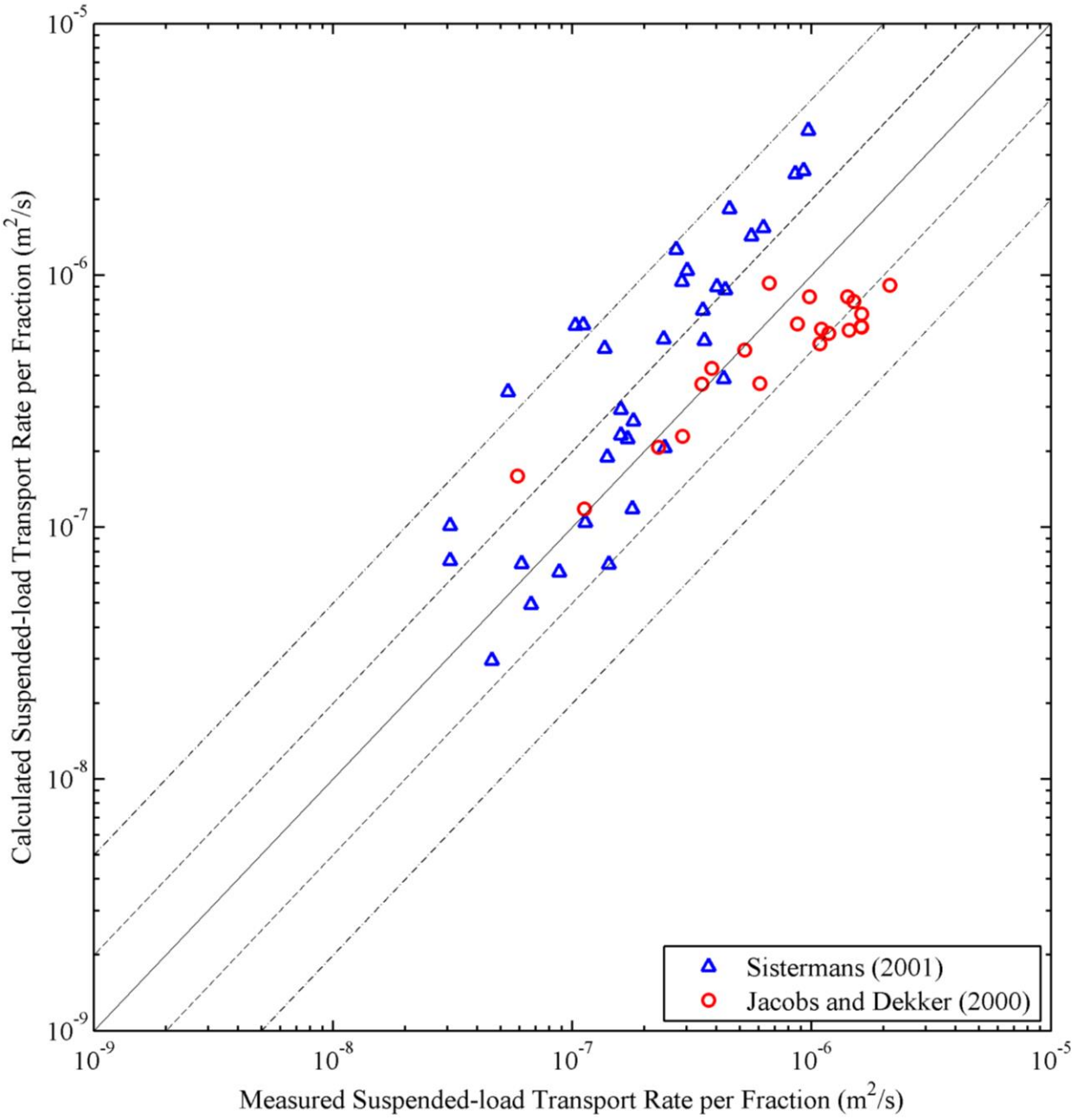

Figure 3.16 Comparison of Predicted and Measured Fractional Transport Rates of Non-uniform Suspended Load under Combined Current and Waves

3.3 Comparison of the Developed Formulas with Other Formulas

To better analyze the performance of the enhanced Wu et al. bed-load transport rate formula, suspended-load transport rate formula, and the near-bed suspended-load concentration formula, several coastal sediment transport formulas are tested with the same uniform and nonuniform dataset presented above (Tables 3.1, 3.3, 3.5, and 3.7) and compared with developed formulas. For uniform bed-load data, the formulas of Bailard (1981), Camenen and Larson (2007), Dibajnia and Watanabe (1992), Ribberink (1998), van Rijn (2007a), and van der A et al. (2013) are used. For nonuniform bed-load data, the formulas include Dibajnia and Watanabe (1996), Hassen et al. (2001), van Rijn (2007c), and van der A et al. (2013). The existing formulas of Bailard (1981), Camenen and Larson (2007), and van Rijn (2007b) are tested with the uniform suspended-load data and compared with the developed suspended-load transport rate formula and near-bed suspended-load concentration formula, among which the van Rijn (2007b) is also tested with nonuniform suspended-load data. All these existing formulas have been listed and reviewed in Section 2.3.

Figs. 17 and 18 compare the transport rates calculated by these formulas with measurements under waves only and combined current and waves for uniform bed-load data, respectively. Fig. 19 shows the transport rates calculated by these formulas with measurement under combined current and waves for nonuniform bed-load data. Table 3.11 shows the statistical analysis for predicated bed-load transport rates by using different formulas. For uniform bed-load sediment transport under waves only, the Camenen and Larson (2007) formula, van Rijn (2007a) formula, and the developed formula have relatively good predictions over theother compared formulas. The logarithmic root-mean-square and bias of the developed formula are the smallest

among all the compared formulas. The formulas of Dibajnia and Watanabe (1992) and van de A et al. (2013) don't have so good predictions as other formulas. For uniform bed-load sediment transport under combined current and waves, the Ribberink (1998) formula, van Rijn (2007a) formula, and the developed formula have more than 70% of the cases are within a factor of 5. For nonuniform bed-load sediment transport under combined current and waves, the Hassen et al. (2001) formula, van Rijn (2007c) formula, and the developed formula have more than 70% of the cases are within a factor of 5. The predicted values given by the developed formula have the best agreement with the measured data, showing the smallest logarithmic root-mean-square and bias. In overall, the formulas of Camenen and Larson (2007), Ribberink (1998), the Hassen et al. (2001), and Van Rijn (2007a, c) show reasonable predictions. The Dibajnia and Watanabe (1992, 1996) cannot provide a good agreement between predicted and measured transport rates for all the test cases.

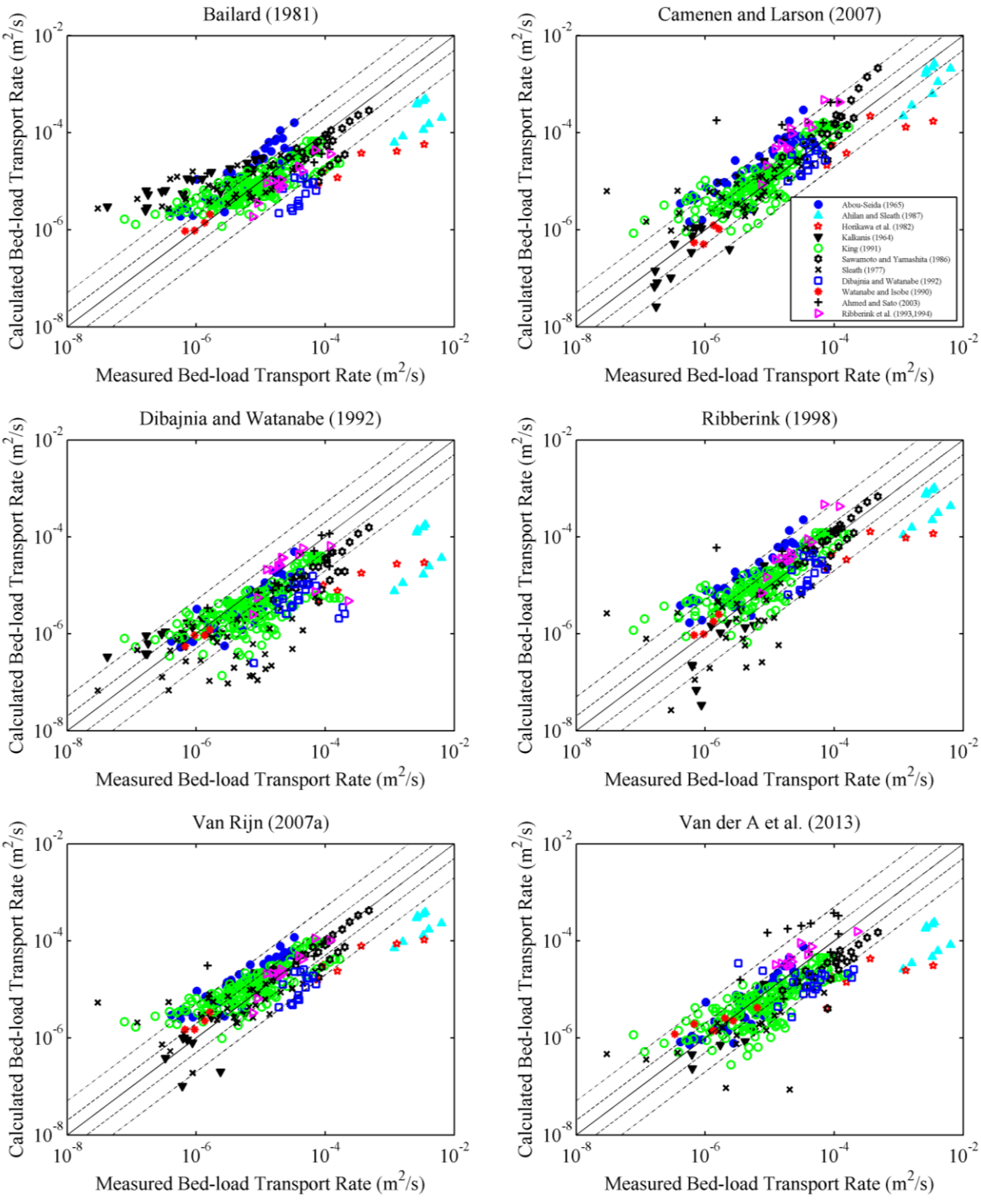

Figure 3.17 Comparison of Predicted and Measured Transport Rates of Uniform Bed Load with Waves Only using Different Foumulas

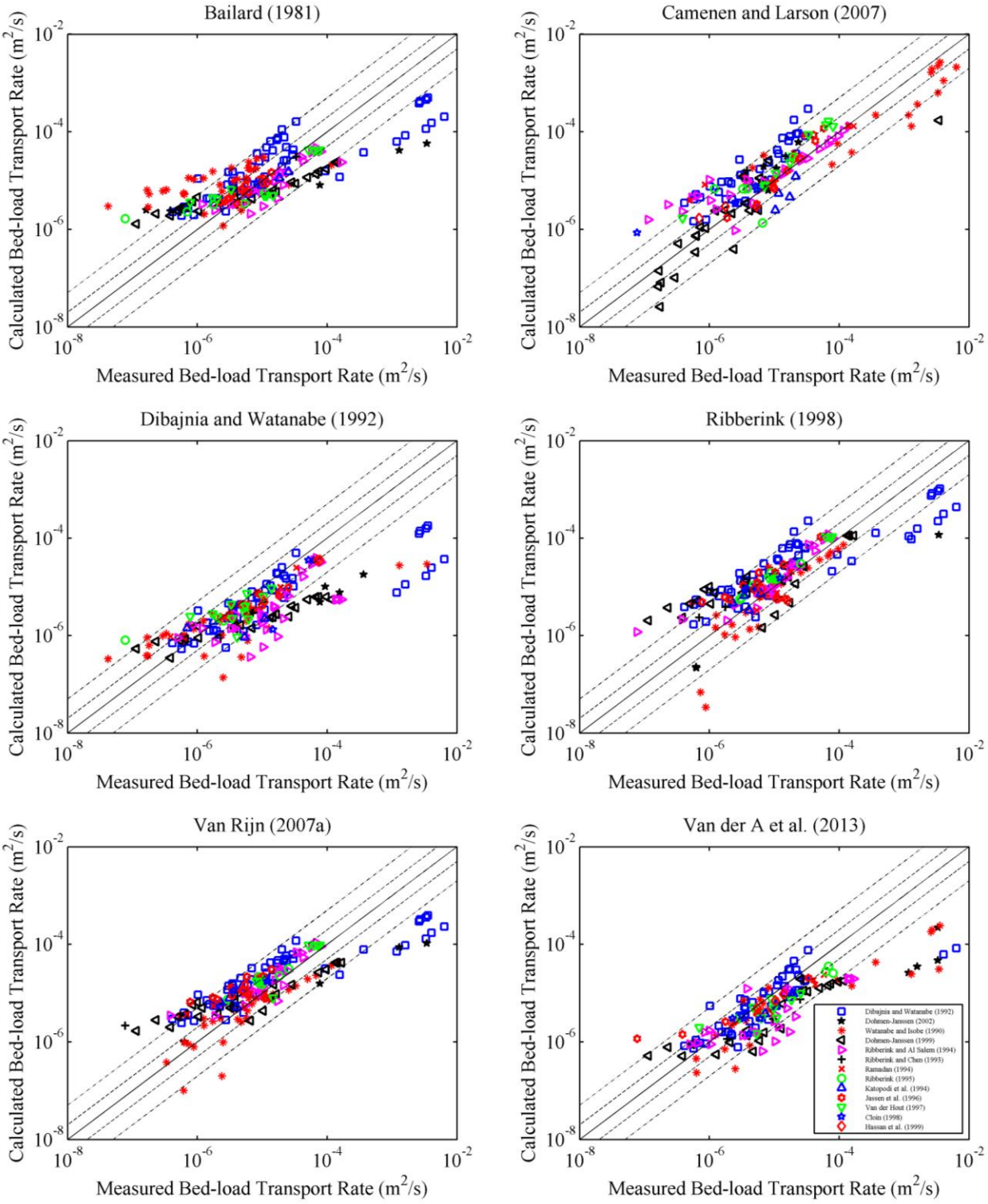

Figure 3.18 Comparison of Predicted and Measured Transport Rates of Uniform Bed Load with Combined Current and Waves using Different Foumulas

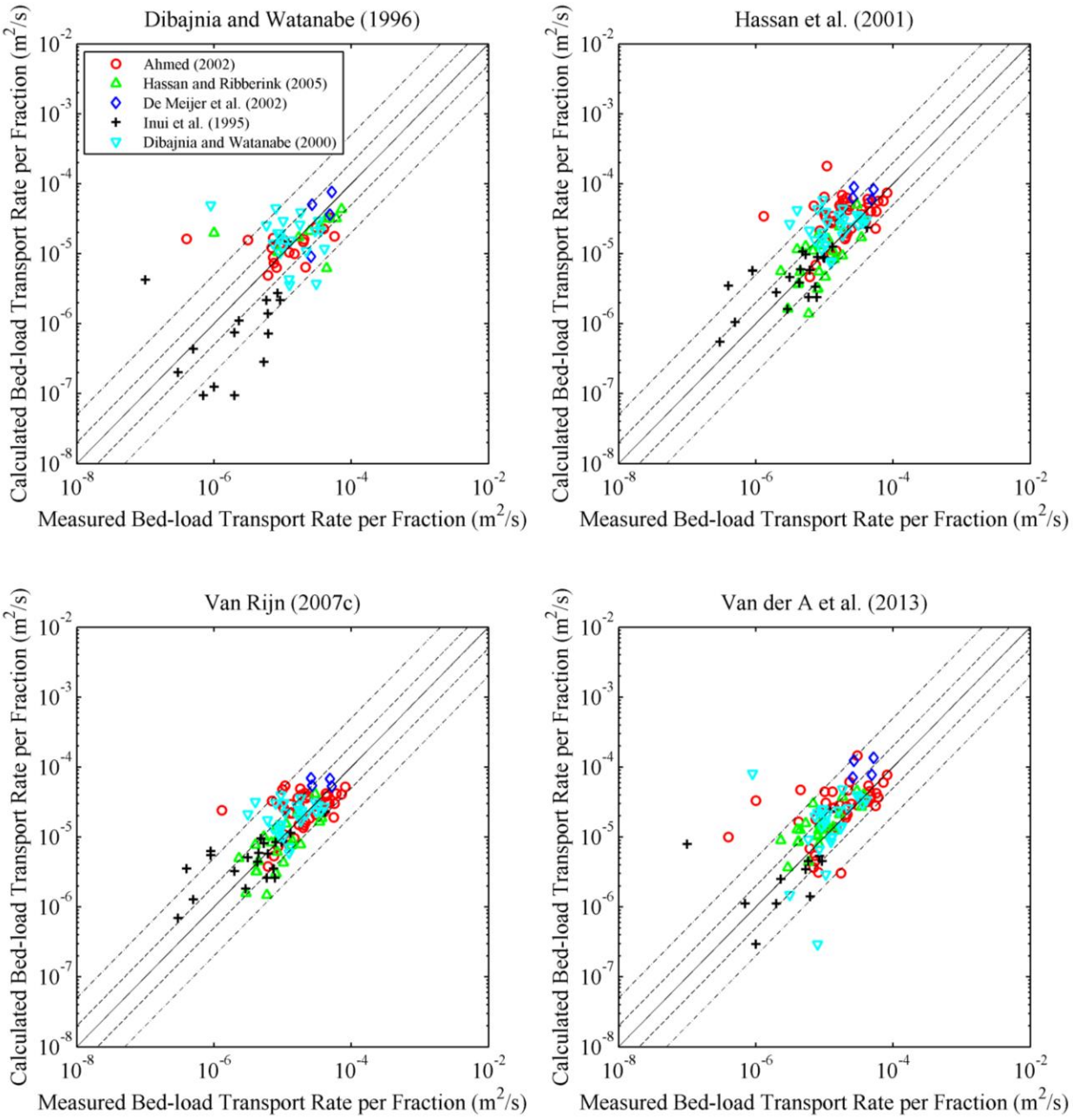

Figure 3.19 Comparison of Predicted and Measured Transport Rates of Nonuniform Bed Load with Combined Current and Waves using Different Foumulas

Table 3.11 Statistics for Predicted Bed-load Transport Rates using Different Formulas

Conditions	Formulas	% of Calculated Transport Rates in Error Range				Log(E_{rms})	Log(*bias*)
		0.8-1.25	0.67-1.5	0.5-2.0	0.2-5.0		
Uniform Waves	Bailard (1981)	18.7	30.1	45.1	74.4	0.584	0.021
	Camenen and Larson (2007)	19.2	30.3	52.8	83.9	0.475	1.941
	Dibajnia and Watanabe (1992)	12.4	24.9	40.7	73.1	0.713	-0.430
	Ribberink (1998)	14.8	28.5	49.5	79.3	0.494	0.083
	Van Rijn (2007a)	17.4	29.5	47.4	81.1	0.496	0.073
	Van der A et al. (2013)	12.1	24.4	41.2	73.3	0.539	-0.204
	Eq. (3.26) or (3.28)	17.1	34.7	52.8	86.5	0.429	-0.067
Uniform Current+Waves	Bailard (1981)	10.5	22.8	38.8	76.8	0.470	0.074
	Camenen and Larson (2007)	16.0	26.2	45.1	65.0	0.403	0.107
	Dibajnia and Watanabe (1992)	11.8	21.9	35.0	57.0	0.875	-0.555
	Ribberink (1998)	19.4	34.2	49.8	71.3	0.634	0.155
	Van Rijn (2007a)	15.6	27.0	45.6	73.0	0.510	-0.163
	Van der A et al. (2013)	17.3	25.7	37.6	54.9	0.616	-0.133
	Eq. (3.28)	23.2	34.2	48.5	75.1	0.515	0.017
Nonuniform Current+Waves (Fractional Rate)	Dibajnia and Watanabe (1996)	10.7	24.8	36.2	56.4	0.532	0.011
	Hassen et al. (2001)	20.1	31.5	45.6	71.1	0.399	0.168
	Van Rijn (2007c)	16.8	30.2	54.4	73.8	0.313	0.063
	Van der A et al. (2013)	18.1	30.9	45.0	67.1	0.476	0.151
	Eq. (3.28)	23.5	38.3	57.0	75.2	0.307	0.051

Figs 3.20 and 3.21 compare the suspended-load transport rates calculated by the different tested formulas with measurements under combined current and waves for uniform and nonuniform cases, respectively. Table 3.12 compares the performance statistics of these formulas on predicting the suspended-load transport rates under current and waves. For uniform cases, the predications given by van Rijn (2007b), Eq. (3.33), and Eq. (3.40) are with a good agreement with

the measurements, more than 50% of the test cases are within and more than 90% of the test cases are within factor of 5.These three methods have comparable performance and are better than the methods of Bailard (1991) and Camenen and Larson (2007). For nonuniform cases, Eq. (3.33) and Eq. (3.40) perform better than van Rijn's (2007c) method. In comparison of Eq. (3.33) and Eq. (3.41) with the developed near-bed concentration Eq. (3.40), both methods have comparable performance.

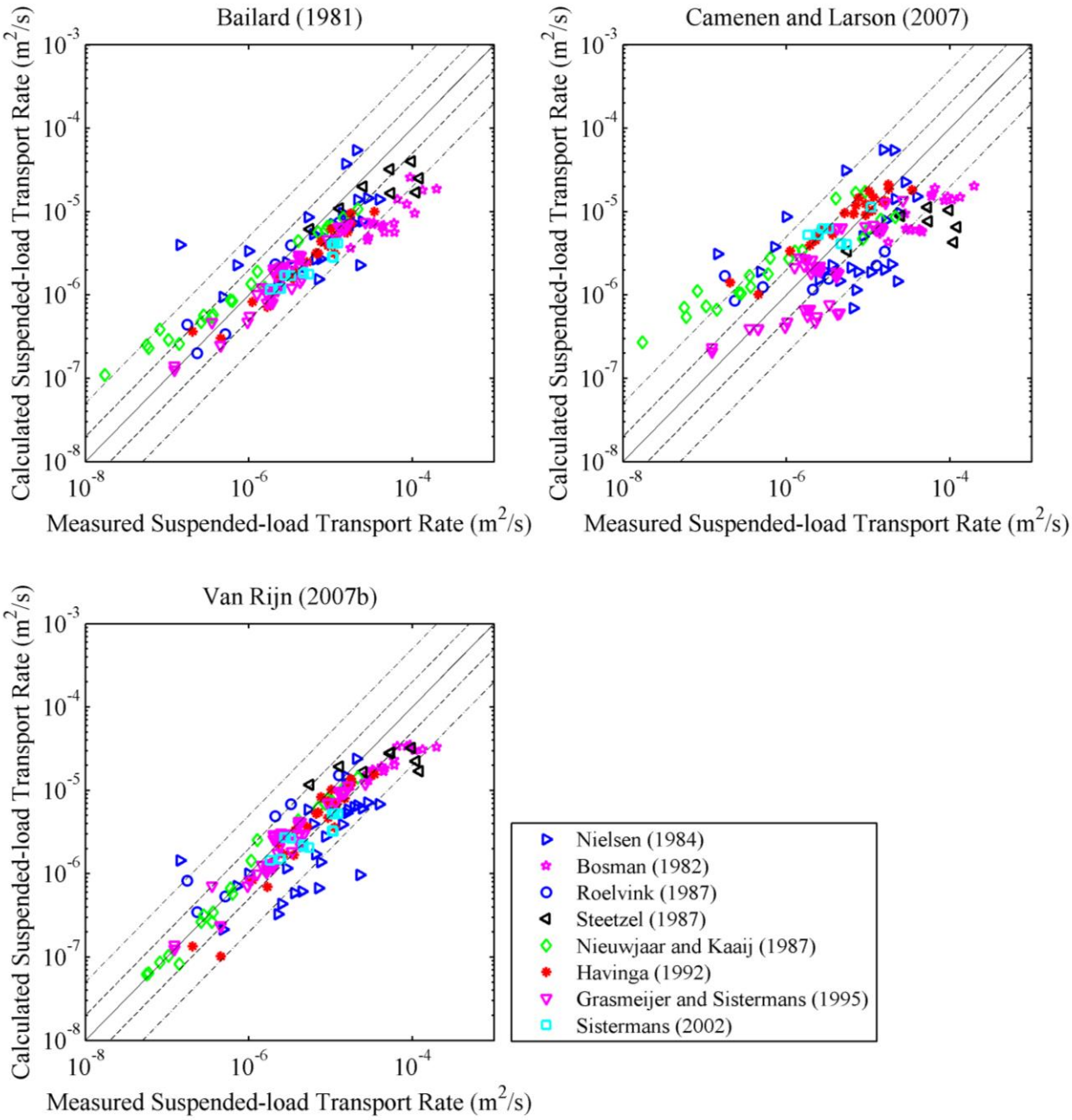

Figure 3.20 Comparison of Predicted and Measured Transport Rates of Uniform Suspended Load under Combined Current and Waves using Different Formulas

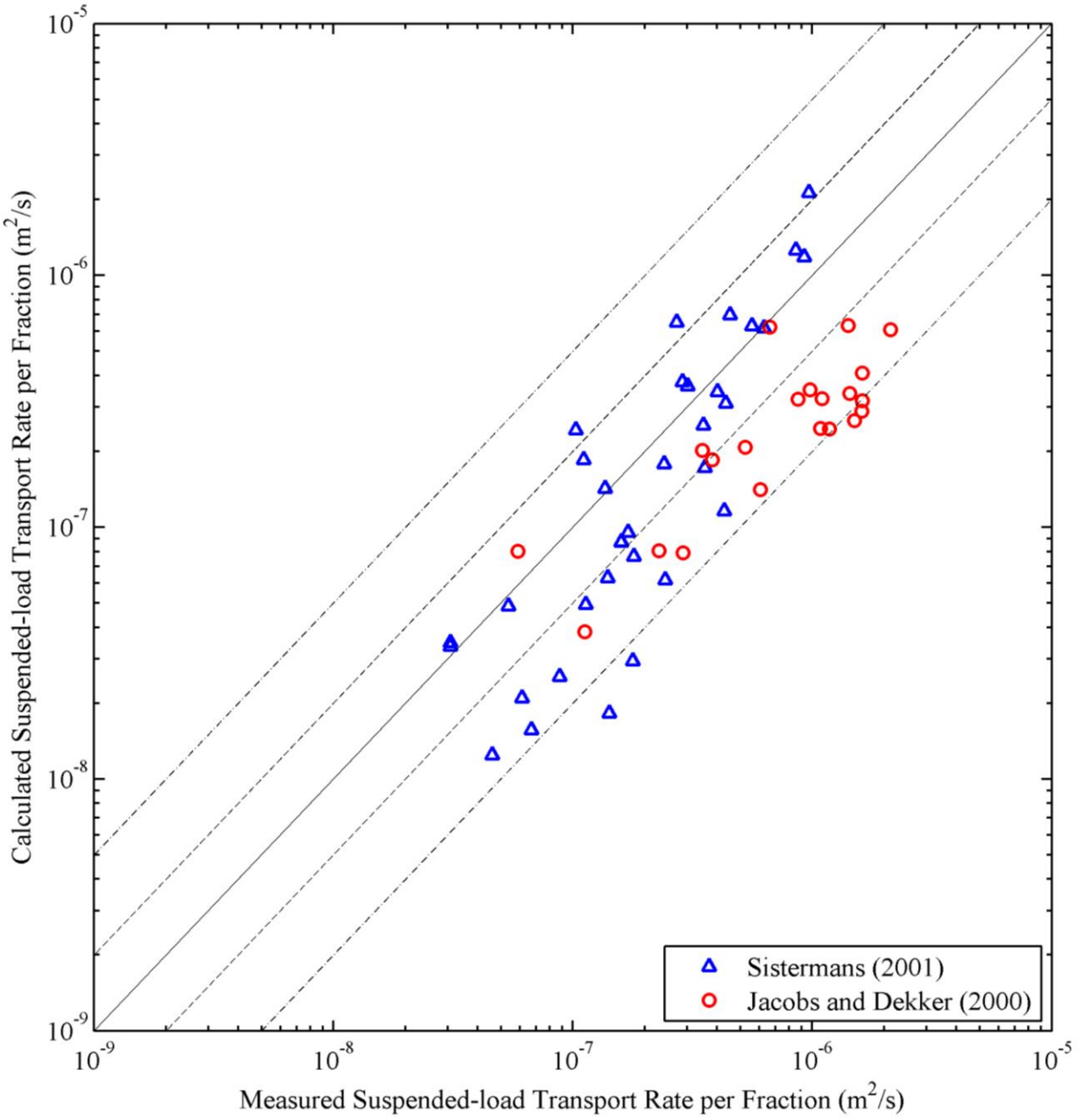

Figure 3.21 Comparison of Predicted and Measured Transport Rates of Nonuniform Suspended Load under Combined Current and Waves using van Rijn (2007c)

Table 3.12 Statistics for Predicted Suspended-load Transport Rates using Different Formulas

Conditions	Formulas	% of Calculated Transport Rates in Error Range				Log(E_{rms})	Log(*bias*)
		0.8-1.25	0.67-1.5	0.5-2.0	0.2-5.0		
Uniform Current+Waves	Bailard (1981)	12.1	23.6	49.7	90.9	0.431	-0.235
	Camenen and Larson (2007)	15.2	24.2	41.2	79.4	0.537	-0.082
	Eq. (3.41) with c_b by van Rijn (2007b)	25.5	46.1	66.1	92.7	0.361	-0.206
	Eq. (3.33)	21.4	40.5	58.9	97.0	0.329	0.068
	Eq. (3.41) with c_b by Eq. (3.40)	24.8	51.5	72.7	93.3	0.386	-0.036
Nonuniform Current+Waves (Fractional Rate)	Eq. (3.41) with c_b by van Rijn (2007c)	15.0	26.7	36.7	83.3	0.473	-0.280
	Eq. (3.33)	20.0	28.3	50.0	85.0	0.435	0.062
	Eq. (3.41) with c_b by Eq. (3.40)	16.7	31.7	46.7	86.7	0.404	0.121

3.2.8 Comparison of Different Methods for Calculating Schmidt Number

In section 3.2.5.3, linear and nonlinear regressions have yielded two fitting curves (Eqs. 3.47 and 3.49) for the relation between $\omega_s/(\kappa U_*)$ and $\sigma_s\omega_s/(\kappa U_*)$ in Fig 3.12. In this section, a unity constant, the two new approaches, and the methods of Einstein and Chien (1954) in Eq. 3.44 and van Rijn (1984b) in Eq. 3.45 are, respectively, applied into the vertical distribution of suspended-load concentration (Eq. 3.43) with the new developed formula for near-bed suspended-load concentration to calculate the suspended-load rate under current only. Same dataset as used for testing the developed near-bed suspended-load concentration is used here.

Table 3.13 shown below indicates different methods have similar results, i.e., the percentages of calculated transport rates in error range are very closed to each other. The approach of Van Rijn (1984b) provides a poor estimation in cases of current only with uniform or nonuniform sediment in comparison with other methods, but it gives a better agreement in the case

of uniform sediment transport under combined current and waves. The values of E_{rms} of the linear and polynomial fitting curves are smaller than those of other approaches in overall. Consequently, the two developed new approaches are good choices to estimate the Schmidt number, while one may assume a Schmidt number of 1.0 in Eq. (3.43) for simplicity.

Table 3.13 Statistics for Predicted Transport Rate by Using Different Methods for Schmidt Number

Conditions	Methods for Schmidt Number	% of Calculated Transport Rates in Error Range				Log(E_{rms})
		0.8-1.25	0.67-1.5	0.5-2.0	0.2-5.0	
Uniform Current only	Constant = 1	40.4	61.2	79.6	95.2	0.352
	Einstein and Chien (1954)	40.9	62.6	79.2	95.1	0.362
	Van Rijn (1984b)	22.9	43.2	70.3	93.9	0.439
	Linear Curve	40.3	61.1	79.6	94.8	0.360
	Polynomial Curve	40.0	61.4	79.5	94.8	0.360
Nonuniform Current only	Constant = 1	15.4	29.5	47.1	85.9	0.514
	Einstein and Chien (1954)	15.2	30.6	47.1	85.3	0.515
	Van Rijn (1984b)	12.5	25.6	43.6	78.8	0.578
	Linear Curve	16.3	27.8	46.9	83.2	0.530
	Polynomial Curve	17.6	29.7	48.2	86.1	0.505

CHAPTER IV

3-D HYDRODYNAMIC MODEL UNDER CURRENT AND WAVES

4.1 Flow Model

4.1.1 3-D Phase-Averaged Shallow Water Flow Equations

The 3-D phase-averaged shallow water flow equations are simplified from the Navier-Stokes equations by assuming hydrostatic pressure. In this study, an implicit 3-D shallow water flow model (Wu, 2014) is adopted, in which only the long wave or current is simulated using a phase-averaged 3-D shallow water flow equations that include the radiation stresses generated by short waves. The short wave characteristics and radiation stresses are determined by a spectral wave model that solves the wave action balance equation. The 3-D shallow water equations in the Cartesian coordinate system are written as

$$\frac{\partial u}{\partial x}+\frac{\partial v}{\partial y}+\frac{\partial w}{\partial z}=0 \tag{4.1}$$

$$\begin{aligned}&\frac{\partial u}{\partial t}+\frac{\partial (uu)}{\partial x}+\frac{\partial (vu)}{\partial y}+\frac{\partial (wu)}{\partial z}=-\frac{1}{\rho}\frac{\partial p_a}{\partial x}-\frac{1}{\rho}\left(\rho_0 g\frac{\partial \eta}{\partial x}+g\int_z^\eta \frac{\partial \rho}{\partial x}dz\right)\\&+\frac{\partial}{\partial x}\left(\nu_{tH}\frac{\partial u}{\partial x}\right)+\frac{\partial}{\partial y}\left(\nu_{tH}\frac{\partial u}{\partial y}\right)+\frac{\partial}{\partial z}\left(\nu_{tV}\frac{\partial u}{\partial z}\right)-\frac{1}{\rho}\frac{\partial S_{xx}}{\partial x}-\frac{1}{\rho}\frac{\partial S_{xy}}{\partial y}+f_c v\end{aligned} \tag{4.2}$$

$$\begin{aligned}&\frac{\partial v}{\partial t}+\frac{\partial (uv)}{\partial x}+\frac{\partial (vv)}{\partial y}+\frac{\partial (wv)}{\partial z}=-\frac{1}{\rho}\frac{\partial p_a}{\partial y}-\frac{1}{\rho}\left(\rho_0 g\frac{\partial \eta}{\partial y}+g\int_z^\eta \frac{\partial \rho}{\partial y}dz\right)\\&+\frac{\partial}{\partial x}\left(\nu_{tH}\frac{\partial v}{\partial x}\right)+\frac{\partial}{\partial y}\left(\nu_{tH}\frac{\partial v}{\partial y}\right)+\frac{\partial}{\partial z}\left(\nu_{tV}\frac{\partial v}{\partial z}\right)-\frac{1}{\rho}\frac{\partial S_{yx}}{\partial x}-\frac{1}{\rho}\frac{\partial S_{yy}}{\partial y}-f_c u\end{aligned} \tag{4.3}$$

where t is the time; x and y are the horizontal coordinates; z is the vertical coordinate pointing upward; u, v, and w are the velocities in x-, y-, and z-directions; η is the water surface elevation above the reference (still) sea level; p_a is the atmospheric pressure; g is the gravitational acceleration; ρ is the density of flow; ρ_0 is the flow density at the water surface; S_{xx}, S_{xy}, S_{yx}, and S_{yy} are wave radiation stress terms; f_c is the Coriolis force coefficient; and ν_{tH} and ν_{tV} are the eddy viscosities in the horizontal and vertical directions.

To obtain the wave radiation stresses, the flow model is coupled with a spectral wave deformation model called CMS-Wave, which solves the spectral wave-action balance equation and provides wave characteristics to the flow model. The spectral wave-action balance equation will be briefly discussed later.

4.1.2 Eddy Viscosity

Even though the developed model can use different eddy viscosities in the vertical and horizontal directions in cases where the vertical and horizontal turbulence structures are significantly different, an isotropic eddy viscosity is used in this study. Considering flows in coastal context are usually large scale in large domains, high-order turbulence closures are usually expensive to use. Therefore, only zero-order turbulence closure models have been implemented in the current version of the developed model, including parabolic eddy viscosity model, subgrid model and mixing length model. Among these options, the mixing length model is found to be applicable for a variety of problems. The classical mixing length model of Prandtl (1925) is usually used for two-dimensional shear flows. For the 3-D shallow water flows, the mixing length model is modified in this study as follows:

$$\nu_t = \sqrt{\left(l_{mV}^2 \left|\bar{S}_V\right|\right)^2 + \left(l_{mH}^2 \left|\bar{S}_H\right|\right)^2} \tag{4.4}$$

where ν_t is the eddy viscosity, l_{mV} is the vertical mixing length, l_{mH} is the horizontal mixing length, $\left|\bar{S}\right|_V = [(\partial u/\partial z)^2 + (\partial v/\partial z)^2]^{1/2}$, and $\left|\bar{S}\right|_H = [2(\partial u/\partial x)^2 + 2(\partial v/\partial y)^2 + (\partial u/\partial y + \partial v/\partial x)^2]^{1/2}$. Eq. (4.4) is a combination of the horizontal and vertical mixing length models and ignores the contribution of vertical velocity that is assumed much smaller than the horizontal velocities in the case of shallow water flow. The vertical and horizontal mixing lengths are determined as

$$l_{mV} = \kappa z\sqrt{1 - z/h} \tag{4.5}$$

$$l_{mH} = \kappa \min(l, c_m h) \tag{4.6}$$

where z is the vertical coordinate above the bed, l is the horizontal distance to the nearest solid wall, h is the total flow depth, κ is the von Karman constant, and c_m is a coefficient which can be calibrated (Wu 2007) and set as about 0.3 in this study.

Eq. (4.5) is the mixing length for vertical two-dimensional open-channel flow proposed by Саткевич (1934). Eq. (4.6) was used by Wu (2007) in a depth-averaged 2-D flow model. Both are modified from Prandtl's mixing length $l_m = \kappa z$ of boundary layer flows. Eq. (4.5) can be applied in the entire depth of open-channel flow, whereas the mixing length of Prandtl is only for the log-law layer near wall boundary. Eq. (4.6) considers the constraint of the horizontal eddy scale by the local flow depth.

In the case of coexisted currents and waves, the horizontal mixing length is determined using Eq. (4.6), and the vertical mixing length is given by

$$l_{mV} = \sqrt{X l_{mc}^2 + (1 - X) l_{mw}^2} \tag{4.7}$$

where l_{mc} is the mixing length due to currents determined with Eq. (4.5); l_{mw} is the mixing length due to waves, set as $a\kappa H$, with a being a coefficient and H the representative wave height; and X is a weighting factor $X = U_c^2 \Big/ \left(U_c^2 + 0.5U_{wm}^2\right)$ in which U_c is the current speed, and U_{wm} is the maximum orbital bottom velocity of wave. The coefficient a will be discussed in the model test section.

4.1.3 Boundary Conditions

For Eqs. (4.1) - (4.3), the flow discharge or velocity is needed at inflow boundaries, while the water level is usually given at outflow boundaries for a subcritical flow or at inflow boundaries for a supercritical flow. At the water surface, the free-surface kinematic condition is applied:

$$\frac{\partial \eta}{\partial t} + u_h \frac{\partial \eta}{\partial x} + v_h \frac{\partial \eta}{\partial y} = w_h \tag{4.8}$$

where u_h, v_h, and w_h are the flow velocities at the water surface.

The surface shear stress due to wind is calculated as

$$\tau_{si} = \rho_a C_D W W_i \tag{4.9}$$

where ρ_a = air density at sea level [~1.2 kg/m^3]; C_D = wind drag coefficient; W_i = wind velocity at 10 m above water level [m/s]; and $W = \sqrt{W_i W_i}$. The drag coefficient is calculated using the formula of Hsu (1988) and modified for high wind speeds based on field data by Powell et al. (2003).

Near rigid wall boundaries, such as beaches and islands, the wall-function approach is employed. By applying the log-law of velocity, the resultant wall shear stress, $\vec{\tau}_w$, is related to the

flow velocity, $\vec{V}_P$, at the center, *P*, of the control volume close to the wall by the following relation:

$$\vec{\tau}_w = -\lambda \vec{V}_P \tag{4.10}$$

where λ is a coefficient determined as $\lambda = \rho u_* \kappa / \ln\left(E y_P^+\right)$ with $y_P^+ = u_* y_P / \nu$, in which y_P is the distance from cell center P to the wall, and *E* is a coefficient related to wall roughness (Wu, 2007). Since λ is related to u_*, iteration is needed to solve Eq. (4.10).

The bed shear stress can be determined using Eq. (4.10) by treating the bed as a solid wall, but the following method is used to take into account the effect of waves on the bed shear stress:

$$\tau_{bx} = \rho c_f u_b \sqrt{u_b^2 + v_b^2 + 0.5 U_{wm}^2}, \quad \tau_{by} = \rho c_f v_b \sqrt{u_b^2 + v_b^2 + 0.5 U_{wm}^2} \tag{4.11}$$

where τ_{bx} and τ_{by} are the bed shear stresses in *x*- and *y*-directions; u_b and v_b are the *x*- and *y*-velocities on the first node above the bed; and c_f is the bed friction coefficient. c_f is treated as a calibrated parameter or determined using the following formula:

$$c_f = \left[\frac{\kappa}{\ln\left(z_P / z_0\right)} \right]^2 \tag{4.12}$$

where κ is the von Karman constant (=0.4); z_P is the elevation of the first node near the bed where u_b and v_b are defined; and z_0 is the bed roughness height coefficient defined as $k_s/30$, in which k_s is the equivalent bed roughness height. k_s is related to the Manning's *n* by Eq. (3.5) if *n* is given.

4.2 Wave Model

4.2.1 Spectral Wave-Action Balance Equation

The spectral wave transformation model, CMS-Wave, is used here to simulate variations of wave-action density in time, space, wave directions, and frequency. CMS-Wave is a spectral wave transformation model and solves the wave-action balance equation using a forward marching finite difference method (Mase et al. 2005; Lin et al. 2008). CMS-Wave includes physical processes such as wave shoaling, refraction, diffraction, reflection, wave-current interaction, wave breaking, wind wave generation, white capping of waves, and the influence of coastal structures. The wave-action balance equation of the wave-action density N is written as

$$\frac{\partial N}{\partial t}+\frac{\partial (c_x N)}{\partial x}+\frac{\partial (c_y N)}{\partial y}+\frac{\partial (c_\theta N)}{\partial \theta}=\frac{\kappa}{2\sigma}\left[\frac{\partial}{\partial y}\left(CC_g\cos^2\theta\frac{\partial N}{\partial y}\right)-\frac{1}{2}CC_g\cos^2\theta\frac{\partial^2 N}{\partial y^2}\right]-\varepsilon_b N+Q \quad (4.13)$$

where $N = N(x,y,\sigma,\theta,t) = E(x,y,\sigma,\theta,t)/\sigma$; E is the spectral wave density representing the wave energy per unit water surface area per frequency interval; σ is the wave angular frequency (or intrinsic frequency); t is the time; x, y are the coordinates in two horizontal directions; θ is wave angle relative to the positive x-direction; C and C_g are the wave celerity and group velocity, respectively; c_x, c_y, and c_θ are the characteristic velocities with respect to x, y and θ, respectively; κ is an empirical coefficient; ε_b is a parameter for wave breaking energy dissipation; and Q includes source/sink terms of wave energy due to wind forcing, bottom friction loss, nonlinear wave-wave interaction, etc.

The first term on the left-hand side of Eq. (4.13) represents the local rate of change of action density in time and is dropped in CMS-Wave which considers a steady wave field at each time interval based on a quasi-steady approach. The second and third terms represent propagation

of wave action density in a horizontal *x*-*y* plane. The fourth term represents depth-induced and current-induced refraction (with propagation velocity c_θ in θ space). The expressions for these propagation speeds are given as

$$\begin{aligned} c_x &= C_g \cos\theta + U \\ c_y &= C_g \sin\theta + V \end{aligned} \tag{4.14}$$

$$c_\theta = \frac{\sigma}{\sinh 2kh}\left(\sin\theta\frac{\partial h}{\partial x} - \cos\theta\frac{\partial h}{\partial y}\right) + \cos\theta\sin\theta\frac{\partial U}{\partial x} - \cos^2\theta\frac{\partial U}{\partial y} + \sin^2\theta\frac{\partial V}{\partial x} - \sin\theta\cos\theta\frac{\partial V}{\partial y} \tag{4.15}$$

where *U*, *V* are the depth-averaged velocities in *x* and *y* directions, *k* is the wave number, and *h* is the water depth.

The first term on the right-hand side of Eq. (4.13), introduced by Mase (2001), represents the energy dissipation due to the diffraction effect in the alongshore *y*-direction, which is implicitly perpendicular to wave direction. Mase (2001) suggested the coefficient κ has a possible value between 2.0–3.0. The second and third terms on the right-hand side represent wave energy loss due to wave breaking and other sources/sinks of wave energy.

4.2.2 Wave Radiation Stress

The wave radiation stresses are calculated using the formula of Mellor (2008):

$$S_{ij} = \int_0^\infty \int_{-\pi}^{\pi} \left\{ k(f)E(f,\theta)\left[\frac{k_i(f)k_j(f)}{k(f)^2}\frac{\cosh^2 k(h+z')}{\sinh kD\cosh kD} - \delta_{ij}\frac{\sinh^2 k(h+z')}{\sinh kD\cosh kD}\right] + \delta_{ij}E_D(f,\theta)\right\} d\theta df \tag{4.16}$$

where *E* is the wave energy, *k* is the wave number, θ is the angle of wave propagation to the onshore direction, *f* is the wave frequency, *h* is the still water depth, *D* is the total water depth, *z'* is

the vertical coordinate referred to the still water level, and E_D is a modified Dirac delta function which is 0 if $z \neq \eta$ and has the following quantity:

$$\int_{-h}^{\eta^+} E_D = E / 2 \tag{4.17}$$

It is noted that the wave-current interactions also include Stokes drift and roller (Walstra et al. 2000; Sheng and Liu, 2011). The present model adopts the roller model implemented in the CMS2D model by Sanchez (2013), which is not described here since it is not used in the model test cases presented in this study. The Stokes drift has different formulations depending on Lagrangian and Eulerian averaging. Based on Eulerian averaging, the Stokes drift is zero below wave trough and nonzero between the wave crest and trough. Because the flow model domain covers only from the phase-averaged water surface to the bed, how to take into account the Stokes drift between the wave crest and phase–averaged water level is still a problem under investigation and does not have a commonly accepted treatment. Because the term E_D in Eq. (4.16), which is the wave energy due to pressure between the wave crest and phase-averaged water surface, can indirectly account for the effect of the corresponding Stokes drift, the Stokes drift is simply lumped into the phase-averaged currents in the present model. This needs to be considered in the interpretation of model results, as demonstrated in test case 4.

4.3 Numerical Solution Methods

The wave-action balance equation (4.13) is solved on a nonuniform Cartesian grid using an implicit finite difference forward marching scheme from seaside boundary to the land side. The details on the numerical methods of the wave model are referred to Mase (2001) and Mase et al. (2005). The following subsections introduce the numerical methods of the flow model and the

coupling between flow and wave models.

4.3.1 Computational Mesh and Data Structure

The present model a multiple-level quadtree rectangular mesh on the horizontal plane for the convenience of local refinement around structures or in high-gradient regions, and the sigma coordinate in the vertical direction to efficiently track the water and bed surface changes. An example of the mesh is shown in Fig. 4.1. For simplifying the mesh, a cell is refined by splitting into four equal child cells on the horizontal plane. Corresponding to this refining, any cell has one or two faces on each of its south, north, west, and east sides. For further simplification, we eliminate those isolated single refined or coarse cells. This means that a cell should be refined if all of its adjacent cells on either x or y direction are refined, and on the other hand, a cell should not be refined if all of its adjacent cells are not refined. Through this handling, each cell has only four to six faces even though its each side may have one or two faces, as shown in Figs. 4.1 and 4.2, so that the computational mesh will be less complicated. Fig. 4.2 shows the connectivity of the mesh on the horizontal plane. The 3-D cell includes a face on each of the top and bottom sides.

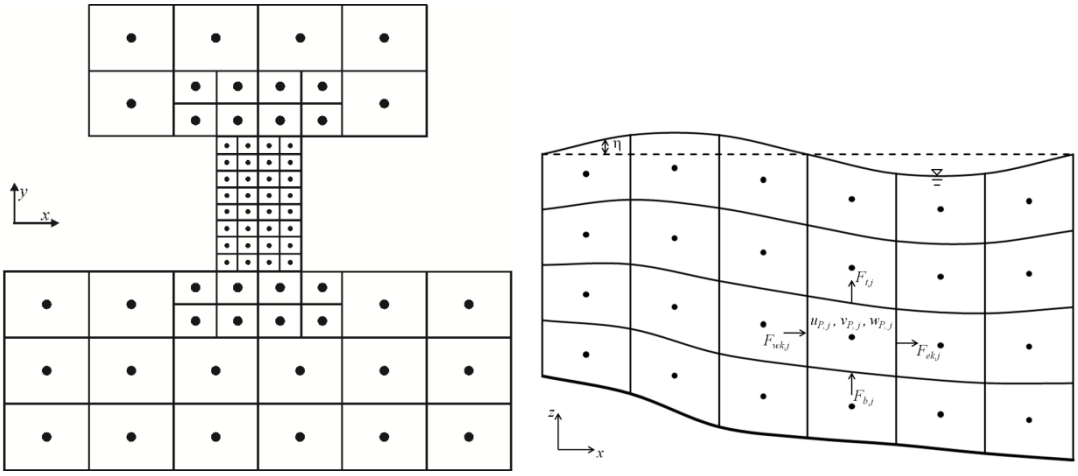

Figure 4.1 Example of the mesh: (left) horizontal quadtree mesh and (right) vertical sigma coordinate

In combination with the vertical sigma coordinate, the nodes on the quadtree mesh at all horizontal layers are numbered in a fully unstructured approach, in which all cells are numbered in a one-dimensional sequence and pointers are used to determine the connectivity of neighboring cells for each cell.

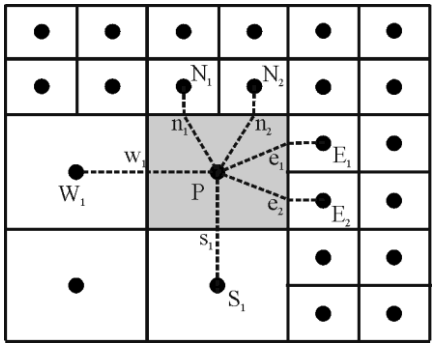

Figure 4.2 Control volume in the horizontal quadtree mesh

One may use staggered or non-staggered approach to arrange the primary variables u, v, w and η. The staggered approach uses a different grid system for each of these variables, while the non-staggered grid uses only one grid system for all of them. Considering the staggered approach is more complicated than the non-staggered approach near the interface between coarse and fine meshes, as shown in Fig. 4.2, the non-staggered grid is used in this study. All the primary variables are arranged at cell centers, and the fluxes are stored at cell faces.

4.3.2 Discretization of 3-D Phase-Averaged Shallow Water Flow Equations

Integrating the continuity equation (4.1) over the 3-D control volume (whose side view is shown in Figs. 4.2), applying Green's theorem and discretizing the temporal derivative by the backward difference scheme, one can derive the following equation:

$$\frac{\Delta V_{P,j}^{n+1} - \Delta V_{P,j}^{n}}{\Delta t} + \sum_{k=1}^{m_e} F_{ek,j} - \sum_{k=1}^{m_w} F_{wk,j} + \sum_{k=1}^{m_n} F_{nk,j} - \sum_{k=1}^{m_s} F_{sk,j} + F_{t,j} - F_{b,j} = 0 \tag{4.18}$$

where Δt is the time step length; $\Delta V_{p,j}$ is the volume of the control volume (cell) at node P with vertical cell index j; the superscript n denotes time level; F denotes the convective fluxes across cell faces; the subscripts w, e, s, n, b and t denote the west (negative x), east (positive x), south (negative y), north (positive y), bottom (negative z) and top (positive z) sides of the control volume; the subscript k is the index of the horizontal faces, with a value of 1 or 2; and m_w, m_e, m_s and m_n are the numbers of cell faces at west, east, south and north sides of the cell. For the control volume shown in Fig. 4.2, m_w=1, m_e=2, m_s=1 and m_n=2. For simplicity, m_w, m_e, m_s, m_n, and the superscript n+1 will be omitted in the following notations.

The convective fluxes at cell faces are defined as

$$
\begin{aligned}
F_{wk,j} &= u_{wk,j}\Delta A_{wk,j}, \quad F_{ek,j} = u_{ek,j}\Delta A_{ek,j} \\
F_{sk,j} &= v_{sk,j}\Delta A_{sk,j}, \quad F_{nk,j} = v_{nk,j}\Delta A_{nk,j} \\
F_{b,j} &= \tilde{w}_{b,j}\Delta A_{b,j}, \qquad F_{t,j} = \tilde{w}_{t,j}\Delta A_{t,j}
\end{aligned}
\tag{4.19}
$$

where ΔA denotes the areas of cell faces, and $\tilde{w}$ denotes the velocity normal to the bottom and top faces of the cell. $\tilde{w}$ is related to the vertical velocity w as well as the horizontal velocities.

Eq. (4.18) is rearranged as

$$
F_{t,j} = F_{b,j} - \frac{\Delta V_{P,j}^{n+1} - \Delta V_{P,j}^{n}}{\Delta t} - \left(\sum_k F_{ek,j} - \sum_k F_{wk,j} + \sum_k F_{nk,j} - \sum_k F_{sk,j} \right) \tag{4.20}
$$

Because the vertical flux at the bed is zero, Eq. (4.20) is used to determine the vertical flux and in turn the vertical velocity at the top face of each cell by sweeping from the bed to water surface in each vertical line.

Integration of the momentum equations (4.2) and (4.3) over the 3-D control volume and discretization of the temporal derivative using the backward difference scheme, the convective terms using an upwinding scheme and the diffusion terms using the central difference scheme leads to

$$
u_{P,j}^{n+1} = \frac{1}{a_{P,j}^{u}} \left(\sum_l a_{l,j}^{u} u_{l,j}^{n+1} + S_u \right) - \sum_k D_{ek,j}^{1} \eta_{ek} + \sum_k D_{wk,j}^{1} \eta_{wk} \tag{4.21}
$$

$$
v_{P,j}^{n+1} = \frac{1}{a_{P,j}^{v}} \left(\sum_l a_{l,j}^{v} v_{l,j}^{n+1} + S_v \right) - \sum_k D_{nk,j}^{2} \eta_{nk} + \sum_k D_{sk,j}^{2} \eta_{sk} \tag{4.22}
$$

where a^u and a^v denote the coefficients for the discretized u and v momentum equations, $D_{wk,j}^{1} = g\Delta A_{wk,j} / a_{P.j}^{u}$, $D_{ek,j}^{1} = g\Delta A_{ek,j} / a_{P,j}^{u}$, $D_{sk,j}^{2} = g\Delta A_{sk,j} / a_{P,j}^{v}$, $D_{nk,j}^{2} = g\Delta A_{nk,j} / a_{P,j}^{v}$, and S_u, S_v include the source terms and the variables at time level n generated from discretization of the temporal derivative terms. Note that the first summation in Eqs. (4.21) and (4.22) is applied with

the index, *l*, sweeping over all the neighboring cells of cell P. The convection terms can be discretized using several numerical schemes with upwinding capability, such as the hybrid upwind/central scheme (Spalding, 1972), exponential scheme (Spalding, 1972) and HLPA scheme (Zhu, 1991). The HLPA scheme is approximately second-order accurate, while the hybrid and exponential schemes have accuracy between first and second orders. Details of these schemes can be found in Wu (2007).

4.3.3 Solution of Discretized Equations

The SIMPLEC algorithm is used in this study to couple the flow velocity and water level. Eq. (4.21) is used to compute the *u* velocity for an assumed water level field in an iterative manner. Application of under-relaxation (Majumdar, 1988) leads to

$$u_{P,j}^{*} = \alpha_u \left(H_{1P,j}^{*} - \sum_k D_{ek,j}^{1} \eta_{ek}^{*} + \sum_k D_{wk,j}^{1} \eta_{wk}^{*} \right) + (1-\alpha_u) u_{P,j}^{o} \tag{4.23}$$

where η^{*} is the guessed water level, $u_{P,j}^{*}$ is the approximate solution of *u*-velocity, $u_{P,j}^{o}$ is the *u*-velocity in the previous iteration step, $H_{1P,j}^{*}$ denotes the first term on the right-hand side of Eq. (4.21) and α_u is the relaxation factor that is set as about 0.8 in this study.

One can derive the relation between the water level and velocity corrections from Eq. (4.23):

$$u_{P,j}^{n+1} = u_{P,j}^{*} + \alpha_u \left(\sum_k \tilde{D}_{wk,j}^{1} \eta'_{wk} - \sum_k \tilde{D}_{ek,j}^{1} \eta'_{ek} \right) \tag{4.24}$$

where η' is the water level correction $\eta' = \eta - \eta^*$. In the SIMPLEC algorithm, $\tilde{D}^1_{wk,j} = D^1_{wk,j} \Big/ \left(1 - \alpha_u \sum_l a^u_{l,j} \Big/ a^u_{P,j}\right)$ and $\tilde{D}^1_{ek,j} = D^1_{ek,j} \Big/ \left(1 - \alpha_u \sum_l a^u_{l,j} \Big/ a^u_{P.j}\right)$. The relation of water level and velocity corrections for the SIMPLE algorithm is similar to Equation (4.24), with $\tilde{D}^1_{wk,j}$ and $\tilde{D}^1_{ek,j}$ replaced by $D^1_{wk,j}$ and $D^1_{ek,j}$.

Similarly, one can have the *v*-equation and the corresponding correction equation:

$$v^*_{P,j} = \alpha_v \left(H^*_{2P,j} - \sum_k D^2_{nk,j} \eta^*_{nk} + \sum_k D^2_{sk,j} \eta^*_{sk} \right) + (1 - \alpha_v) v^o_{P,j} \tag{4.25}$$

$$v^{n+1}_{P,j} = v^*_{P,j} + \alpha_v \left(\sum_k \tilde{D}^2_{sk,j} \eta'_{sk} - \sum_k \tilde{D}^2_{nk,j} \eta'_{nk} \right) \tag{4.26}$$

where $H^*_{2P,j}$ denotes the first term on the right-hand side of Eq. (4.22), $\tilde{D}^2_{sk,j} = D^2_{sk,j} \Big/ \left(1 - \alpha_v \sum_l a^v_{l,j} \Big/ a^v_{P,j}\right)$ and $\tilde{D}^2_{nk,j} = D^2_{nk,j} \Big/ \left(1 - \alpha_v \sum_l a^v_{l,j} \Big/ a^v_{P,j}\right)$. Here, α_v is the relaxation factor for the *v*-equation.

In order to avoid the checkerboard splitting for the collocated arrangement (Patankar, 1980), the momentum interpolation technique proposed by Rhie and Chow (1983) is adopted to evaluate the variable values at cell faces from the quantities at cell centers. For example, the *u*-velocity at w-face and the *v*-velocity at s-face are determined as

$$\begin{aligned} u^*_{wk,j} = {} & \alpha_u \left[\left(1 - f_{x,p}\right) H^*_{1PWk,j} + f_{x,p} H^*_{1P,j} \right] + \alpha_u \left[\left(1 - f_{x,p}\right) / a^u_{PWk,j} + f_{x,p} / a^u_{P,j} \right] g \Delta A_{wk,j} \left(\eta^*_{Wk} - \eta^*_P \right) \\ & + (1 - \alpha_u) \left[\left(1 - f_{x,p}\right) u^o_{Wk,j} + f_{x,p} u^o_{P,j} \right] \end{aligned} \tag{4.27}$$

$$\begin{aligned} v^*_{sk,j} = {} & \alpha_v \left[\left(1 - f_{y,p}\right) H^*_{2PSk,j} + f_{y,p} H^*_{2P,j} \right] + \alpha_v \left[\left(1 - f_{y,p}\right) / a^v_{PSk,j} + f_{y,p} / a^v_{P,j} \right] g \Delta A_{sk,j} \left(\eta^*_{Sk} - \eta^*_P \right) \\ & + (1 - \alpha_v) \left[\left(1 - f_{y,p}\right) v^o_{Sk,j} + f_{y,p} v^o_{P,j} \right] \end{aligned} \tag{4.28}$$

in which $f_{x,p}$ and $f_{y,p}$ are the weighting factors used to interpolate the values of a variable at cell faces w and s from the values at two adjoining cell centers P and W or P and S, respectively; $H^*_{1PWk,j}$ and $H^*_{2PSk,j}$ stand for $H^*_{1P,j}$ and $H^*_{2P,j}$ when applying Eqs. (4.23) and (4.25) on the cells centered by W and S, respectively. The velocity corrections corresponding to Eqs. (4.27) and (4.28) for the SIMPLEC algorithm are derived as

$$u^{n+1}_{wk,j} = u^*_{wk,j} + \alpha_u \tilde{Q}^1_{wk,j}\left(\eta'_{Wk} - \eta'_P\right) \tag{4.29}$$

$$v^{n+1}_{sk,j} = v^*_{sk,j} + \alpha_v \tilde{Q}^2_{sk,j}\left(\eta'_{Sk} - \eta'_P\right) \tag{4.30}$$

where $\tilde{Q}^1_{wk,j} = \left[\left(1-f_{x,p}\right)/a^u_{PWk,j} + f_{x,p}/a^u_{P,j}\right] g\Delta A_{wk,j} \Big/ \left[1-\alpha_u\left(1-f_{x,p}\right)\left(\sum_l a^u_l/a^u_P\right)_{PWk,j} - \alpha_u f_{x,p}\left(\sum_l a^u_l/a^u_P\right)_{P,j}\right]$

$\tilde{Q}^2_{sk,j} = \left[\left(1-f_{y,p}\right)/a^v_{PSk,j} + f_{y,p}/a^v_{P,j}\right] g\Delta A_{sk,j} \Big/ \left[1-\alpha_v\left(1-f_{y,p}\right)\left(\sum_l a^v_l/a^v_P\right)_{PSk,j} - \alpha_v f_{y,p}\left(\sum_l a^v_l/a^v_P\right)_{P,j}\right]$

With the definition of fluxes at cell faces and Eqs. (4.29) and (4.30), one can derive the flux corrections at w and s faces:

$$F_{wk,j} = F^*_{wk,j} + a^\eta_{Wk,j}\left(\eta'_{Wk} - \eta'_P\right) \tag{4.31}$$

$$F_{sk,j} = F^*_{sk,j} + a^\eta_{Sk,j}\left(\eta'_{Sk} - \eta'_P\right) \tag{4.32}$$

where $a^\eta_{Wk,j} = \alpha_u \tilde{Q}^1_{wk,j}\Delta A_{wk,j}$, $a^\eta_{Sk,j} = \alpha_v \tilde{Q}^2_{sk,j}\Delta A_{sk,j}$, and $F^*_{wk,j}$ and $F^*_{sk,j}$ are the fluxes at faces w and s in terms of the velocities $u^*_{wk,j}$ and $v^*_{sk,j}$ evaluated using Eqs. (4.28) and (4.29).

Summation of Eq. (4.20) over each vertical line and application of the free-surface kinematic condition (4.8) leads to the depth-integrated continuity equation:

$$\frac{\eta^{n+1}_P - \eta^n_P}{\Delta t}\Delta A_P + \sum_k\sum_{j=1}^{J} F_{ek,j} - \sum_k\sum_{j=1}^{J} F_{wk,j} + \sum_k\sum_{j=1}^{J} F_{nk,j} - \sum_k\sum_{j=1}^{J} F_{sk,j} = 0 \tag{4.33}$$

where J is the number of cells at the vertical line, and ΔA_P is the area of the cell projected onto the horizontal plane.

Inserting Eqs. (4.31) and (4.32) into (4.33) leads to the following equation for water level correction:

$$a_P^{\eta}\eta'_P = \sum_k a_{Wk}^{\eta}\eta'_{Wk} + \sum_k a_{Ek}^{\eta}\eta'_{Ek} + \sum_k a_{Sk}^{\eta}\eta'_{Sk} + \sum_k a_{Nk}^{\eta}\eta'_{Nk} + S_{\eta} \tag{4.34}$$

where $a_{Wk}^{\eta} = \sum_{j=1}^{J} a_{Wk,j}^{\eta}$, $a_{Ek}^{\eta} = \sum_{j=1}^{J} a_{Ek,j}^{\eta}$, $a_{Sk}^{\eta} = \sum_{j=1}^{J} a_{Sk,j}^{\eta}$, $a_{Nk}^{\eta} = \sum_{j=1}^{J} a_{Nk,j}^{\eta}$, $a_P^{\eta} = \sum_l a_l^{\eta} + \frac{\Delta A_P}{\Delta t}$, and

$$S_{\eta} = -\frac{\eta_P^* - \eta_P^n}{\Delta t}\Delta A_P - \left(\sum_k \sum_{j=1}^{J} F_{ek,j}^* - \sum_k \sum_{j=1}^{J} F_{wk,j}^* + \sum_k \sum_{j=1}^{J} F_{nk,j}^* - \sum_k \sum_{j=1}^{J} F_{sk,j}^* \right).$$

The set of non-linear discretized equations are solved iteratively. The iteration process consists of inner and outer iteration loops. The inner iteration is designed for iteratively solving each of the discretized momentum equations (4.21) and (4.22) and the water-level-correction equation (4.34). The outer iteration loop visits the discretized equations in the following sequence in each time step as required by the SIMPLEC algorithm:

a) Guess the water level field η^*;

b) Solve the momentum equations (4.23) and (4.25) to obtain $u_{P,j}^*$ and $v_{P,j}^*$;

c) Use the Rhie and Chow's momentum interpolation to determine the horizontal velocities and fluxes at cell faces;

d) Calculate η' using Eq. (4.34);

e) Correct η by $\eta = \eta^* + \eta'$, and update $u_{P,j}$ and $v_{P,j}$ using Eqs. (4.24) and (4.26) and horizontal fluxes using Eqs. (4.31) and (4.32);

f) Determine the vertical fluxes at top and bottom faces using the discretized continuity equation (4.20) by sweeping from the bottom to the water surface along each vertical line, and then the vertical velocity $w_{P,j}$ at cell centers using the derived vertical fluxes;

g) Treat the corrected water level, η, as a new guess η^*, and repeat the procedure from steps 2 to 6 until a converged solution is obtained.

4.3.4 Weting and Drying Techniques

It is of importance to handling the wetting and drying processes in surface water flow simulation. The present model uses a threshold flow depth (a small value such as 0.01 m in experimental cases and 0.05 m in field cases) to judge drying and wetting. If the flow depth at a vertical line is larger than the threshold value, the vertical line is considered to be wet; otherwise, the vertical line is dry. For the convenience of solution algorithm, each dry vertical line is represented by the same number of nodes as the neighboring wet vertical line. Because a fully implicit solver is used in the present model, all the wet and dry nodes participate in the solution. The nodes on all dry vertical lines are assigned a zero velocity. On the water edges between the dry and wet nodes, the wall-function approach is applied (Wu 2014).

4.3.5 Coupling of Flow and Wave Models

The flow and wave models are coupled together using a process called steering. The time interval at which the wave model is run is called the steering interval or wave time step. The steering process is summarized below:

a) The wave model is run first using the initial water level, current velocity, and bed elevation;
b) Wave information such as wave height, period, dissipation, radiation stress gradient, and wave unit vector are interpolated spatially from the wave grid to the flow grid and passed to the flow model;
c) The flow model is run until the next steering interval using wave characteristics that are linearly interpolated throughout time during the specified steering interval. At each flow time step, variables such as wave length and bottom orbital velocities are updated using the new water depth and current velocity;
d) Water level, current velocity, and bed elevation are interpolated from the flow grid to the wave grid and passed to the wave model;
e) The wave model is then run again for the following wave time step;
f) Steps b) - e) are repeated until the end of the simulation.

4.4 Model Testing

The developed model was tested by four cases. The first two cases are tidal flows in estuaries, through which the stability, efficiency and reliability of the model for unsteady flows are quantitatively validated. The third case is wind-induced current case, which shows the validity of mixing length model in simulating the wind-induced velocity profile. The fourth case is undertow current due to waves on a sloping beach, which validates the coupling of the wave and flow models.

4.4.1 Tidal Flow in San Francisco Bay

San Francisco Bay is the largest estuary on the west coast of the U.S.A. It includes four bays: Suisun Bay, San Pablo Bay, Central Bay and South Bay, as shown in Fig. 4.3. The simulation domain includes the full bay and the open sea. Because the domain is very irregular, the used mesh consists of 72081 quadtree rectangular cells on the horizontal plane and 6 layers in the vertical direction. Fig. 4.4 shows the computational mesh, with dots representing locations of cell centers. The coarsest cell size is 3200×3200 m near the offshore ocean boundary, and the finest cell size is 25×25 m near the southern shoreline of Pacific coast. The bathymetry data covering the full bay area was downloaded from USGS's San Francisco Bay Bathymetry Web Site (http://sfbay.wr.usgs.gov/sediment/sfbay/index.html). The measured tidal levels are used at the offshore boundary. The simulation period is 120 hours long in April 25–30, 2003. The simulation starts from a static condition (zero flow velocity), but with a two-day ramp period to get reasonable initial tidal flow field. The Coriolis coefficient is 0.000089. The bed friction coefficient c_f is set as 0.002. The computational time step is 15 minutes.

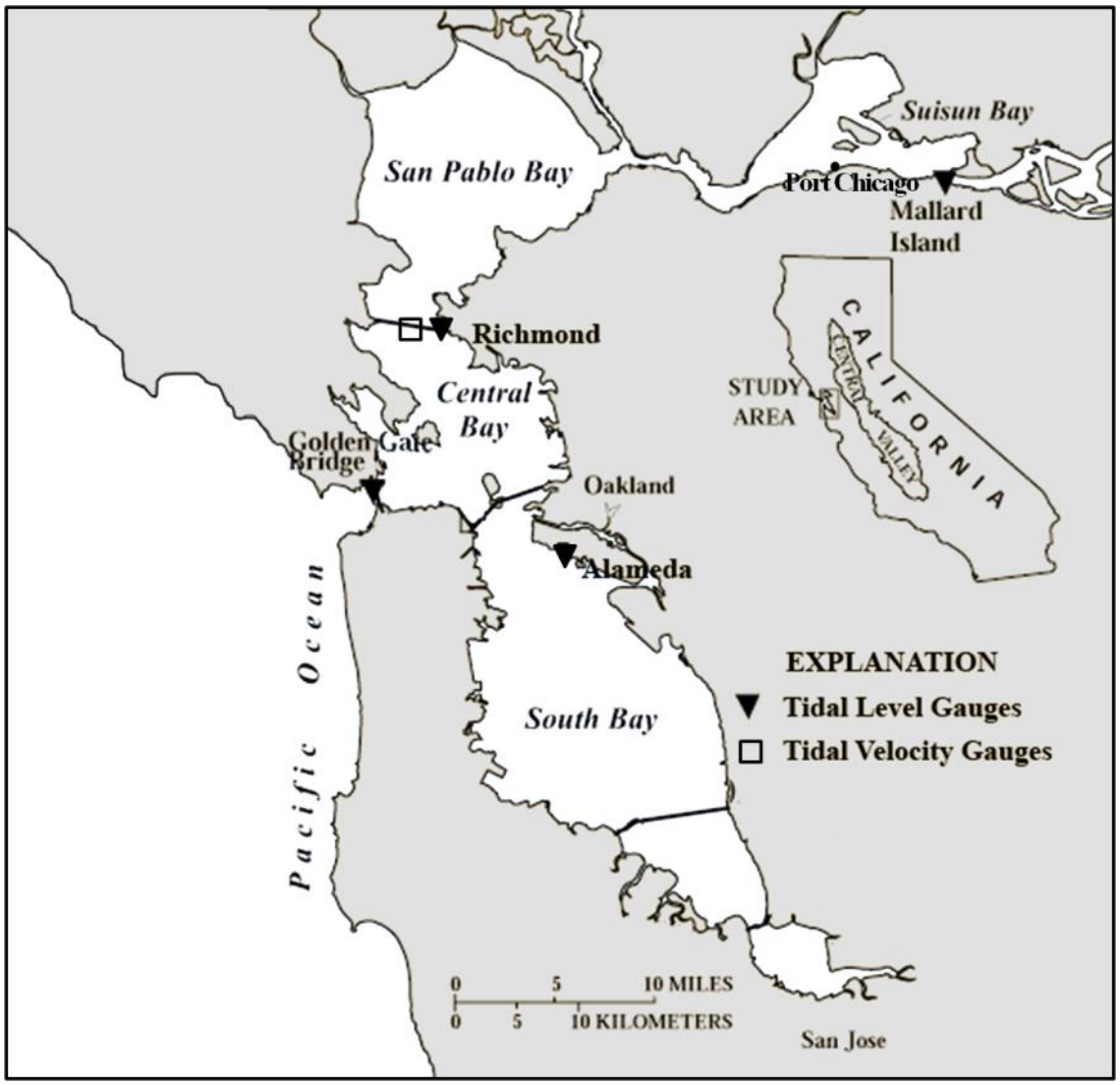

Figure 4.3 Computational domain and measurement stations in San Francisco Bay, CA

Figs. 4.5 and 4.6 show the computed flow patterns near the Golden Gate Bridge and Port Chicago in flood and ebb tides. One can see that the wetting and drying processes on the flood plain are handled well. Fig. 4.7 compares the measured and simulated water levels at four stations: Alameda, Golden Gate Bridge, Richmond, and Mallard Island. The amplitudes and phases of the

tidal levels are well predicted. There is no significant phase difference between the measurement and simulation. Fig. 4.8 compares the measured and simulated flow velocities at the upper, middle and bottom layers of water in station Richmond. The general trend of the temporal variation of velocity is reasonably well obtained.

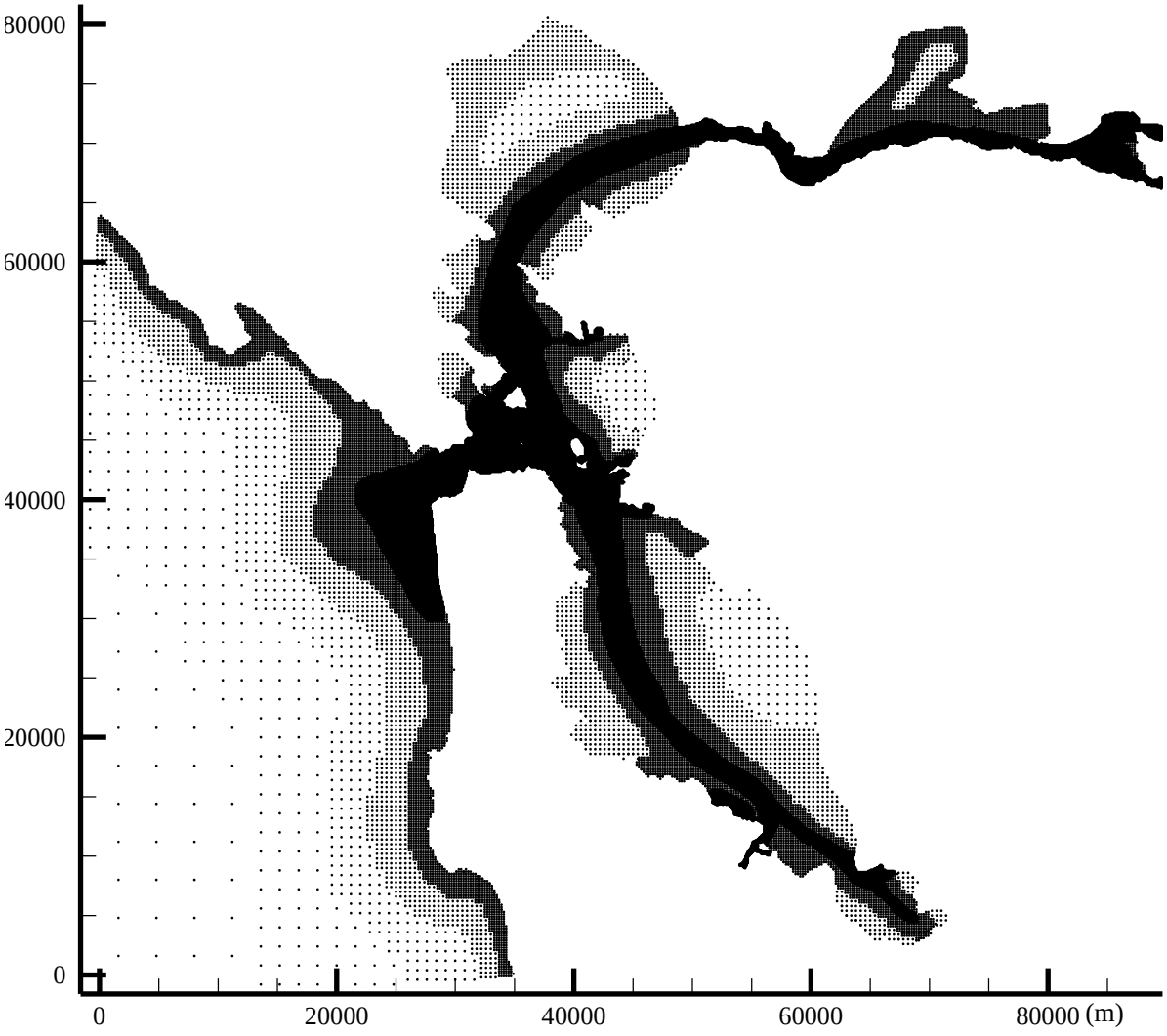

Figure 4.4 Computational mesh for San Francisco Bay (dots: cell centers)

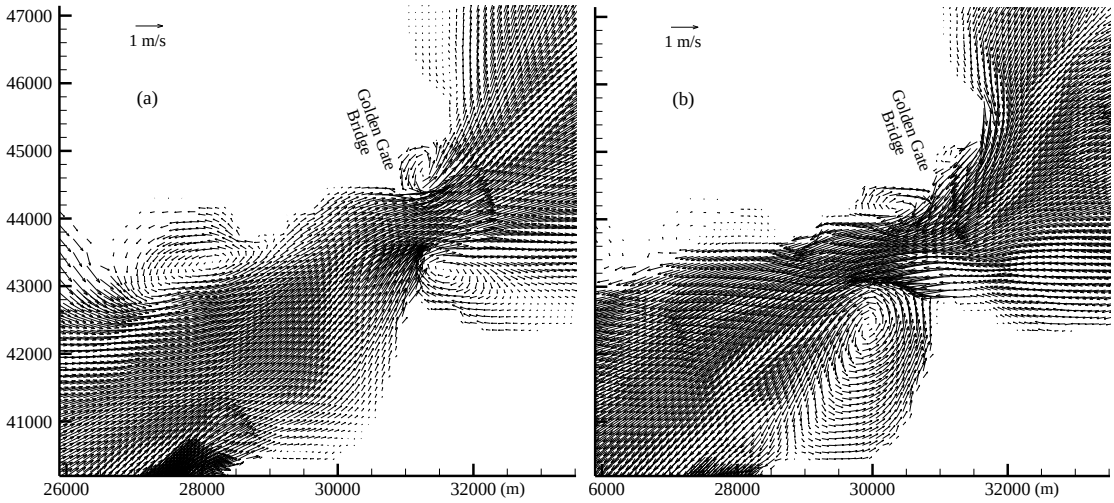

Figure 4.5 Computed depth-average flow patterns near Golden Gate Bridge: (a) flood tide and (b) ebb tide

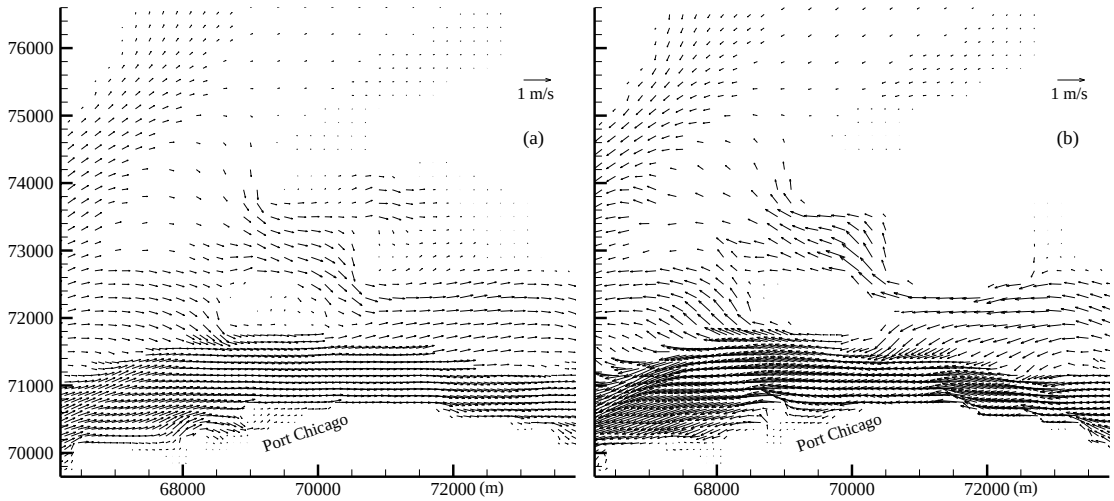

Figure 4.6 Computed depth-average flow patterns near Port Chicago: (a) flood tide and (b) ebb tide

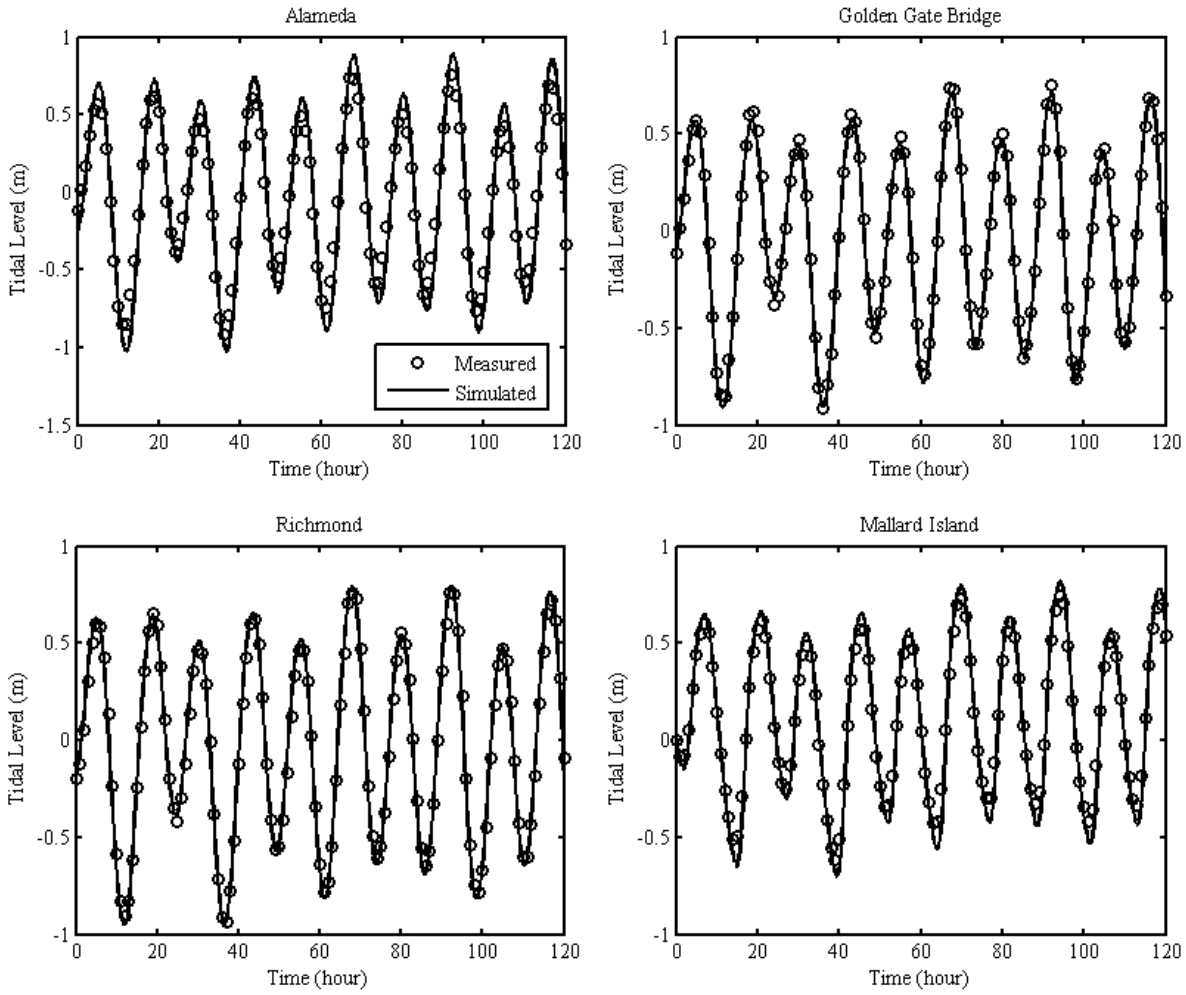

Figure 4.7 Measured and simulated tide levels in San Francisco Bay

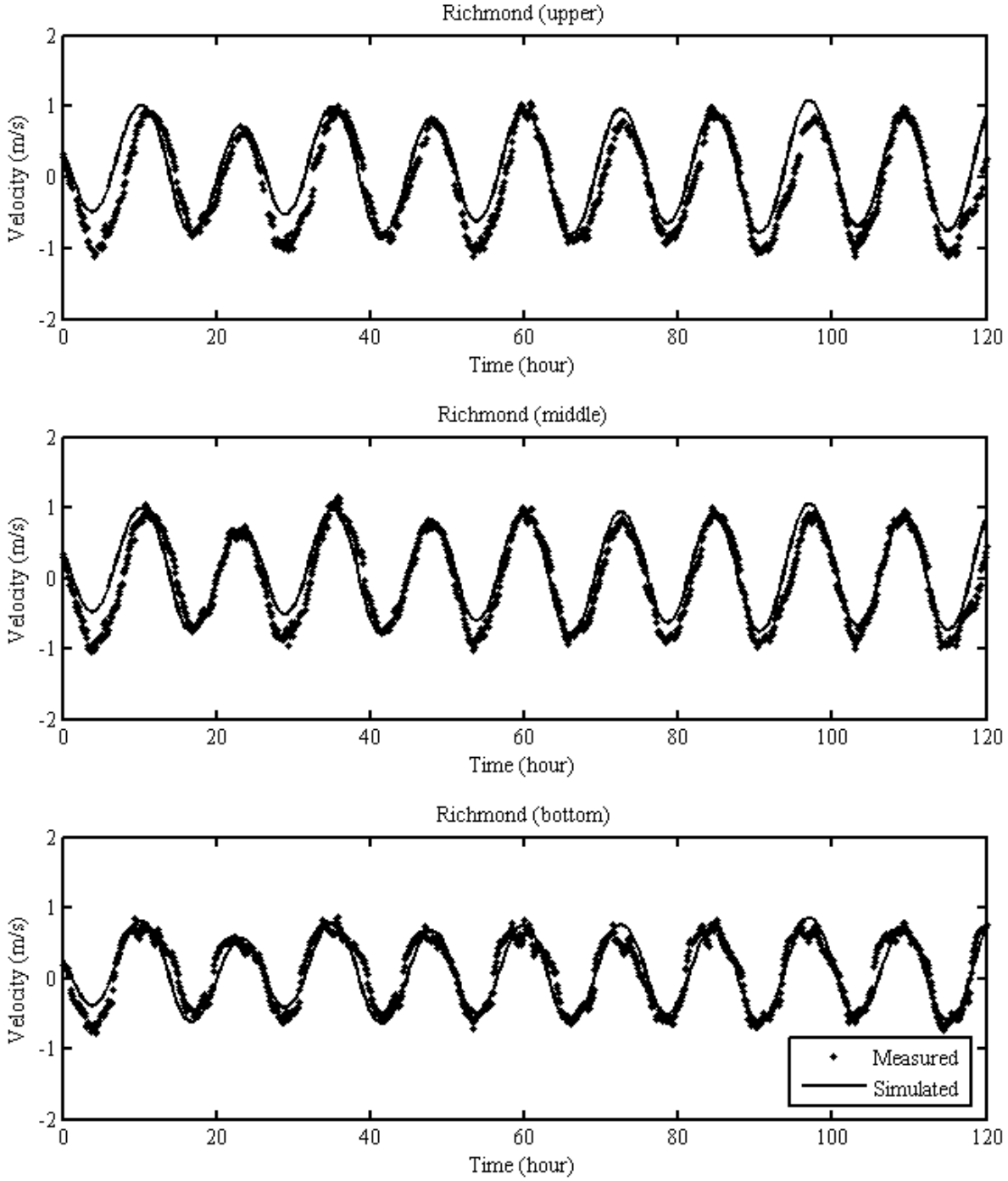

Figure 4.8 Measured and simulated velocities at station Richmond, San Francisco Bay

4.4.2 Tidal Flow in Gironde Estuary

The Gironde Estuary, located in southwestern France, is the passage of the Garonne River and the Dordogne River into the Atlantic Ocean, as shown in Fig. 4.9. The water body is about 2–14 km wide, and the navigation channel is about 6–30 m deep. The estuary is partially mixed and macrotidal, with a 12 hour and 25 minutes tidal lunar period and a tidal amplitude of 1.5–5 m at the mouth (Li et al., 1994). The simulation domain is about 80 km long, starting from the mouth to the Garonne River and the Dordogne River. The horizontal domain is represented by a uniform mesh with a size of 250 m × 125 m for each cell, and each vertical line is divided to 6 layers. The data measured from May 19–25, 1975 is used to validate the developed model. The computational time step is 15 minutes. At the estuary mouth, the tidal elevation is given by the recorded time series at station "Pointe de Grave". At the two upstream ends, the flow discharges of the Garonne River and the Dordogne River are specified according to the measured data at La Réole and Pessac. The bed friction coefficient c_f is estimated as 0.002.

Fig. 4.10 compares the measured and simulated water levels at stations Richard and Ile Verte. The amplitude and phase are well predicted by the numerical model. No obvious phase difference exists between the measured and simulated tidal levels. Fig. 4.11 shows the comparison of the measured and simulated flow velocities at 1 m under the water surface and 1 m above the bed in stations Blaye and PK68. The agreement is reasonably good.

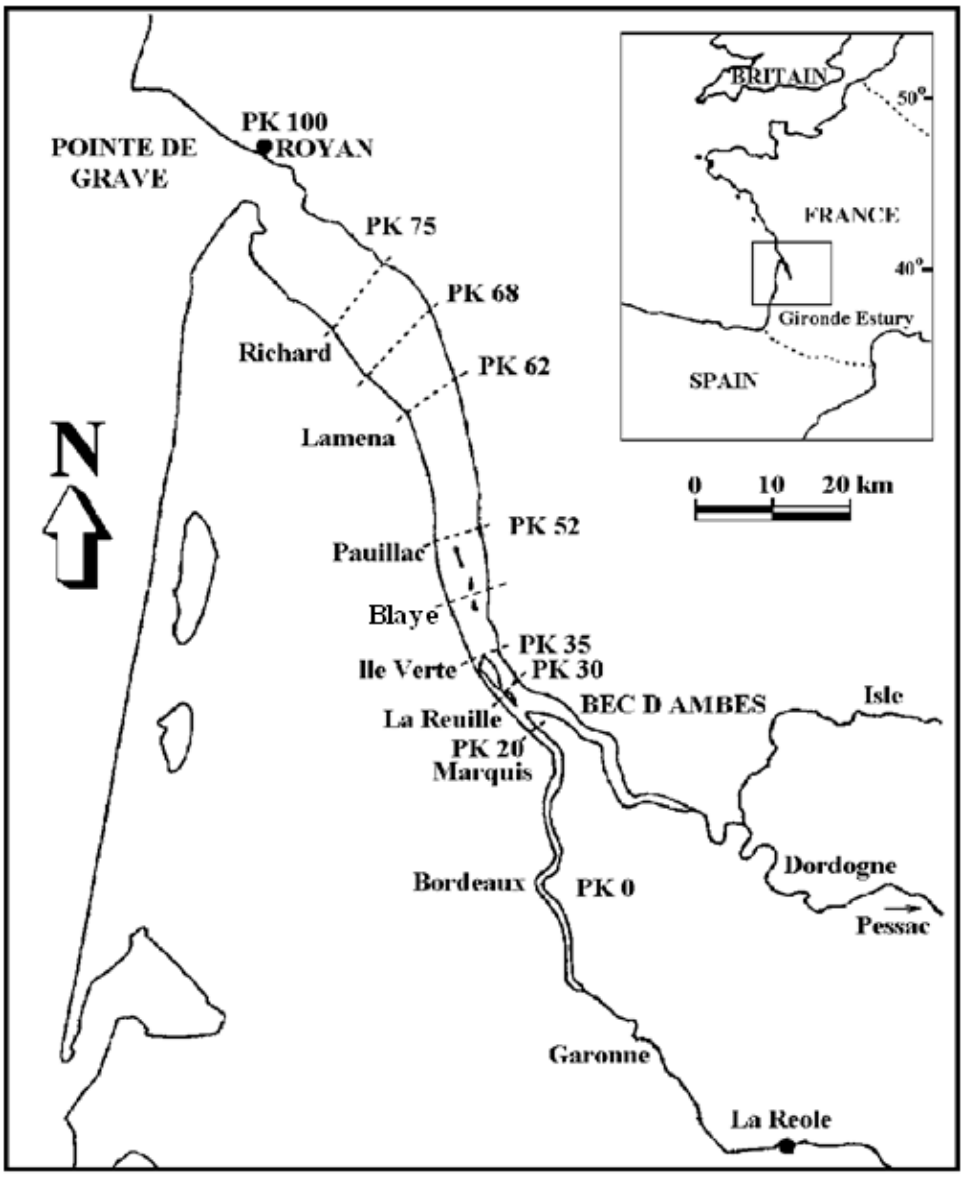

Figure 4.9 Sketch of Gironde Estuary, France

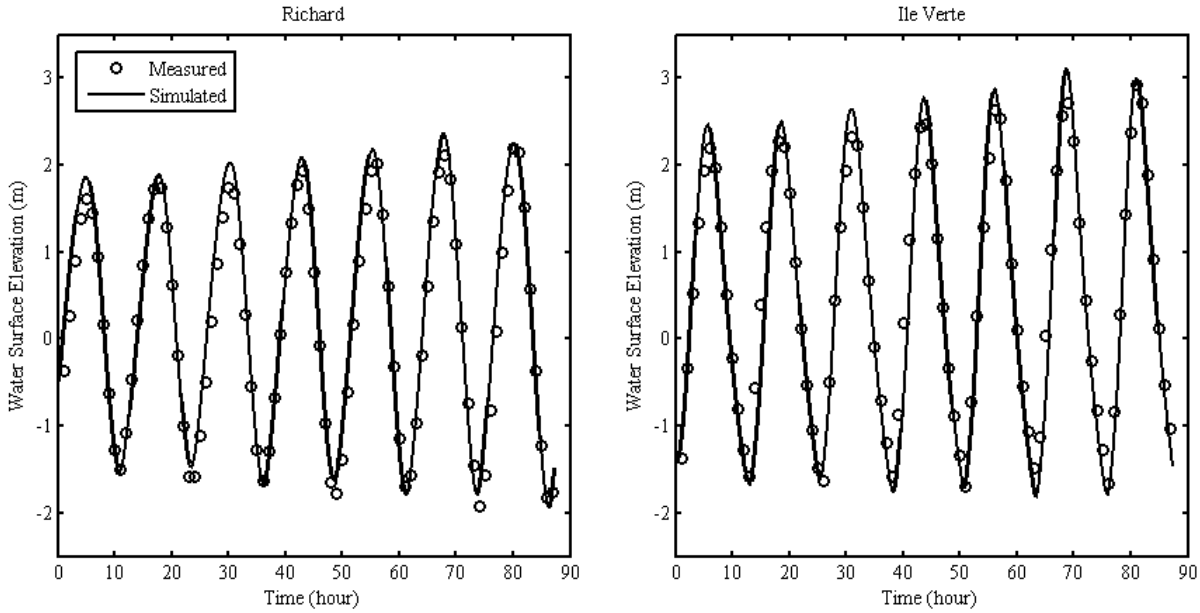

Figure 4.10 Measured and calculated water levels at selected stations in Gironde Estuary

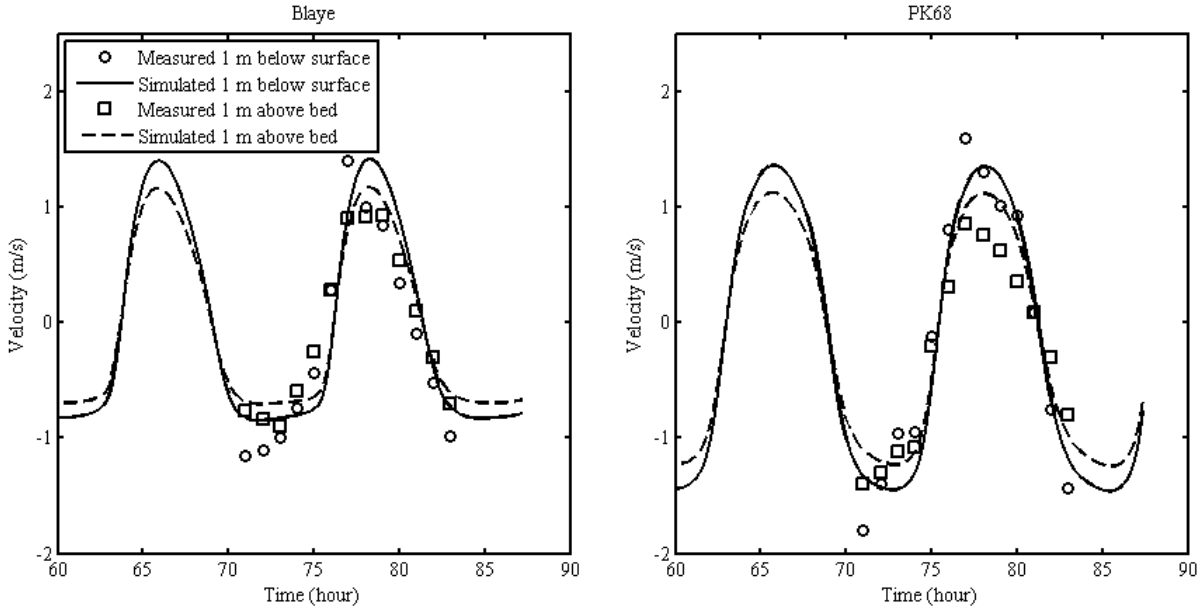

Figure 4.11 Measured and calculated flow velocities at selected stations in Gironde Estuary

4.4.3 Wind-induced Current in a Flume

The developed model is tested using the experiment data of wind-induced currents acquired by Baines and Knapp (1965). The experimental apparatus consisted of a wind channel with a cross-section of 0.9144 m by 0.9144 m and a length of 12.8 m. The test section was 9.144 m long, and the water depth was 0.3048 m. Observations were made at different points over the depth for two wind conditions with average wind speeds of 3.901 and 6.096 m/s. In the numerical model, the same conditions were deployed. The channel is discretized with square grid cells of side 0.061 m. Eighteen layers are used in the depth direction. The relative layer thickness (layer thickness over flow depth) from top to bottom is 0.005, 0.005, 0.01, 0.02, 0.03, 0.04, 0.05, 0.065, 0.085, 0.1, 0.1, 0.1, 0.1, 0.1, 0.05, 0.03 and 0.01. The bed friction coefficient c_f is 0.005. The mixing layer model is used, with two different vertical mixing length functions. One is the classical formula of mixing length for open-channel flow expressed in Eq. (4.5) and the other one is newly proposed as follows:

$$l_{mV} = \begin{cases} \kappa z & z < 0.5h \\ \kappa(h - z) & z \geq 0.5h \end{cases} \tag{4.35}$$

The measured and calculated velocities for the two cases with wind speed of 3.902 and 6.096 m/s are compared in Figs. 4.12 and 4.13, respectively. It can be seen that the model with the vertical mixing vertical length function (4.35) reproduces well the current velocity profile in the entire water depth, except some error at the water surface. The model with the classical mixing length function in Eq. (4.5) predicts well the velocity profile in the middle and lower depth layers, but has larger errors near the water surface.

It should be noted that the results obtained by Eq. (4.35) are better than those by Eq. (4.5), but the model is less stable and requires shorter time step when Eq. (4.35) is used. The time step is 15 sec when Eq. (4.5) is used, and 1 sec when Eq. (4.35) is used. If the current velocity near the water surface is not the main concern, Eq. (4.5) can be used since it is much more efficient in computation.

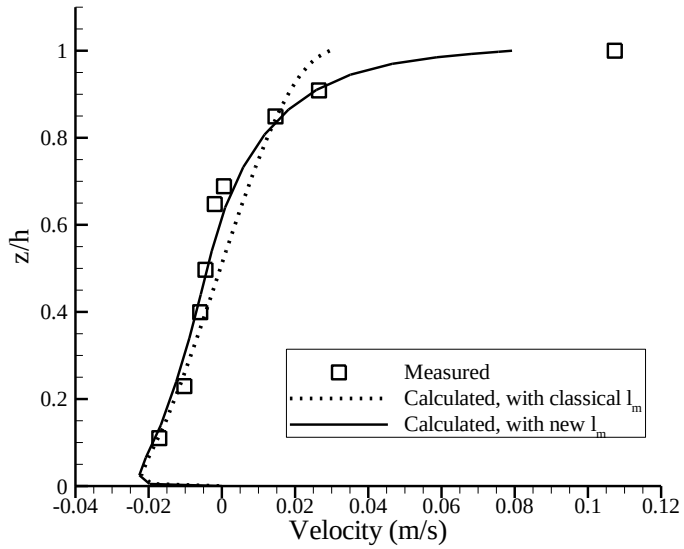

Figure 4.12 Measured and simulated current velocities induced by wind with a speed of 3.901 m/s

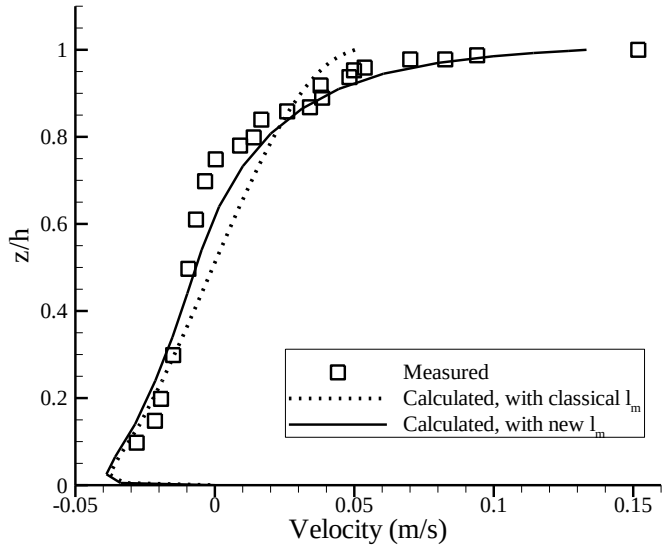

Figure 4.13 Measured and simulated current velocities induced by wind with a speed of 6.096 m/s

4.4.4 Undertow Flow Induced by Waves on a Slopped Beach

The undertow is a near-bottom compensating cross-shore flow for mass transport and Stokes drift in the surf zone. The developed 3-D shallow water flow model coupled with the CMS-Wave model was applied to simulate the undertow flow in this case. The experiment was conducted by Ting and Kirby (1994) in a two-dimensional wave tank, 40 m long, 0.6 m wide and 1.0 m deep, as shown in Fig. 4.14. The bottom slope was 1:35, and the water depth in the horizontal region was 0.4 m. The experimental data were obtained with a wave height of 0.128 m in the horizontal region and a wave period of 5 sec.

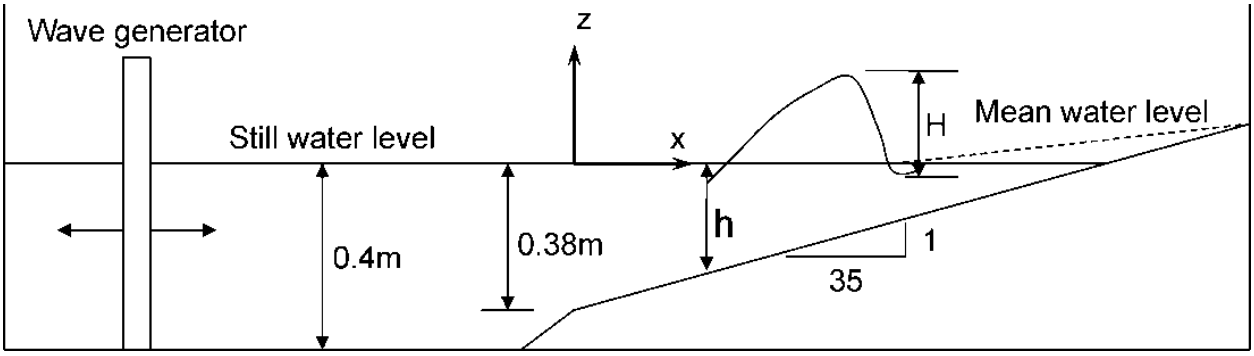

Figure 4.14 Cross-shore Plan of Ting and Kirby (1994) Undertow Flow Experiment Setup

The computational domain included the horizontal region and the beach. The cross-shore grid spacing was 0.5 m, and 16 layers with a uniform spacing were used in the vertical direction. The simulation starts from a still water condition and reaches to the phase-averaged steady state reported in the experiment. The time step was 60 sec. The total simulation period was 3 hours, which was much longer than the time required to reach a steady flow state. The bed friction coefficient c_f is set as 0.0035. The mixing length model in Eq. (4.7) is used, with the current mixing length determined by Eq. (4.5) but two different functions for the vertical wave mixing length. Both functions can be written as $l_{mw} = a\kappa H$, with the coefficient a defined differently. In one function a has a constant value of 0.3 over the flow depth, and in the other function a is expressed as

$$a = \begin{cases} 0.6\,z/\delta & z < \delta \\ 0.6\,(h-z)/(h-\delta) & z \geq \delta \end{cases} \tag{4.36}$$

where δ is the bottom layer thickness, set as $0.1h$ in this test case. Note that for simplicity, δ is not related to the wave boundary layer thickness. However, this can be done in the future by using more test cases. The coefficient 0.6 in Eq. (4.36) is calibrated by comparing the calculated and

measured undertow current velocities. Its validity for other conditions needs to be validated further.

Fig. 4.15 compares the measured and calculated cross-shore profiles of mean water levels and wave heights. The calculation results are obtained with the option of constant coefficient *a* as 0.3 over the depth, but the wave height and water level calculated by using Eq. (4.36) are very similar. In this experiment, the wave breaks at the location x=7.795 m. The predicted wave breaking location is slightly on the offshore side of the measured one. The model underpredicts the maximum wave height. This may be because the wave model is designed for random waves, whereas the present case uses regular waves. The model predicts well the wave setup. The measured and calculated mean water levels are in general good agreement.

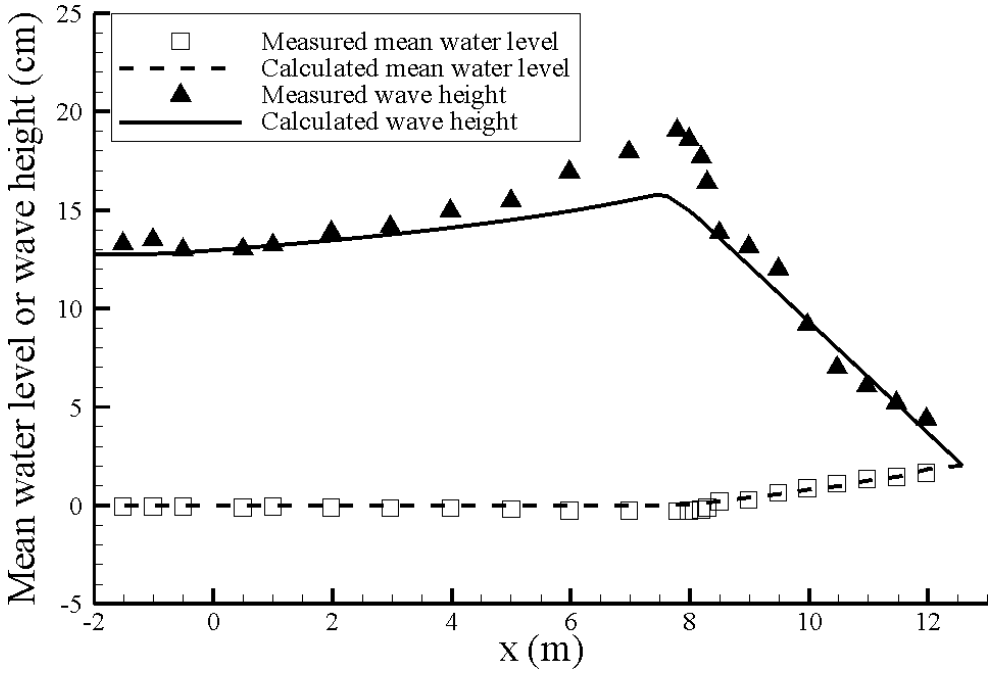

Figure 4.15 Wave height and mean water level in the case of Ting and Kirby (1994) undertow flow experiment

Fig. 4.16 shows the undertow current pattern in the cross-shore vertical plane calculated using the constant *a* option. The calculated undertow offshore flow and upper onshore flow are qualitatively reasonable. Fig. 4.17 shows the calculated and measured phase-averaged flow velocities in six stations at x= 7.795, 8.345, 8.795, 9.295, 9.795, and 10.395 m. The results using both options of coefficient *a* are reported in Fig. 4.17. When the constant coefficient *a* is used the model predicts gentle gradients of velocity between the upper onshore and lower offshore flows, which are less accurate than the sharper gradients obtained by the variable coefficient *a*, in comparison with sharp gradients observed in the experiment. The undertow layer thickness is also better predicted by using the option of variable coefficient *a*. However, noticeable differences exist between the calculated onshore currents between the two options and the measured data. Because the model predicts a steady flow state, the calculated onshore and offshore fluxes are equal because of mass balance ensured by the numerical model; however, the onshore flux is smaller than the offshore flux in the experiment, which is due to that only the currents under the wave trough were sampled so that the onshore current is not accurately represented in the measurements. In particular, the Stokes drift is not included in the measurement data, whereas the present flow model lumps the Stokes drift into the phase-averaged currents. Considering the uncertainty or error in the measured onshore current, we can make a conclusion that the model with the option of variable coefficient *a* expressed in Eq. (4.36) can more accurately simulate the undertow current induced by waves over a sloping beach than using the option of constant coefficient *a*. In general, both options give qualitatively reasonable results.

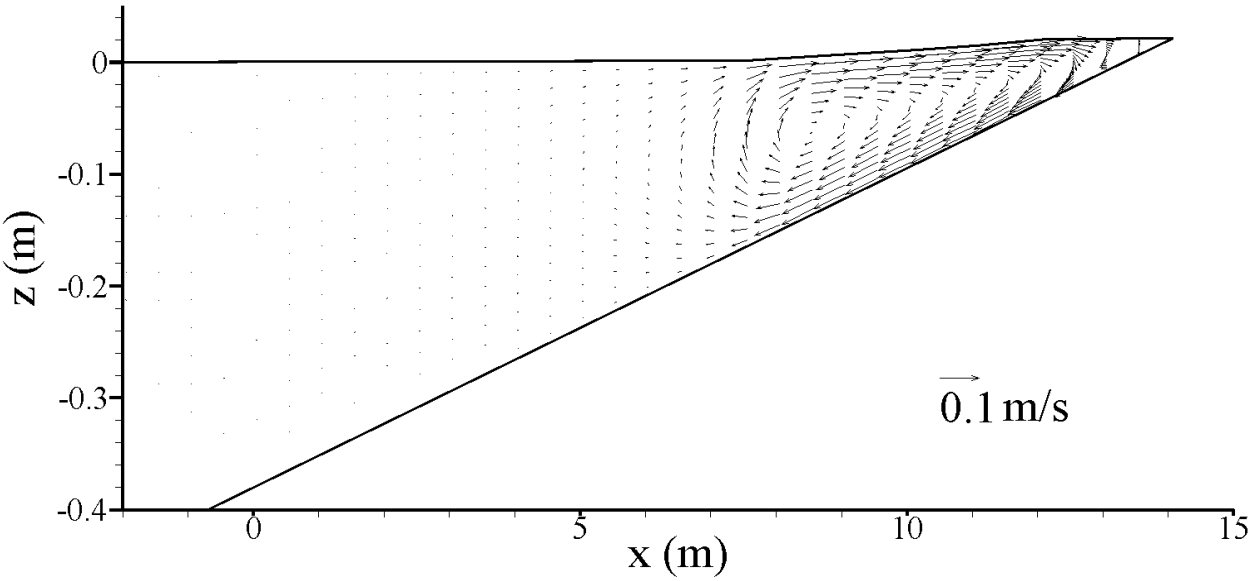

Figure 4.16 Calculated undertow flow in the case of Ting and Kirby (1994) experiment

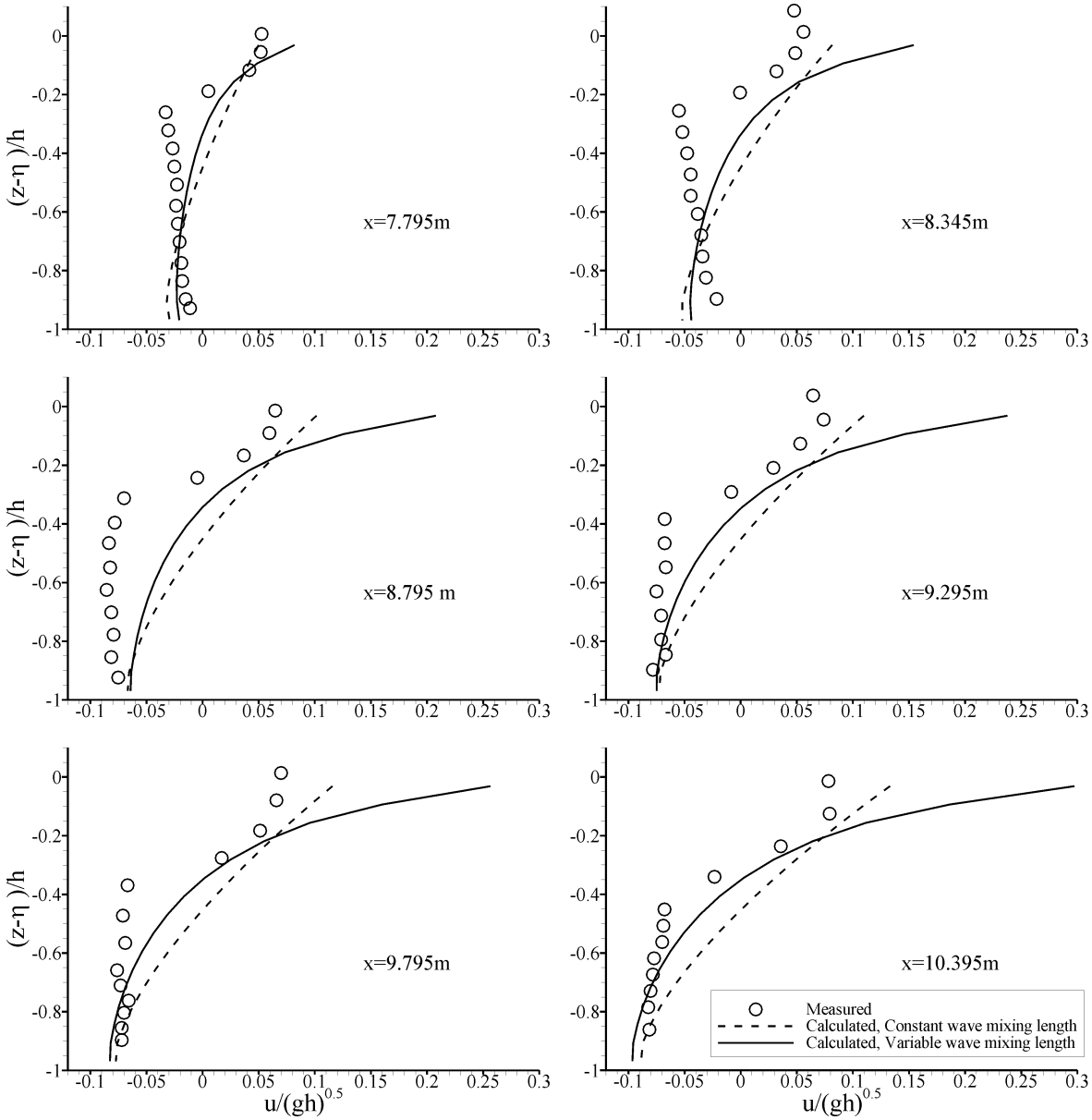

Figure 4.17 Vertical profile of cross-shore current in the case of Ting and Kirby (1994) experiment

CHAPTER V

3-D NONUNIFORM SEDIMENT TRANSPORT MODEL UNDER CURRENT AND WAVES

Some coastal sediment transport models are based on the assumption that the bed load or total load (both bed load and suspended load) instantaneously reaches the equilibrium state, calculate the sediment transport rate using empirical formulas, and then determine the bed change by solving the sediment mass balance equation or the Exner (1925) equation (Stuiksma *et al.* 1985, Chesher *et al.* 1993, Roelvink and Banning 1994, Ranasinghe *et al.* 1999, Cayocca 2001, Fortunato and Olveira 2004, Buttolph *et al.* 2006, and Warner *et al.* 2008). However, because of the dynamic nature of currents and waves on the coast, the sediment transport in coastal waters usually is not in states of equilibrium. The assumption of local equilibrium may lead to unrealistic results and significant errors in cases of strong erosion and deposition. Therefore, a non-equilibrium transport model, which is more realistic for sediment transport, is adopted in the present study. Compared to the equilibrium model, the non-equilibrium model describes the temporal and spatial lags between flow and sediment transport.

The water column is usually divided into bed-load zone and suspended-load zone due to the different behaviors between bed load and suspended load. The bed-load zone is from the bed elevation to a certain reference level, which is usually assumed to be about twice the sediment diameter or half the bed-form height. The method to determine the reference level in this study has

been discussed in Chapter 3. The suspended-load zone is from the reference level to the water surface. The present sediment transport model solves the actual transport equations for both bed load and suspended load. The governing equations of non-equilibrium suspended-load and bed-load sediment transport are presented in the following sections.

5.1 Suspended-load Sediment Transport Equation

The suspended load is transported by the turbulent flow in the water column above the bed-load layer. The governing equation of nonuniform suspended-load transport in tensor notation is written as

$$\frac{\partial c_k}{\partial t} + \frac{\partial \left[\left(u_j - \omega_{sk} \delta_{j3} \right) c_k \right]}{\partial x_j} = \frac{\partial}{\partial x_j} \left(\varepsilon_s \frac{\partial c_k}{\partial x_j} \right) \quad \left(k = 1, 2, ..., N \right) \tag{5.1}$$

where c_k is the local concentration of the kth size class of suspended load; ε_s is the turbulent diffusivity of sediment, which is assumed to be proportional to the turbulent eddy viscosity as $\varepsilon_s = \nu_t / \sigma_s$, in which σ_s is the Schmidt number; ω_{sk} is the settling velocity, which will be discussed later; and δ_{j3} is the Kronecker delta with "3" indicating the vertical direction.

5.2 Bed-load Sediment Transport Equation

The bed load moves by rolling, sliding, and saltating within the bed-load layer. The bed load is simulated using the equilibrium transport model (Wang and Adeff 1986, van Rijn 1987, Spasojevic and Holly 1994, and Olsen 2003) or the non-equilibrium transport model (Wu et al. 2000a). The non-equilibrium transport model is more adequate. Because the bed-load layer is very thin, the bed-load transport equation in the 3-D model has the same formulation as the horizontal

2-D model equation, which is written as

$$\frac{\partial\left(q_{bk}/u_{bk}\right)}{\partial t}+\frac{\partial\left(\alpha_{bx}q_{bk}\right)}{\partial x}+\frac{\partial\left(\alpha_{by}q_{bk}\right)}{\partial y}=\frac{1}{L}\left(q_{b*k}-q_{bk}\right)\quad\left(k=1,2,...,N\right)\tag{5.2}$$

where q_{bk} and q_{b*k} are the actual and equilibrium (capacity) transport rates of the *k*th size class of bed load and q_{b*k} is determined using the bed-load capacity formula developed in Chapter 3 (Eqs. 3.26 - 3.29); u_{bk} is the bed-load velocity; L is the adaptation length of sediment, which is related sediment transport and bed form scales and treated as a calibration parameter in this study (Wu, 2007); and α_{bx} and α_{by} are the direction cosines of the calculated bed shear stress, which are calculated as

$$\alpha_{bx}=u_{bx}/\sqrt{u_{bx}^2+u_{by}^2}\quad\text{and}\quad\alpha_{by}=u_{by}/\sqrt{u_{bx}^2+u_{by}^2}\tag{5.3}$$

where u_{bx} and u_{by} are the x- and y-components of bed-load velocity or the flow velocity near the bed.

5.3 Settling Velocity

The settling velocity in clear water is calculated using the following relation proposed by Wu and Wang (2006):

$$\omega_{sk}=\frac{M\nu}{Nd_k}\left[\sqrt{\frac{1}{4}+\left(\frac{4N}{3M^2}D_*^3\right)^{1/n}}-\frac{1}{2}\right]^n\tag{5.4}$$

where the coefficients *M*, *N*, and *n* are given as

$$M=53.5e^{-0.65S_p},\quad N=5.65e^{-2.5S_p},\quad n=0.7+0.9S_p\tag{5.5}$$

where S_p is the Corey shape factor, usually equal to 0.7 for naturally worn particles.

5.4 Bed Change and Bed Material Sorting

The fractional bed change is determined by

$$(1-p'_m)\left(\frac{\partial z_b}{\partial t}\right)_k = D_{bk} - E_{bk} + \frac{1}{L}(q_{bk} - q_{b*k}) \quad (k = 1, 2, ..., N) \tag{5.6}$$

where $(\partial z_b / \partial t)_k$ is the rate of change in bed elevation due to size class k; p'_m is the porosity of sediment deposit, and D_{bk} and E_{bk} are the near-bed deposition and entrainment fluxes of sediment, respectively. The near-bed sediment exchange flux, D_{bk} - E_{bk}, is calculated by

$$D_{bk} - E_{bk} = \omega_{sk}(c_{bk} - c_{b*k}) \quad (k = 1, 2, ..., N) \tag{5.7}$$

where c_{bk} and c_{b*k} are the actual and equilibrium (capacity) near-bed sediment concentrations, respectively. The equilibrium (capacity) near-bed sediment concentration is calculated using an empirical equation described in a later section.

The total rate of change in bed elevation, $\partial z_b / \partial t$, is determined by

$$\frac{\partial z_b}{\partial t} = \sum_{k=1}^{N}\left(\frac{\partial z_b}{\partial t}\right)_k \quad (k = 1, 2, ..., N) \tag{5.8}$$

The size gradation of bed material may vary along the vertical direction due to historical sedimentation. To consider this variation, the bed material above the nonerodible layer is divided into multiple layers, as shown in Fig. 5.1. Bed material sorting is the process in which the bed material changes composition. The sorting of sediments is calculated using the mixing layer concept (Hirano 1971, Karim and Kennedy 1982, Rahuel et al. 1989, Armanini and di Silvio 1988, Wu 1991, and van Nielerk et al. 1992). The mixing layer is the top layer of the bed, in which all

sediment particles are subject to exchange with those moving with flow, i.e., entraining from the mixing layer to the water column or depositing from the water column to the mixing layer. The second layer is a subsurface layer. More underlying subsurface layers can be added. However, the sediment particles in the subsurface layers do not directly exchange with the moving particles.

The temporal variation of the bed-material gradation in the mixing layer is calculated as (Wu 2007)

$$\frac{\partial\left(\delta_m p_{bk}\right)}{\partial t}=\left(\frac{\partial z_b}{\partial t}\right)_k+p_{bk}^{*}\left(\frac{\partial \delta_m}{\partial t}-\frac{\partial z_b}{\partial t}\right)\quad\left(k=1,2,...,N\right) \tag{5.9}$$

where δ_m is the mixing layer thickness; p_{bk} is the fraction of the kth size class of bed material contained in the mixing layer; and p_{bk}^{*} is the p_{bk} when $\partial z_b/\partial t-\partial\delta_m/\partial t\geq 0$ and the fraction of the kth size class of bed material contained in the second layer when $\partial z_b/\partial t-\partial\delta_m/\partial t<0$. The first term on the right-hand side of Eq. (5.9) represents the exchange between moving sediment and bed material, while the last term accounts for the exchange between the mixing layer and the second layer, due to rise or descent of the lower bound of the mixing layer.

The bed-material gradation in the second layer is calculated by

$$\frac{\partial\left(\delta_s p_{sbk}\right)}{\partial t}=-p_{bk}^{*}\left(\frac{\partial \delta_m}{\partial t}-\frac{\partial z_b}{\partial t}\right)\quad\left(k=1,2,...,N\right) \tag{5.10}$$

where δ_s is the second layer thickness; and p_{sbk} is the fraction of the kth size class of bed material contained in the second layer. Eq. (5.10) assumes no exchange between the second and third layers.

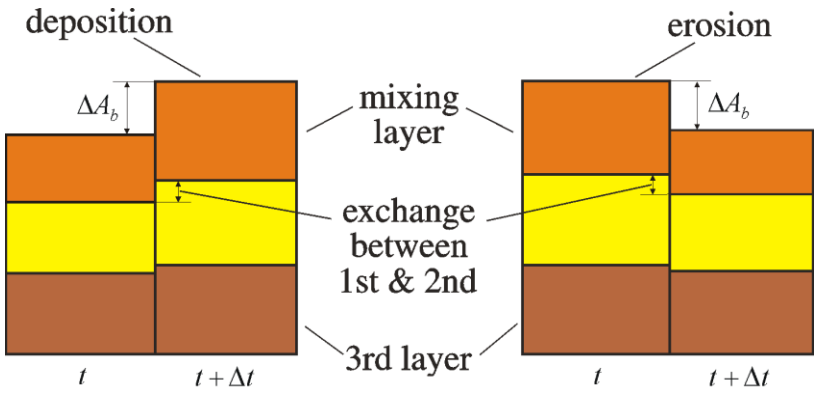

Figure 5.1 Multiple Layer Model for Bed Material Sorting

5.5 Boundary Conditions

5.5.1 Vertical Boundary Conditions

The net vertical sediment flux across the water surface should be zero and, thus, the suspended-load boundary condition at the water surface is

$$\left(\varepsilon_s \frac{\partial c_k}{\partial z} + \omega_{sk} c_k\right)_{z=z_s} = 0 \quad (k = 1, 2, ..., N) \tag{5.11}$$

There are usually two approaches to specify the suspended-load boundary condition at the interface between the suspended-load and bed-load zone. One approach is to assume the near-bed suspended-load concentration to be at equilibrium:

$$c_k\big|_{z=z_b+\delta} = c_{b*} \quad (k = 1, 2, ..., N) \tag{5.12}$$

where c_{b*k} is the equilibrium sediment concentration of kth size at the interface. The model in this study adopts the other approach, which is to assume that the near-bed sediment entrainment flux is at the capacity of flow picking up sediment under the considered flow conditions and the bed sediment configurations:

$$E_{bk} = -\varepsilon_s \left.\frac{\partial c_k}{\partial z}\right|_{z=z_b+\delta} = \omega_{sk} c_{b*k} \quad (k = 1, 2, ..., N) \tag{5.13}$$

where E_{bk} is the entrainment flux of the sediment at the interface. Correspondingly, the deposition flux at the interface is defined as

$$D_{bk} = \omega_{sk} c_{bk} \quad (k = 1, 2, ..., N) \tag{5.14}$$

where c_{bk} is the suspended-load concentration at the interface between the suspended-load and bed-load zones.

5.5.2 Horizontal Boundary Conditions

Traditional lateral boundary conditions are used in the developed sediment transport model. At solid boundary, i.e., interface between dry and wet cells, there is no sediment flux across the boundary. Inflow boundaries may be assigned a specific concentration, or the equilibrium concentration. Outflow boundaries are assigned a zero-gradient boundary condition for sediment concentration.

5.6 Discretization of Sediment Transport Equations

5.6.1 Suspended-load Transport Equation

The suspended-load transport equation is discretized based on the same mesh as the flow model, which is quadtree rectangular mesh in the horizontal plane and sigma coordinate in the vertical direction (see Figs. 4.1). Figs. 5.2 and 5.3 show the vertical mesh and 3-D control volume for the sediment model, respectively. The bed load is a thin layer below the suspended load region.

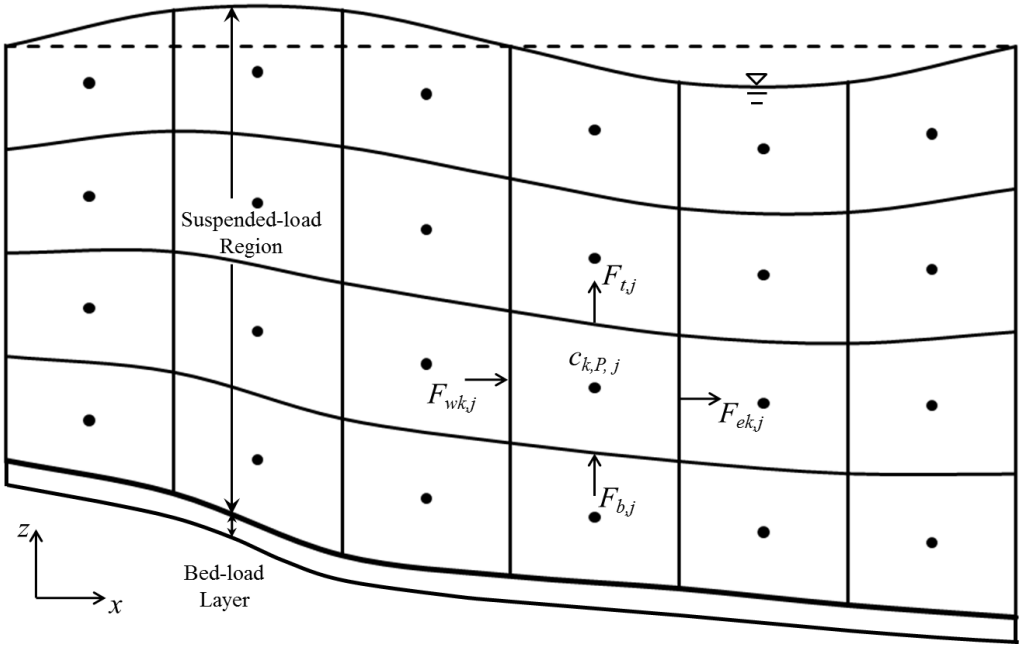

Figure 5.2 Vertical Mesh for Sediment Transport Model

To solve the suspended-load transport equation (5.1), the sediment settling term can be treated as a source term or combined with the vertical convection term. Wu et al. (2000a) suggested the former approach would be better. Thus, Eq. (5.1) can be rewritten as

$$\frac{\partial c_k}{\partial t}+\frac{\partial\left(u_j c_k\right)}{\partial x_j}=\frac{\partial}{\partial x_j}\left(\varepsilon_s\frac{\partial c_k}{\partial x_j}\right)+\frac{\partial\left[\left(\omega_{sk}\delta_{j3}\right)c_k\right]}{\partial x_j}\quad\left(k=1,2,...,N\right)\tag{5.15}$$

Integrating Eq. (5.15) over a 3-D control volume (see Fig. 5.3), yields

$$\frac{\partial c_{k,j}}{\partial t}\Delta V_{P,j}+\left[\sum_{m=1}^{m_e}\left(uc_k\Delta A\right)_{em,j}-\sum_{m=1}^{m_w}\left(uc_k\Delta A\right)_{wm,j}\right]+$$
$$\left[\sum_{m=1}^{m_n}\left(vc_k\Delta A\right)_{nm,j}-\sum_{m=1}^{m_s}\left(vc_k\Delta A\right)_{sm,j}\right]+\left[\left(wc_k\Delta A\right)_{t,j}-\left(wc_k\Delta A\right)_{b,j}\right]$$
$$=\left[\sum_{m=1}^{m_e}\left(\varepsilon_s\frac{\partial c_k}{\partial x}\Delta A\right)_{em,j}-\sum_{m=1}^{m_w}\left(\varepsilon_s\frac{\partial c_k}{\partial x}\Delta A\right)_{wm,j}\right]+\left[\sum_{m=1}^{m_n}\left(\varepsilon_s\frac{\partial c_k}{\partial y}\Delta A\right)_{nm,j}-\sum_{m=1}^{m_s}\left(\varepsilon_s\frac{\partial c_k}{\partial y}\Delta A\right)_{sm,j}\right] \quad (5.16)$$
$$+\left[\left(\varepsilon_s\frac{\partial c_k}{\partial z}\Delta A\right)_{t,j}-\left(\varepsilon_s\frac{\partial c_k}{\partial z}\Delta A\right)_{b,j}\right]+\left[\left(\omega_{sk}c_k\Delta A\right)_{t,j}-\left(\omega_{sk}c_k\Delta A\right)_{b,j}\right]\quad\left(k=1,2,...,N\right)$$

where $\Delta V_{P,j}$ is the control volume of cell P with the vertical cell index j; u, v, and w are the velocities in x-, y-, and, z-directions; the subscripts w, e, s, n, b and t denote the west (negative x), east (positive x), south (negative y), north (positive y), bottom (negative z) and top (positive z) sides of the control volume; the subscript m is the index of the horizontal faces, with a value of 1 or 2; and m_w, m_e, m_s, and m_n are the numbers of cell faces at the west, east, south, and north sides of the cell. For the control volume shown in Fig. 5.3, m_w=1, m_e=2, m_s=1, and m_n=1.

Discretization of the temporal derivative in Eq. (5.16) using the backward difference scheme, the convection terms using exponential scheme, and source term using an upwinding scheme, and the diffusion terms using the central difference scheme leads to

$$\frac{\Delta V_{P,j}^{n+1}c_{k,P,j}^{n+1}-\Delta V_{P,j}^{n}c_{k,P,j}^{n}}{\Delta t}=\sum_{m=1}^{m_w}\left(a_W c_{k,W}^{n+1}\right)_{m,j}+\sum_{m=1}^{m_e}\left(a_E c_{k,E}^{n+1}\right)_{m,j}+\sum_{m=1}^{m_s}\left(a_S c_{k,S}^{n+1}\right)_{m,j}+\sum_{m=1}^{m_n}\left(a_N c_{k,N}^{n+1}\right)_{m,j}$$
$$+\left(a_B c_{k,B}^{n+1}\right)_j+\left(a_T c_{k,T}^{n+1}\right)_j-\left(a_P c_{k,P}^{n+1}\right)_j+S_{k,j}\quad\left(k=1,2,...,N\right) \quad (5.17)$$

where Δt is the time step length; the superscript n denotes time level; the subscripts W, E, S, N, B and T denote the west (negative x), east (positive x), south (negative y), north (positive y), bottom (negative z) and top (positive z) neighboring nodes of node P; a is coefficients; and S is the source term.

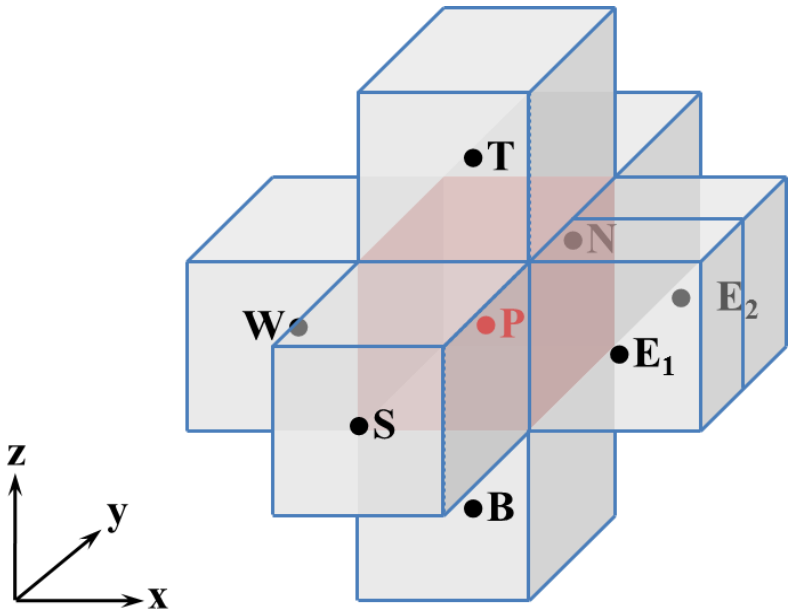

Figure 5.3 3-D Control Volume of Node P and its Neighboring Cells

With discretizing the convection by exponential scheme and source terms by the upwinding scheme, the coefficients *a* and *S* are expressed as

$$a_{Wm,j}=\frac{F_{wm,j}\exp\left(F_{wm,j}/D_{wm,j}\right)}{\exp\left(F_{wm,j}/D_{wm,j}\right)-1},\quad a_{Em,j}=\frac{F_{em,j}}{\exp\left(F_{em,j}/D_{em,j}\right)-1}$$

$$a_{Sm,j}=\frac{F_{sm,j}\exp\left(F_{sm,j}/D_{sm,j}\right)}{\exp\left(F_{sm,j}/D_{sm,j}\right)-1},\quad a_{Nm,j}=\frac{F_{nm,j}}{\exp\left(F_{nm,j}/D_{nm,j}\right)-1}$$

$$a_{B,j}=\frac{F_{bm,j}\exp\left(F_{bm,j}/D_{bm,j}\right)}{\exp\left(F_{bm,j}/D_{bm,j}\right)-1},\quad a_{T,j}=\frac{F_{tm,j}}{\exp\left(F_{tm,j}/D_{tm,j}\right)-1} \tag{5.18}$$

$$a_P=\sum_{m=1}^{m_w}a_{Wm,j}+\sum_{m=1}^{m_e}a_{Em,j}+\sum_{m=1}^{m_s}a_{Sm,j}+\sum_{m=1}^{m_n}a_{Nm,j}+a_{B,j}+a_{T,j}+$$

$$\left(\sum_{m=1}^{m_e}F_{em,j}-\sum_{m=1}^{m_w}F_{wm,j}+\sum_{m=1}^{m_n}F_{nm,j}-\sum_{m=1}^{m_s}F_{sm,j}+F_{t,j}-F_{b,j}\right)$$

$$S_{k,j}=S_{k,U,j}+S_{k,P,j}c_{k,P,j}^{n+1},\quad \text{with}\quad S_{k,U,j}=\left(\omega_{sk}\Delta A\right)_{t,j}c_{k,T,j}^{n+1}\quad \text{and}\quad S_{k,P,j}=-\left(\omega_{sk}\Delta A\right)_{b,j}$$

where ΔA denotes the areas of cell faces; F and D are defined as

$$
\begin{aligned}
F_{wm,j} &= \left(u_w \Delta A_w\right)_{m,j}, \quad F_{em,j} = \left(u_e \Delta A_e\right)_{m,j} \\
F_{sm,j} &= \left(v_s \Delta A_s\right)_{m,j}, \quad F_{nm,j} = \left(v_n \Delta A_n\right)_{m,j} \\
F_{b,j} &= \left(w_b \Delta A_b\right)_j, \quad F_{t,j} = \left(w_t \Delta A_t\right)_j \\
D_{wm,j} &= \left(\frac{\varepsilon_s \Delta A_w}{\Delta x_w}\right)_{m,j}, \quad D_{em,j} = \left(\frac{\varepsilon_s \Delta A_e}{\Delta x_e}\right)_{m,j} \\
D_{sm,j} &= \left(\frac{\varepsilon_s \Delta A_s}{\Delta y_s}\right)_{m,j}, \quad D_{nm,j} = \left(\frac{\varepsilon_s \Delta A_n}{\Delta y_n}\right)_{m,j} \\
D_{b,j} &= \left(\frac{\varepsilon_s \Delta A_b}{\Delta z_b}\right)_j, \quad D_{t,j} = \left(\frac{\varepsilon_s \Delta A_t}{\Delta z_t}\right)_j
\end{aligned}
\tag{5.19}
$$

Rearranging Eq. (5.18) by putting all the $c_{k,P}^{n+1}$ terms on the left hand side of the equation, the final discretization form of Eq. (5.15) can be written as

$$
\begin{aligned}
a'_{P,j} c_{k,P,j}^{n+1} = &\sum_{m=1}^{m_w} \left(a_W c_{k,W}^{n+1}\right)_{m,j} + \sum_{m=1}^{m_e} \left(a_E c_{k,E}^{n+1}\right)_{m,j} + \sum_{m=1}^{m_s} \left(a_S c_{k,S}^{n+1}\right)_{m,j} + \sum_{m=1}^{m_n} \left(a_N c_{k,N}^{n+1}\right)_{m,j} \\
&+ \left(a_B c_{k,B}^{n+1}\right)_j + \left(a_T c_{k,T}^{n+1}\right)_j + S'_{k,U,j} \quad \left(k = 1, 2, ..., N\right)
\end{aligned}
\tag{5.20}
$$

where

$$
\begin{aligned}
a'_{P,j} &= a_{P,j} + \Delta V_{P,j}^{n+1} / \Delta t - S_{k,P,j} \\
S'_{k,U,j} &= S_{k,U,j} + \Delta V_{P,j}^{n} c_{k,P,j}^{n} / \Delta t
\end{aligned}
\tag{5.21}
$$

Note that the convection terms are also discretized using other numerical schemes with upwinding capability, such as the hybrid upwind/central scheme (Spalding, 1972), exponential scheme (Spalding, 1972) and HLPA scheme (Zhu, 1991). The HLPA scheme is approximately second-order accurate, while the hybrid and exponential schemes have accuracy between first and second orders. With different discretization schemes, the final discretization form of Eq. (5.1)

remains the same as Eq. (5.20) but with the coefficients defined in different ways. Details of these schemes can be found in Wu (2007). The exponential difference scheme is used in this study.

5.6.2 Bed-load Transport Equation

The bed-load model in this study is assumed to be a thin layer below the lowest level of the vertical grid (see Fig. 5.2). Therefore, the bed-load transport equation is discretized based on the quadtree rectangular mesh in a 2-D horizontal plan. The bed-load transport equation (5.2) can be integrated over a 2-D control volume and resulted in

$$\frac{\partial\left(q_{bk}/u_{bk}\right)}{\partial t}\Delta A_p+\left[\sum_{m=1}^{m_e}\left(\alpha_{bx}q_{bk}\Delta y\right)_{em}-\sum_{m=1}^{m_w}\left(\alpha_{bx}q_{bk}\Delta y\right)_{wm}\right]+\left[\sum_{m=1}^{m_n}\left(\alpha_{by}q_{bk}\Delta x\right)_{n}-\sum_{m=1}^{m_s}\left(\alpha_{by}q_{bk}\Delta x\right)_{s}\right] \tag{5.22}$$
$$=\frac{\Delta A_p}{L}\left(q_{b^*k,P}^{n+1}-q_{bk,P}^{n+1}\right)\quad\left(k=1,2,...,N\right)$$

Discretizing Eq. (5.22) using the same manner as the suspended-load transport equation, yields,

$$\frac{\Delta A_P}{\Delta t}\left(\frac{q_{bk,P}^{n+1}}{u_{bk,P}^{n+1}}-\frac{q_{bk,P}^{n}}{u_{bk,P}^{n}}\right)=\sum_{m=1}^{m_w}\left(a_W^q q_{bk,W}^{n+1}\right)_m+\sum_{m=1}^{m_e}\left(a_E^q q_{bk,E}^{n+1}\right)_m+\sum_{m=1}^{m_s}\left(a_S^q q_{bk,S}^{n+1}\right)_m+\sum_{m=1}^{m_n}\left(a_N^q q_{bk,N}^{n+1}\right)_m \tag{5.23}$$
$$-a_P^q q_{bk,P}^{n+1}+S_k^q\quad\left(k=1,2,...,N\right)$$

where the coefficients a^q and the source term S_k^q are defined as

$$\begin{aligned}
&a_{Wm}^q=\max\left(F_{wm}^q,0\right),\ \ a_{Em}^q=\max\left(-F_{em}^q,0\right),\ \ a_{Sm}^q=\max\left(F_{sm}^q,0\right),\ \ a_{Nm}^q=\max\left(-F_{nm}^q,0\right)\\
&a_P^q=\sum_{m=1}^{m_w}a_{Wm}^q+\sum_{m=1}^{m_e}a_{Em}^q+\sum_{m=1}^{m_s}a_{Sm}^q+\sum_{m=1}^{m_n}a_{Nm}^q+\left(\sum_{m=1}^{m_e}F_{em}^q-\sum_{m=1}^{m_w}F_{wm}^q+\sum_{m=1}^{m_n}F_{nm}^q-\sum_{m=1}^{m_s}F_{sm}^q\right)\\
&F_{wm}^q=\left(\alpha_{bx,w}\Delta y\right)_m,\ \ F_{em}^q=\left(\alpha_{bx,e}\Delta y\right)_m,\ \ F_{sm}^q=\left(\alpha_{bx,s}\Delta x\right)_m,\ \ F_{nm}^q=\left(\alpha_{bx,n}\Delta x\right)_m\\
&S_k^q=S_{k,U}^q+S_{k,P}^q q_{bk,P}^{n+1},\ \ \text{with}\ \ S_{k,U}^q=\frac{\Delta A_P}{L}q_{b^*k,P}^{n+1}\ \ \text{and}\ \ S_{k,P}^q=-\frac{\Delta A_P}{L}
\end{aligned} \tag{5.24}$$

Rearranging Eq. (5.22) by putting all the $q_{bk,P}^{n+1}$ terms on the left hand side of the equation, the final discretization form of Eq. (5.24) can be written as

$$a_P'^q q_{bk,P}^{n+1} = \sum_{m=1}^{m_w}\left(a_W^q q_{bk,W}^{n+1}\right)_m + \sum_{m=1}^{m_e}\left(a_E^q q_{bk,E}^{n+1}\right)_m + \sum_{m=1}^{m_s}\left(a_S^q q_{bk,S}^{n+1}\right)_m + \sum_{m=1}^{m_n}\left(a_N^q q_{bk,N}^{n+1}\right)_m + S_{k,U}'^q \quad \left(k=1,2,...,N\right) \tag{5.25}$$

where

$$a_P'^q = a_P^q + \Delta A/\left(u_{bk,P}^{n+1}\Delta t\right) - S_{k,P}^q$$
$$S_{k,U}'^q = S_{k,U}^q + \frac{\Delta A}{\Delta t}\frac{q_{bk,P}^n}{u_{bk,P}^n} \tag{5.26}$$

5.6.3 Bed Change and Bed Material Sorting Equations

The bed change equations (5.8) is discretized as

$$\Delta z_{bk,P} = \frac{\Delta t}{1-p_m'}\left[D_{bk,P}^{n+1} - E_{bk,P}^{n+1} + \frac{1}{L}\left(q_{bk,P}^{n+1} - q_{b^*k,P}^{n+1}\right)\right] \quad \left(k=1,2,...,N\right) \tag{5.27}$$

Thus, the total change in bed elevation is determined by

$$\Delta z_{b,P} = \sum_{k=1}^{N}\Delta z_{bk,P} \tag{5.28}$$

After the bed change is calculated, the bed elevation is updated by

$$z_{b,P}^{n+1} = z_{b,P}^n + \Delta z_{b,P} \tag{5.29}$$

The bed material sorting equations (5.9) and (5.10) are discretized as

$$p_{bk,P}^{n+1} = \frac{\Delta z_{bk,P} + \delta_{m,P}^n p_{bk,P}^n + p_{bk,P}^{*n}\left(\delta_{m,P}^{n+1} - \delta_{m,P}^n - \Delta z_{b,P}\right)}{\delta_{m,P}^{n+1}} \tag{5.30}$$

$$p_{sbk,P}^{n+1} = \frac{\delta_{s,P}^{n} p_{sbk,P}^{n} - p_{bk,P}^{*n}\left(\delta_{m,P}^{n+1} - \delta_{m,P}^{n} - \Delta z_{b,P}\right)}{\delta_{s,P}^{n+1}} \tag{5.31}$$

5.7 Solution of Discretized Sediment Transport Equations

To solve the discretized sediment transport equations, the equilibrium near-bed suspended-load concentration and bed load transport rate need to be determined using empirical formulas. In general, these formulas can be written as

$$c_{b*k} = p_{bk} c_{bk}^{*}, \quad q_{b*k} = p_{bk} q_{bk}^{*} \tag{5.32}$$

In the present model, the sediment transport, bed change, and bed material sorting are solved in a coupled approach. To couple the sediment calculation, the bed-material gradation in Eq. (5.32) is treated implicitly:

$$c_{b*k,P}^{n+1} = p_{bk,P}^{n+1} c_{bk,P}^{*n+1}, \quad q_{b*k,P}^{n+1} = p_{bk,P}^{n+1} q_{bk,P}^{*n+1} \tag{5.33}$$

Also from Eqs. (5.13) and (5.14), one can derive

$$E_{bk,P}^{n+1} = \omega_{sk} c_{b*k,P}^{n+1}, \quad \mathrm{D}_{bk,P}^{n+1} = \omega_{sk} c_{bk,P}^{n+1} \tag{5.34}$$

Substituting Eqs. (5.30), (5.33), and (5.34) into Eq. (5.27) yields

$$\begin{aligned} \Delta z_{bk,P} = & \frac{\omega_{sk}\Delta t \delta_m^{n+1} c_{bk,P}^{n+1} + \Delta t \delta_m^{n+1} q_{bk,P}^{n+1} / L}{\left(1-p_m'\right)\delta_m^{n+1} + \omega_{sk}\Delta t c_{bk,P}^{*n+1} + \Delta t q_{bk,P}^{*n+1} / L} \\ & - \frac{\left(\omega_{sk}\Delta t c_{bk,P}^{*n+1} + \Delta t q_{bk,P}^{*n+1} / L\right)\left[\delta_{m,P}^{n} p_{bk,P}^{n} + \left(\delta_{m,P}^{n+1} - \delta_{m,P}^{n}\right) p_{bk}^{*n}\right]}{\left(1-p_m'\right)\delta_m^{n+1} + \omega_{sk}\Delta t c_{bk,P}^{*n+1} + \Delta t q_{bk,P}^{*n+1} / L} \\ & + \frac{\left(\omega_{sk}\Delta t c_{bk,P}^{*n+1} + \Delta t q_{bk,P}^{*n+1} / L\right) p_{bk}^{*n}}{\left(1-p_m'\right)\delta_m^{n+1} + \omega_{sk}\Delta t c_{bk,P}^{*n+1} + \Delta t q_{bk,P}^{*n+1} / L} \Delta z_{b,P} \end{aligned} \tag{5.35}$$

Summing Eq. (5.35) over all size classes and using Eq. (5.28) yields the following equation for the total change in bed elevation:

$$\Delta z_{b,P} = \left\{ \sum_{k=1}^{N} \frac{\omega_{sk} \Delta t \delta_m^{n+1} c_{bk,P}^{n+1} + \Delta t \delta_m^{n+1} q_{bk,P}^{n+1} / L}{(1-p'_m)\delta_m^{n+1} + \omega_{sk} \Delta t c_{bk,P}^{*n+1} + \Delta t q_{bk,P}^{*n+1} / L} \right.$$
$$\left. - \sum_{k=1}^{N} \frac{\left(\omega_{sk} \Delta t c_{bk,P}^{*n+1} + \Delta t q_{bk,P}^{*n+1} / L\right)\left[\delta_{m,P}^{n} p_{bk,P}^{n} + \left(\delta_{m,P}^{n+1} - \delta_{m,P}^{n}\right) p_{bk}^{*n}\right]}{(1-p'_m)\delta_m^{n+1} + \omega_{sk} \Delta t c_{bk,P}^{*n+1} + \Delta t q_{bk,P}^{*n+1} / L} \right\} / \tag{5.36}$$
$$\left\{ 1 - \sum_{k=1}^{N} \frac{\left(\omega_{sk} \Delta t c_{bk,P}^{*n+1} + \Delta t q_{bk,P}^{*n+1} / L\right) p_{bk}^{*n}}{(1-p'_m)\delta_m^{n+1} + \omega_{sk} \Delta t c_{bk,P}^{*n+1} + \Delta t q_{bk,P}^{*n+1} / L} \right\}$$

Thus, the sediment equations can be solved iteratively in the following sequence:

a) Calculate the flow field;

b) Determine $\Delta z_{b,P}$ using Eq. (5.36) with estimated c_{bk}^{n+1} and q_{bk}^{n+1};

c) Calculate p_{bk}^{n+1} using Eq. (5.30);

d) Calculate $c_{b^*k}^{n+1}$ and $q_{b^*k}^{n+1}$ using Eq. (5.33);

e) Calculate c_{bk}^{n+1} and q_{bk}^{n+1} using Eqs. (5.20) and (5.25);

f) Use the calculated c_{bk}^{n+1} and q_{bk}^{n+1} as new estimates and repeat steps b) - e) until the convergent solution is obtained;

g) Update the bed topography using Eq. (5.9) and the bed-material gradations in the subsurface layers.

5.8 Model Testing

5.8.1 Erosion in a Basin due to Clear Water Inflow

The developed sediment transport model was applied to a laboratory case of erosion due to clear water inflow from a narrow channel in a rectangular basin with a sandy bed layer over a hard bottom. The experiment is good for testing the sediment transport model under strong erosion conditions in the presence of a hard bottom. Thuc (1991) carried out a movable bed laboratory experiment in a 5-m long and 4-m wide rectangular basin, with a narrow 0.2-m-wide inlet and a 1.2-m-wide outlet. The initial water depth was 0.15 m, with a 0.16-m layer of sand ($d50$ = 0.155 mm) over a concrete bottom. The estimated sand settling velocity is 0.013 m/s. The inflow depth-averaged current velocity is 0.6m/s. Bed elevation changes along the longitudinal centerline at 1 and 4 hour were measured. However, no measurements of bed-load or suspended-load were available in this experiment.

The computational grid (see Fig. 5.4) had a constant resolution in the x-direction of 0.1 m and a variable resolution in the y-direction between 0.0333 and 0.1333 m. The computational mesh consisted of 62 rows and 69 columns. The computational time step was 30 sec. A water flux boundary was applied at the upstream end and a water level boundary was applied to the downstream end. Three different values of bed friction coefficients, 0.008, 0.009, and 0.01, were used to obtain the best morphologic change results.

Fig. 5.5 compares the measured and calculated bed changes along the longitudinal centerline at 1 and 4 hr. The calculated erosion and deposition depths are in good agreement with the measured data, in particular at time 4 hr. It was found that c_f = 0.009 provides the best agreement between the calculated and measured bed elevations.

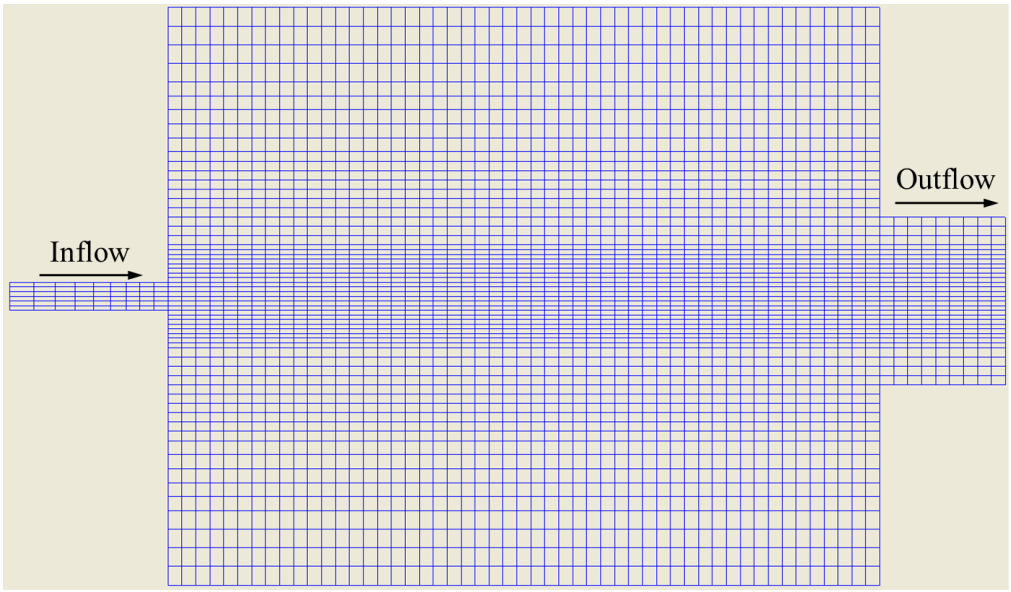

Figure 5.4 Computational Grid for the Thuc (1991) Experiment Case

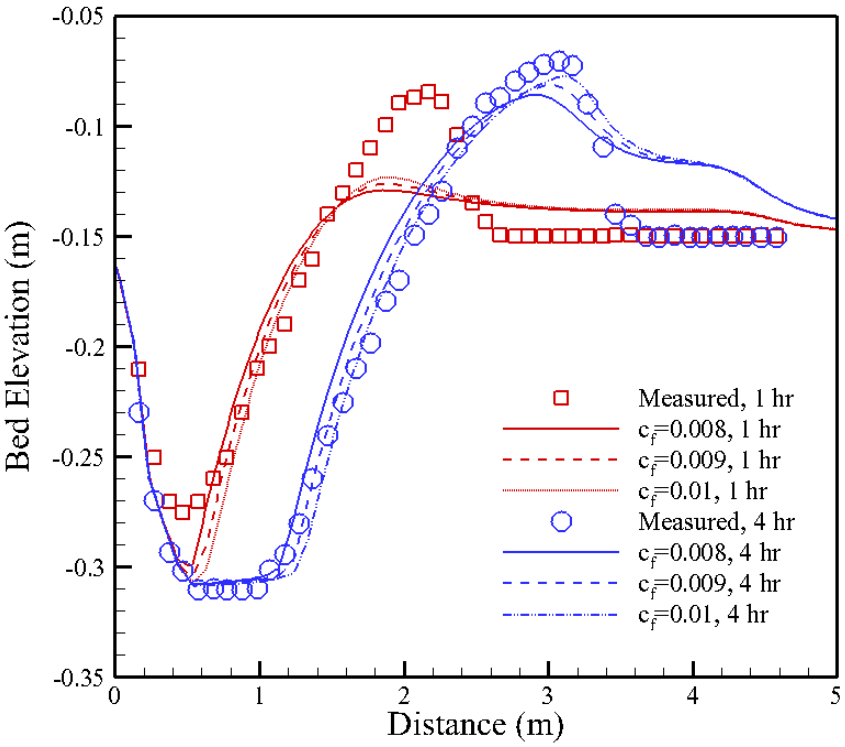

Figure 5.5 Comparison of Calculated and Measured Bed Elevations at 1 and 4 hr for the Thuc (1991) Test Case

5.8.2 Channel Infilling and Migration: Waves Parallel to Flow

The developed sediment transport model was applied to an experiment which concerns the migration and sedimentation of a channel perpendicular to the current direction. The current and the waves are in the same direction. Van Rijn (1986) carried out the experiment in a flume with 17-m in length, 0.3-m in width, and 0.5-m in depth. A channel with side slopes of 1:10 and a depth of 0.125 m was excavated in the measuring section of the flume as shown in Fig. 5.6. The velocity and sediment concentration profiles at initial time were measured at five locations as shown in Fig. 5.6. The bed material consisted of fine well sorted sand with d_{50} = 0.1 mm and d_{90} = 0.13 mm. The water depth and current velocity upstream of the channel were 0.255 m and 0.18 m/s. Regular waves with a period of 1.5 s were generated by a simple wave paddle. The wave height at the upstream was 0.08 m. Sand with the same size and composition as the bed material was supplied at a constant rate of 0.0167 kg/m/s at the upstream end to maintain equilibrium conditions.

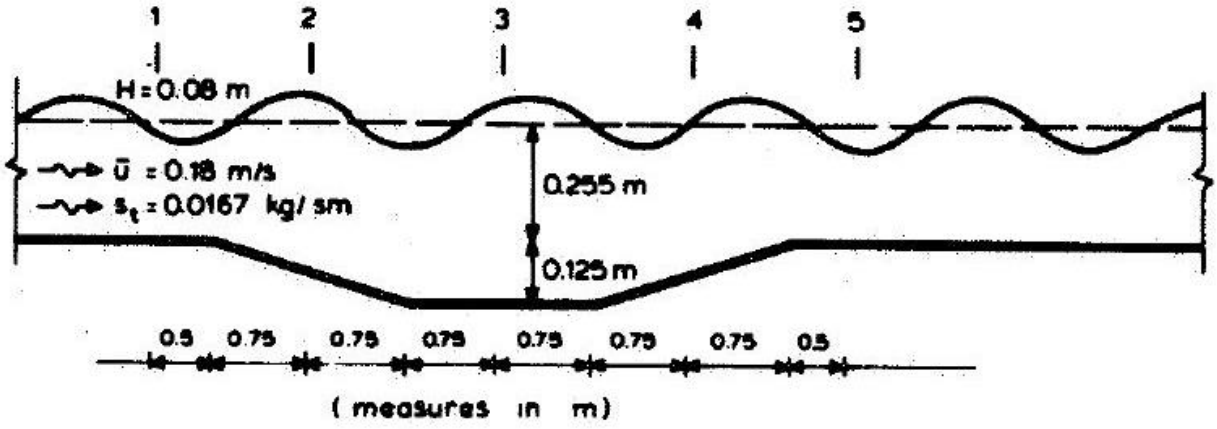

Figure 5.6 Side View of the Experiment Flume (after van Rijn 1986)

The computational grid had a constant resolution of 0.1 m in the x-direction and 0.1 m in the y-direction. The mesh was divided into 13 layers in vertical (z-) direction with finer layers towards the bed. The computational time step was 120 sec. A water flux boundary was applied at the upstream end and a water level boundary was applied to the downstream end. The bottom friction coefficient was set as 0.07 in the model. A range of suspended-load scale factors and Schmidt numbers was used to analyze sensitivity of the results to these parameters.

Fig. 5.7 shows the measured and computed velocity profiles at initial time (t=0). The calculated results have a good agreement with the measurement. The calculated concentration profiles at initial time for different suspended-load scale factors and Schmidt numbers are shown in Figs. 5.8 and 5.9. The suspended-load scale factor is used to multiply the equilibrium near-bed suspended load concentration determined by the empirical formula (3.40). The calculated concentration profiles generally agree with the measurements. With larger suspended-load scale factor and smaller Schmidt Number, the calculated results are more closed to the measurement. The variations of the bed level after 10 hour for different suspended-load scale factors and Schmidt numbers were also compared with the measurement as shown in Figs 5.10 and 5.11. The calculated bed change shows best agreement with the measurement with suspended-load scale factor equal to 2.7 and Schmidt number equal to 1.0.

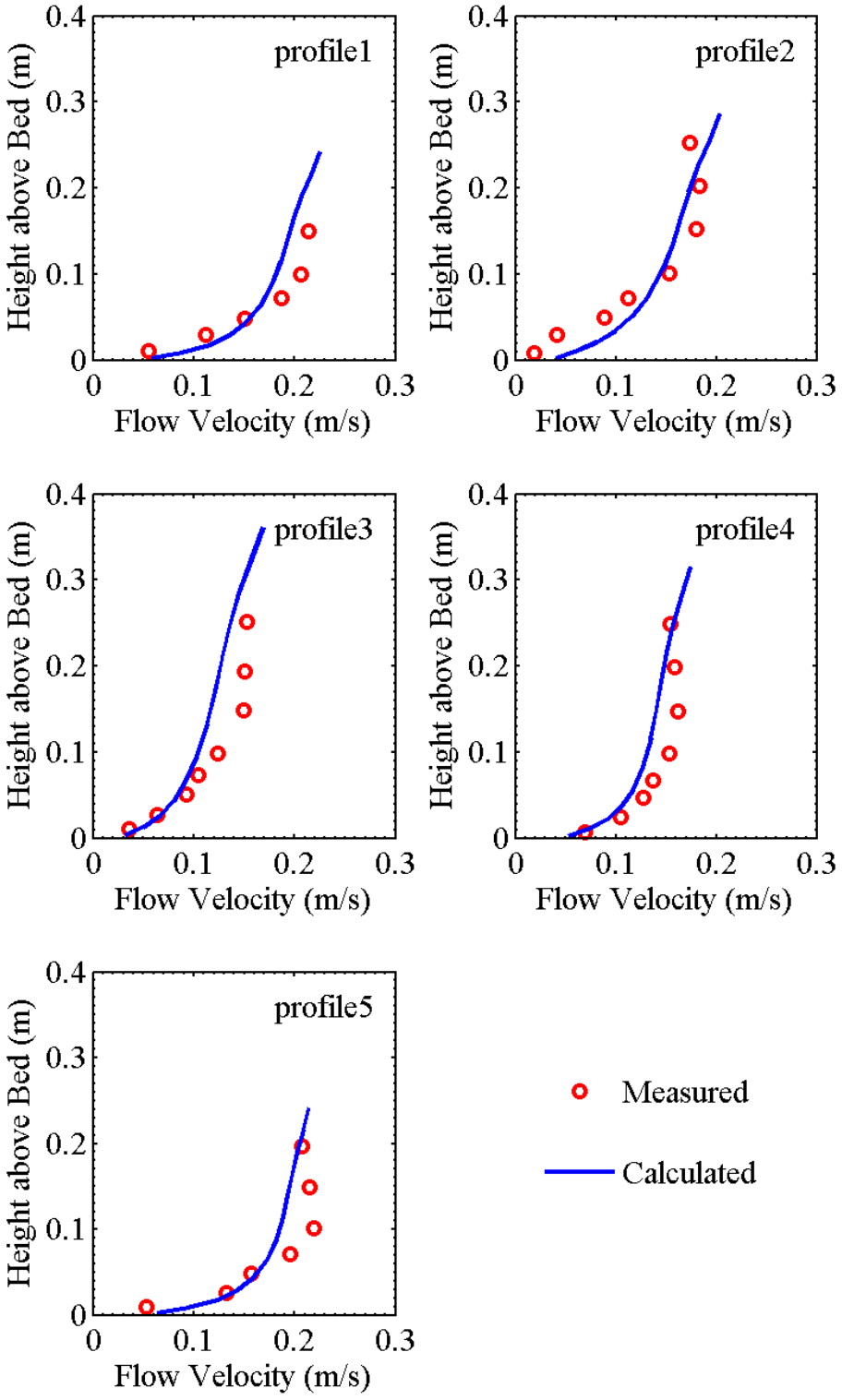

Figure 5.7 Comparison of the Measured and Calculated Velocity Profiles at Initial Time

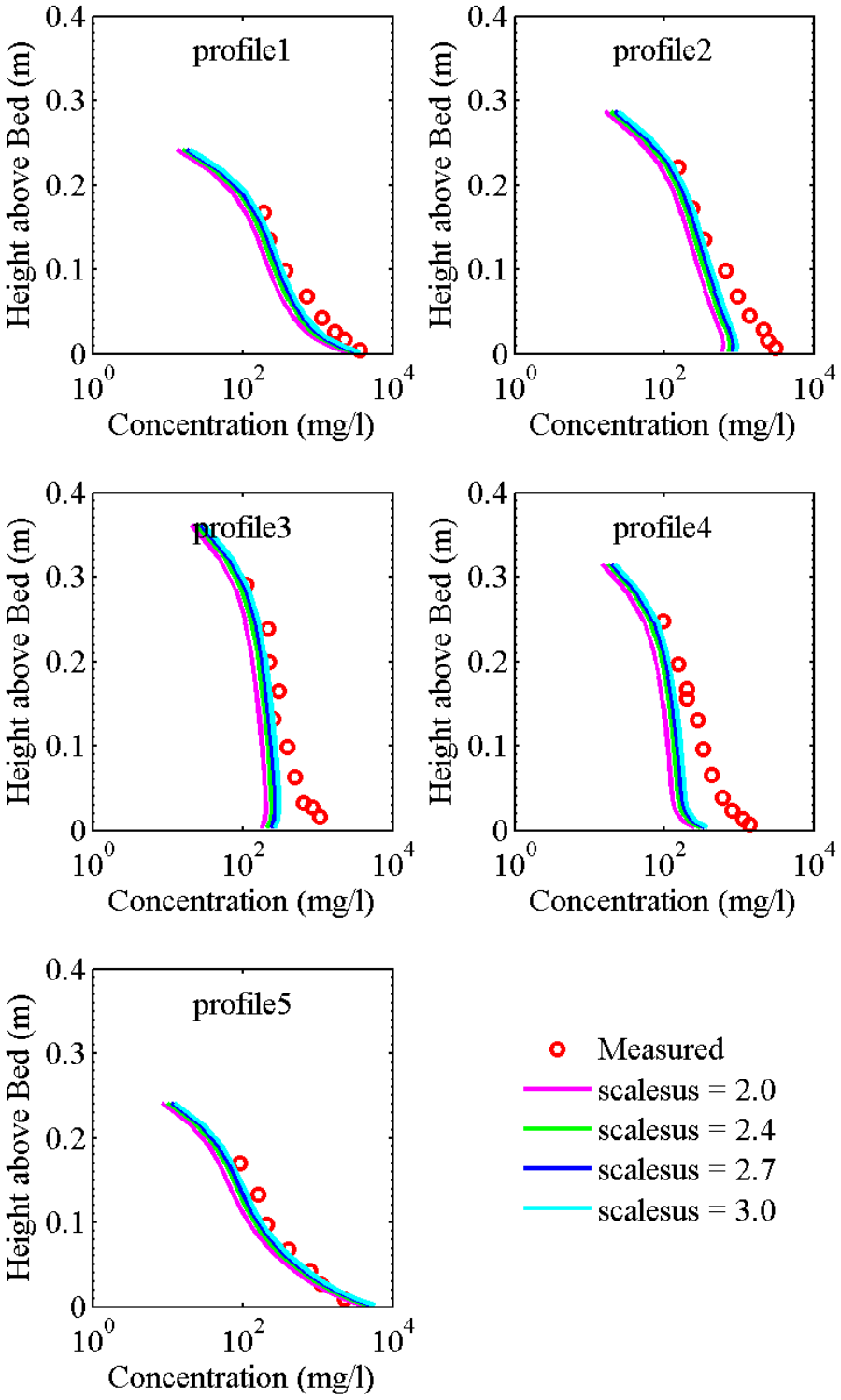

Figure 5.8 Comparison of the Measured and Calculated Concentration Profiles at Initial Time for Different Suspended-load Scale Factors

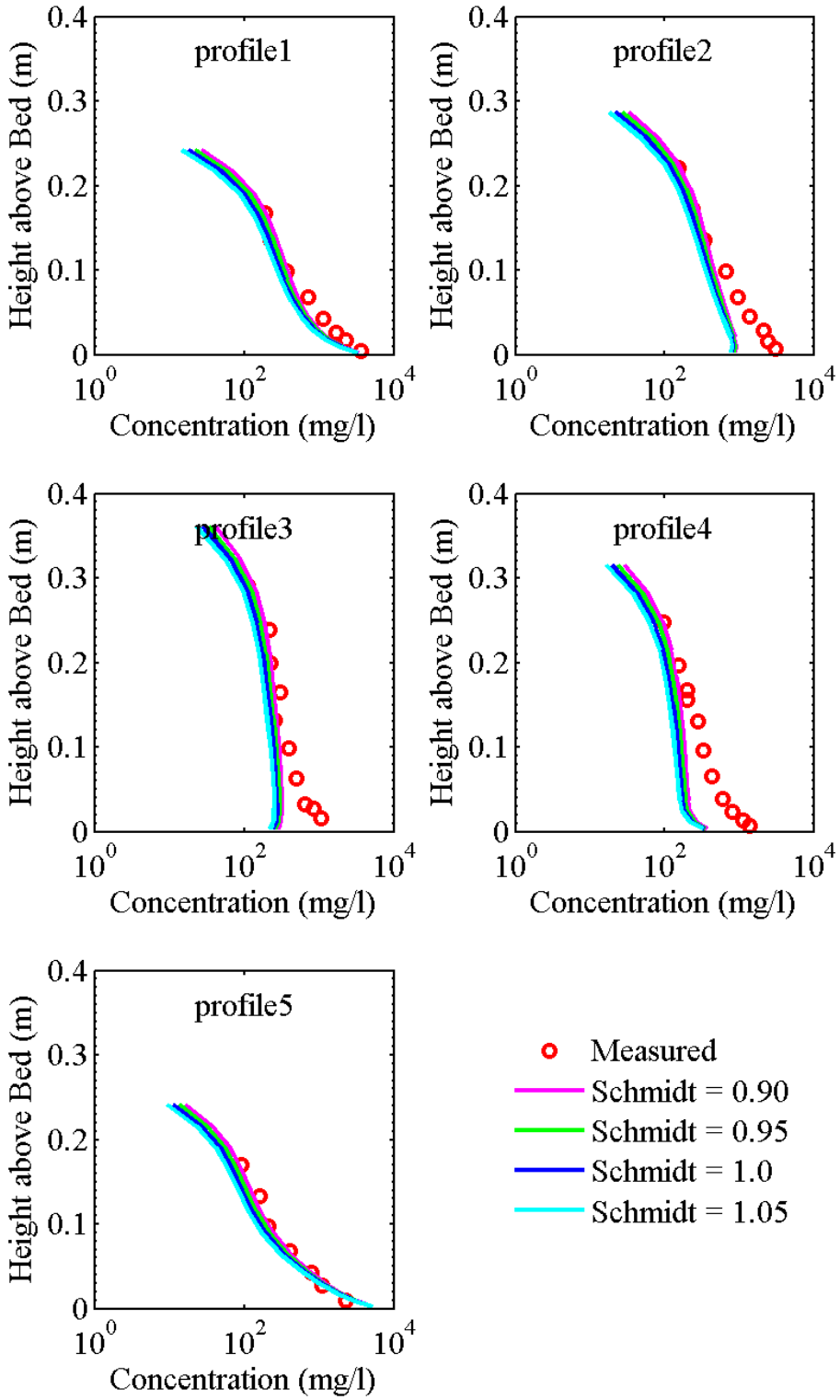

Figure 5.9 Comparison of the Measured and Calculated Concentration Profiles at Initial Time for Different Schmidt Numbers

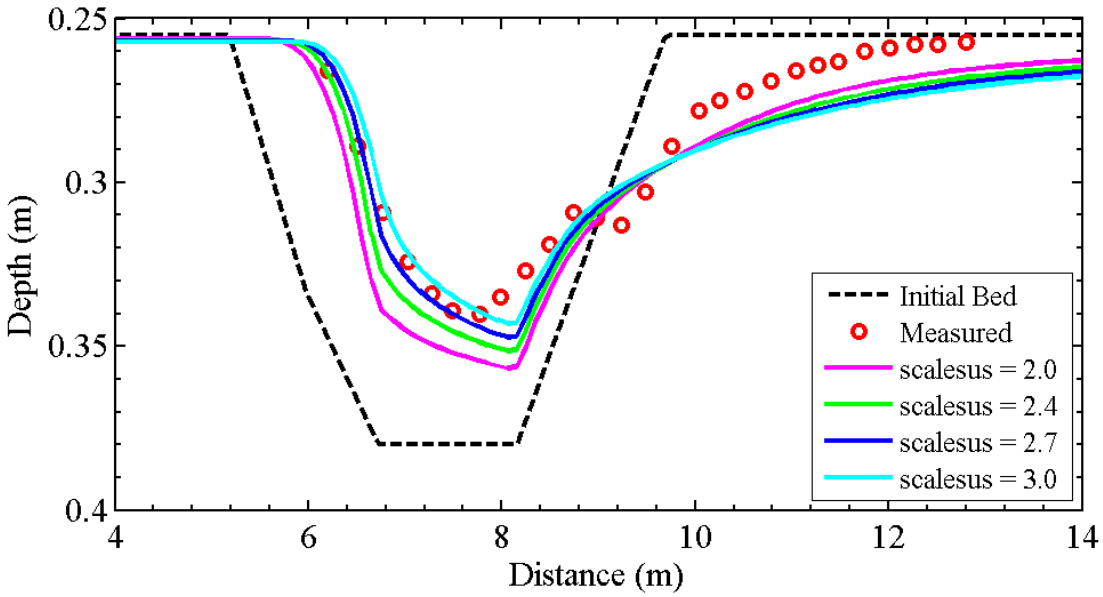

Figure 5.10 Comparison of the Measured and Calculated Bed Changes at 10 hour for Different Suspended-load Scale Factors

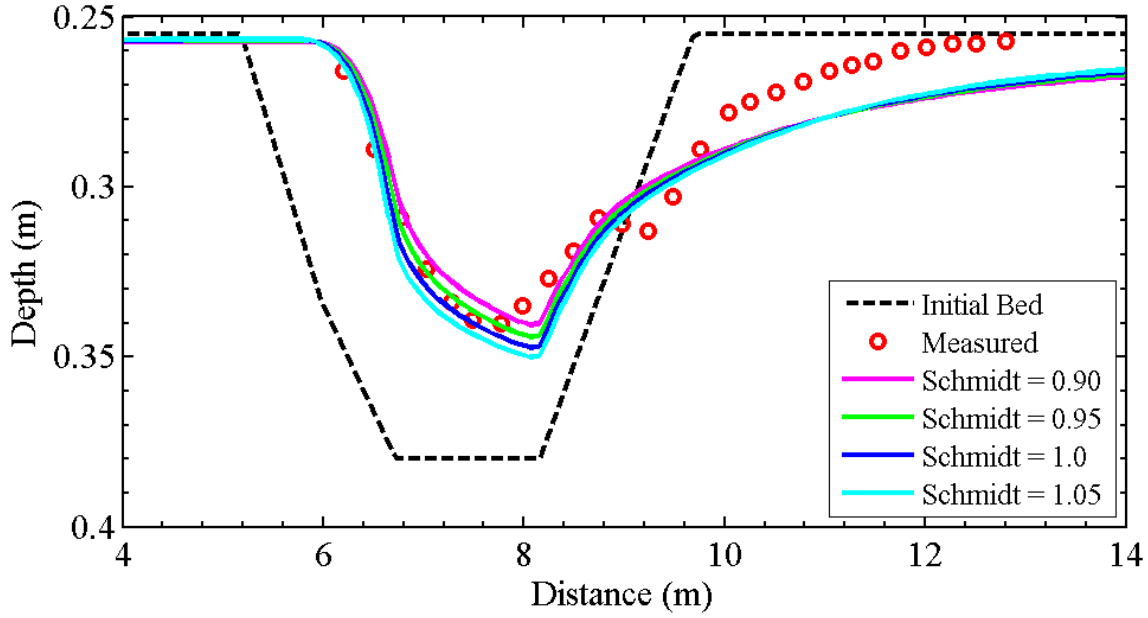

Figure 5.11 Comparison of the Measured and Calculated Bed Changes at 10 hour for Different Schmidt Numbers

5.8.3 Channel Infilling and Migration: Waves Perpendicular to Flow

The developed sediment transport model was applied to an experiment which was conducted by van Rijn and Havinga (1995) in a wave-current basin. Irregular waves (JONSWAP form) were generated by a directional wave generator. The flume was 26.5 m in length and 4 m in width. The channel had side slopes of 1:10 as shown in Fig. 5.12. The bed material consisted of fine well sorted sand with d_{50} = 0.1 mm and d_{90} = 0.13 mm. The water depth and current velocity upstream of the channel were 0.42 m and 0.245 m/s. Irregular waves were generated perpendicular to the current with a peak period of 2.2 s and significant wave height of 0.105 m at the upstream. Sand with the same size and composition as the bed material was supplied at a constant rate of 0.022 kg/m/s at the upstream end to maintain equilibrium conditions.

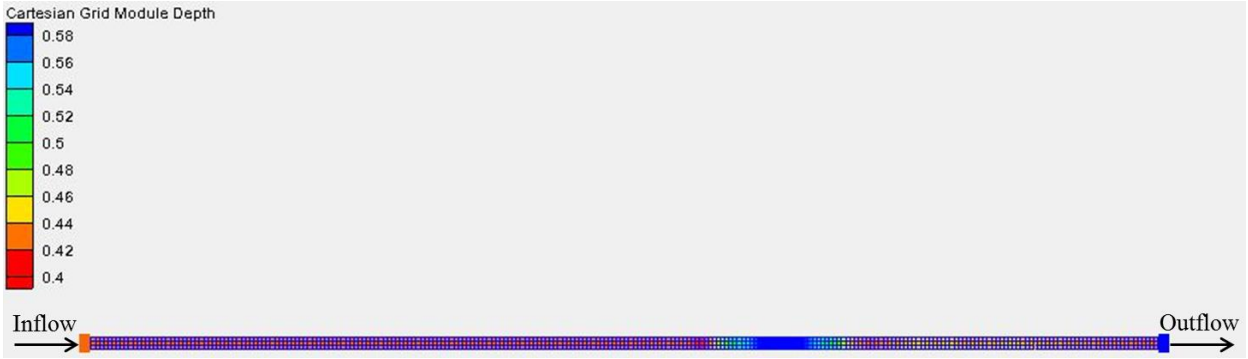

Figure 5.12 Computational Grid for the Van Rijn and Havinga (1995) Experiment Case

The computational grid had a constant resolution of 0.1 m in the x-direction and 0.1 m in the y-direction. The mesh was divided into 13 layers in vertical (z-) direction with finer layers towards the bed. The computational time step was 60 sec. A water flux boundary was applied at the upstream end and a water level boundary was applied to the downstream end. A range of

bed-load adaptation lengths and roughness height constants was used to test this case.

The calculated bed level change after 23.5 hours for different bed-load adaptation lengths and roughness height constants are shown in Figs. 5.13 and 5.14. Four different values of bed-load adaptation length were used: 1 , 5, 10, and 15 m. From Fig. 5.13, one can observe that the results barely changed with the variation of the bed-load adaptation length. This is due to the fact that the suspended load is dominant in this case.

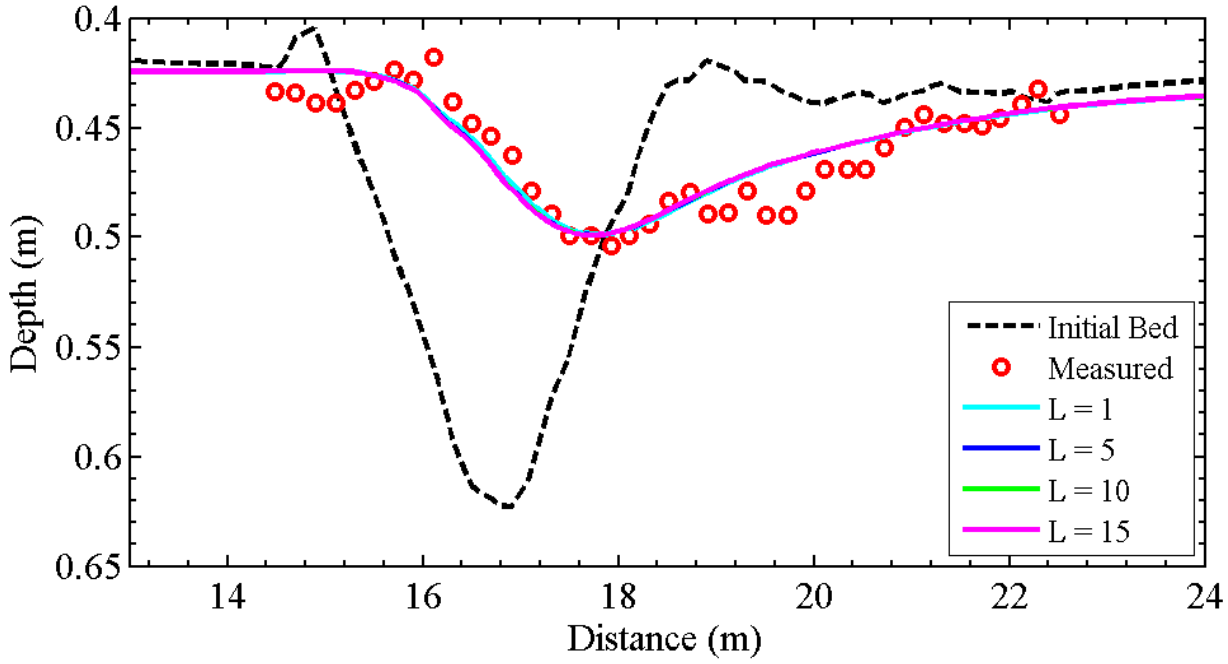

Figure 5.13 Comparison of the Measured and Calculated Bed Change at 23.5 hour for Different Bed-load Adaptation Lengths

Four different values of roughness height constant z_0 (=k_s/30) were used: 0.00054, 0.00057, 0.0006, and 0.00063m. A roughness height constant of 0.00057 m gives the best agreement between the calculated and measured bed level change. Overall, the model performs

well in calculating the bed level change including upstream erosion, channel infilling, and downstream erosion.

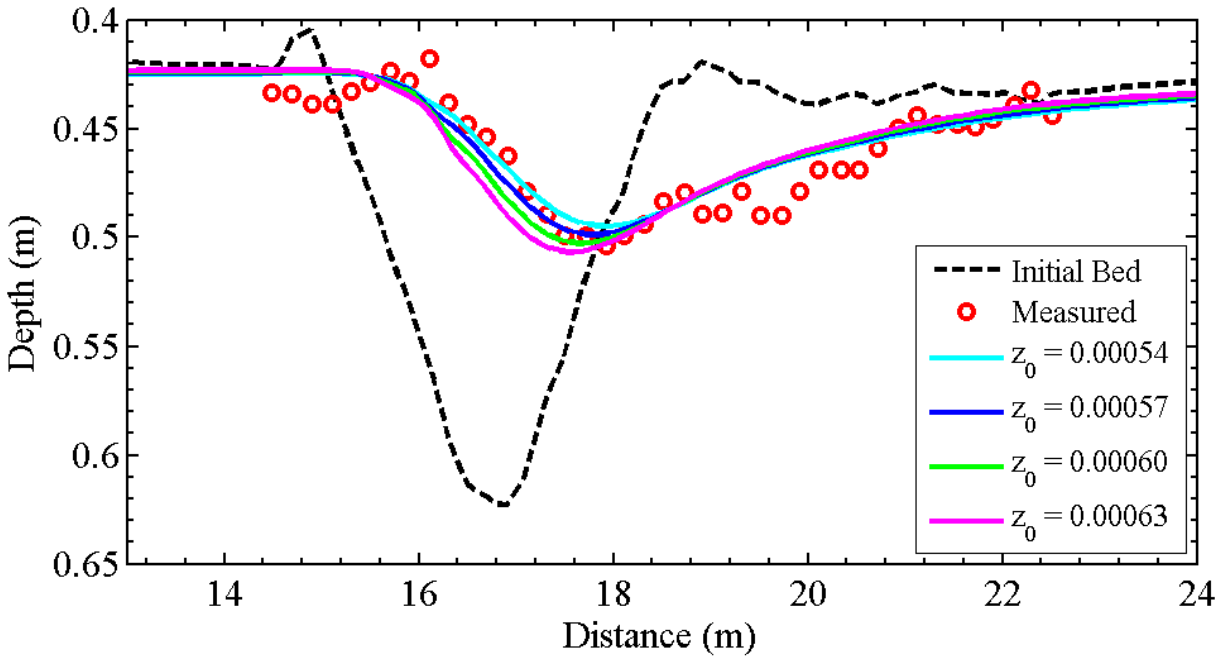

Figure 5.14 Comparison of the Measured and Calculated Bed Change at 23.5 hour for Different Roughness Height Constants

5.8.4 Tidal Flow and Channel Infilling at Shark River Inlet, NJ

The comprehensive performance of the developed model was tested by a field case which involves tidal flow and channel infilling at Shark River Inlet, NJ. The Shark River Inlet is located in Monmouth County along the Atlantic Highlands region of the New Jersey shore and is the northernmost inlet on this coast. The inlet is stabilized by two parallel rubble stone jetties (Beck and Kraus 2010). This case is useful for testing the developed model's hydrodynamic and morphologic capabilities for an inlet with a relatively small bay with dual-jetties entrance. Water

level data from Belmar, NJ, a site within Shark River Estuary (Fig. 5.14), were compared to model calculations for a 10-day period from August 15-25, 2009. The measurement of morphology change over a 4-month period from January to April 2009 was also available to compare the calculated results.

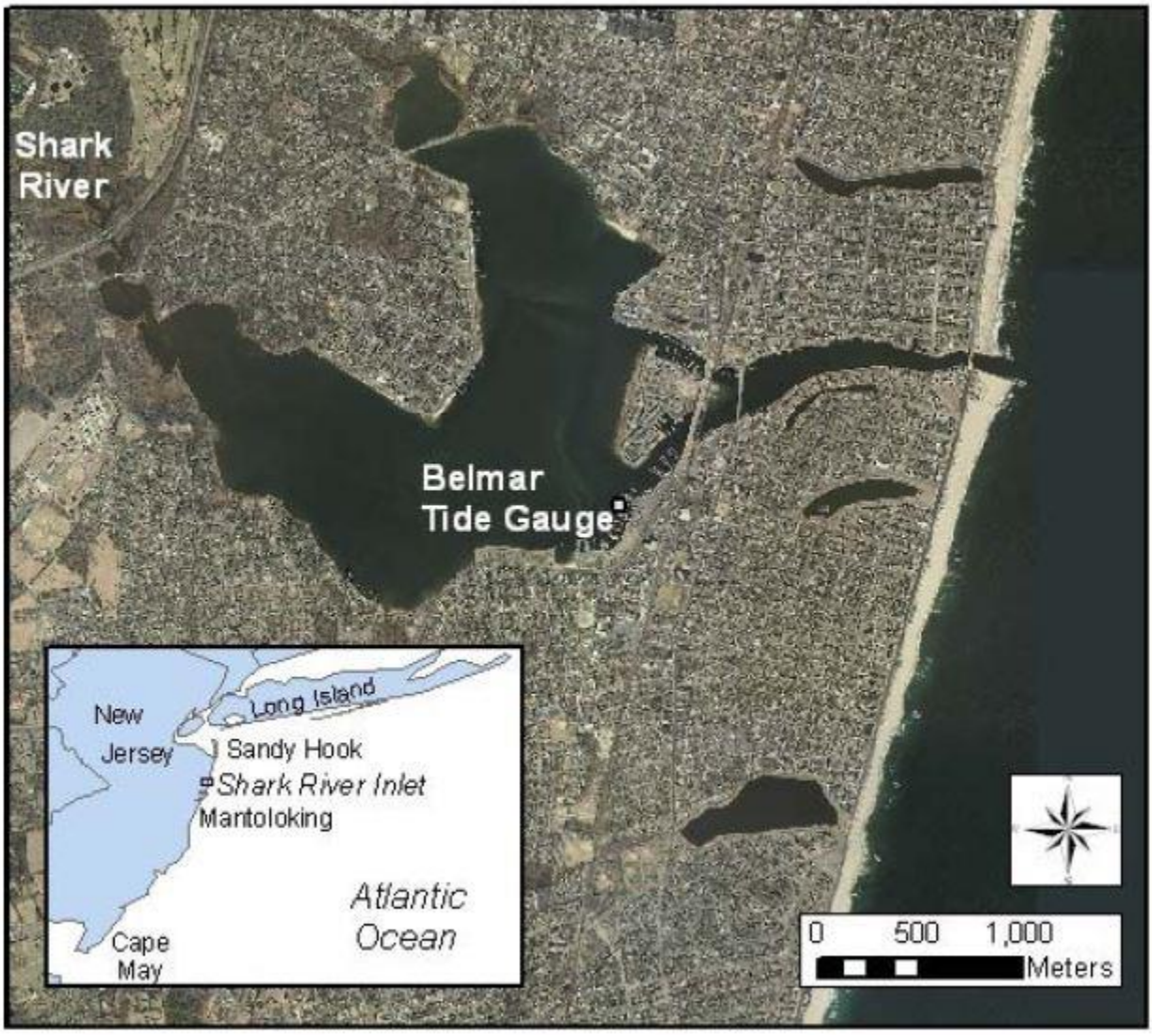

Figure 5.15 Location Map for Shark River Inlet, NJ

The model domain covered a local scale of approximately 11 km centrally located around Shark River Inlet. A telescoping grid was used. The smallest 8-m cell size was used within the main throat of the inlet and the largest 128-m cell size was used in the ocean. The cell size around the groins and beach was 16 m. The total of active ocean cells was approximately 20,000 (Fig. 5.16). In the vertical (z-) direction, 6 layers were used.

Bathymetry needed to develop the model grid for the backbay, entrance channel, and ocean was assembled from several datasets and converted to mean sea level (MSL) as given by the local tidal datum for Long Branch, NJ. Water level from a tidal gage at Sandy Hook, NJ was applied at the open ocean boundary. Wave data from Wave Information Study station 129 provided input parameters for generating spectral waves for CMS-Wave. The initial bed composition was defined by assuming an initial log-normal grain size distribution, and specifying an initial geometric standard deviation σ_g = 1.8 mm and median grain size d_{50} = 0.26 mm (Sanchez et al. 2011). Five size classes are used to represent the sediment mixture. The Manning's coefficient was modified at discrete locations of the grid, ranging from 0.02 to 0.06 $s/m^{1/3}$. For example, larger Manning's coefficient was used around the structures to increase the friction. Non-erodible hard bottom cells are specified around the two jetties where structure protection is imposed at the field. A time step of 30 minutes is used. The steering interval between flow and wave models is 3 hour.

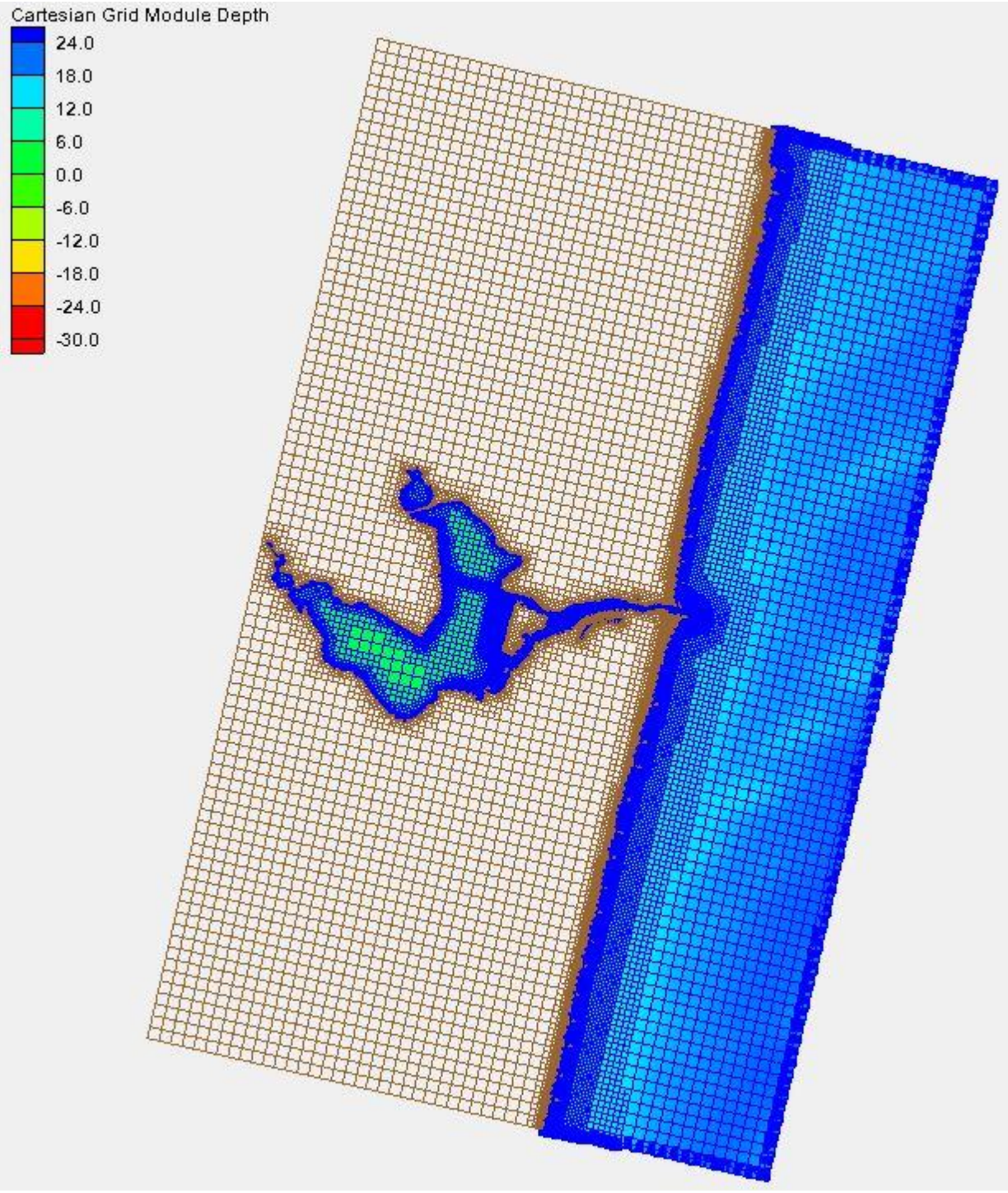

Figure 5.16 Computational Mesh for the Shark River Inlet Case

Fig. 5.17 shows the measured and calculated water levels at Belmar tidal gage from August 15–25, 2009. The model reproduces well the measured tidal level. Fig. 5.18 shows a comparison of measured and calculated morphology changes in the inlet after 4-month simulation. The model provides a generally good agreement of deposition patterns within the inlet channel. The morphological change around the jetties is zero due to the specified non-erodible hard bottom cells. Fig.5.19 shows the d_{50} of the bed material after 4-month simulation. The coarse sediment is transported towards the shore. Figs. 5.20-5.24 compare the measured and calculated bathymetry across five transects after the 4-month simulation period. The locations of the five transects are shown in Fig. 5.18. Transects 1 and 2 represent the along channel sedimentation patterns in the direction of currents. Both transects extend from the bridge pilings eastward toward the ocean. The model reproduced well the trend of deposition and erosion in in these two transects. Transect 3 is located within the jettied part of the channel. The model illustrated a good agreement between the measured and calculated deposition in the center of the channel. The model generally captured the channel infilling at the location of greatest change in Transect 4. Calculated and measured morphology changes in transect 5 are very closed and resulted in a good agreement.

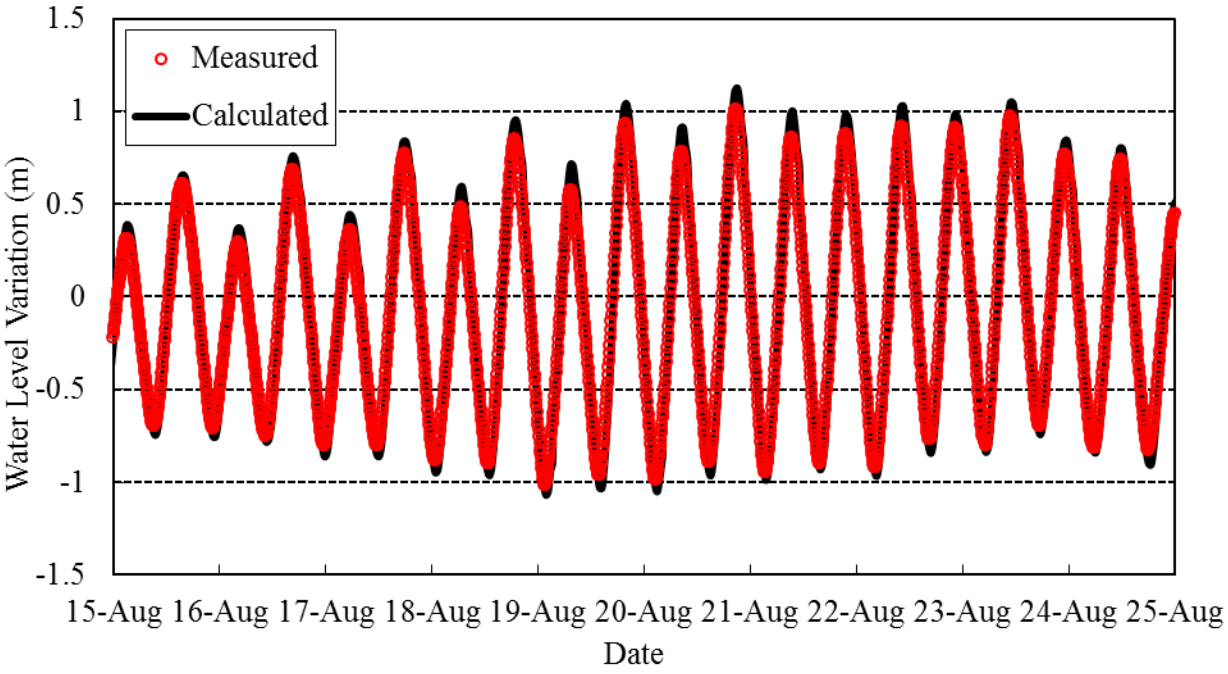

Figure 5.17 Comparison of Measured and Calculated Water Level at Belmar

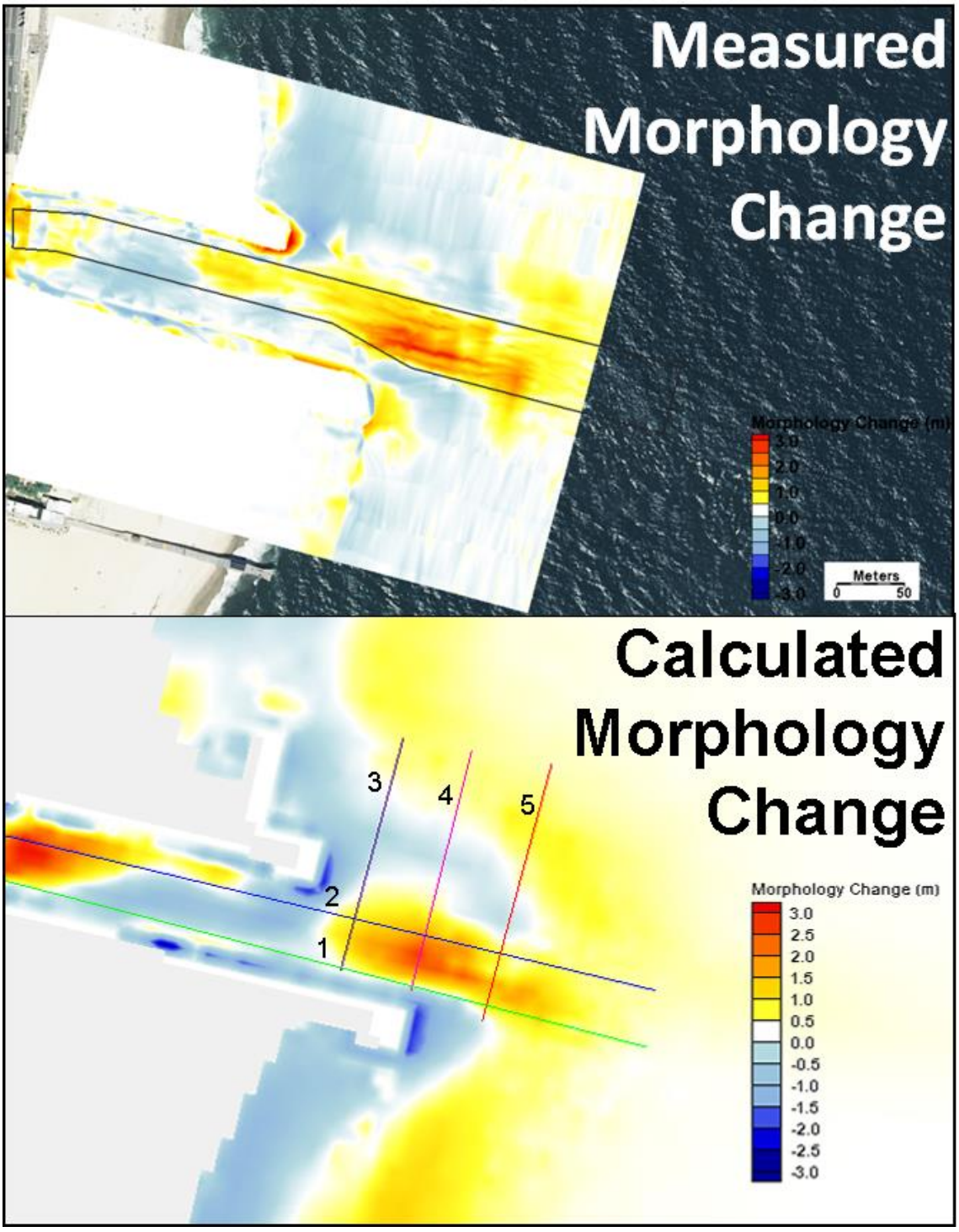

Figure 5.18 Measured (top) and Calculated (bottom) Morphology Change for a 4-month Period (January-April 2009) at Shark River Inlet, FL.

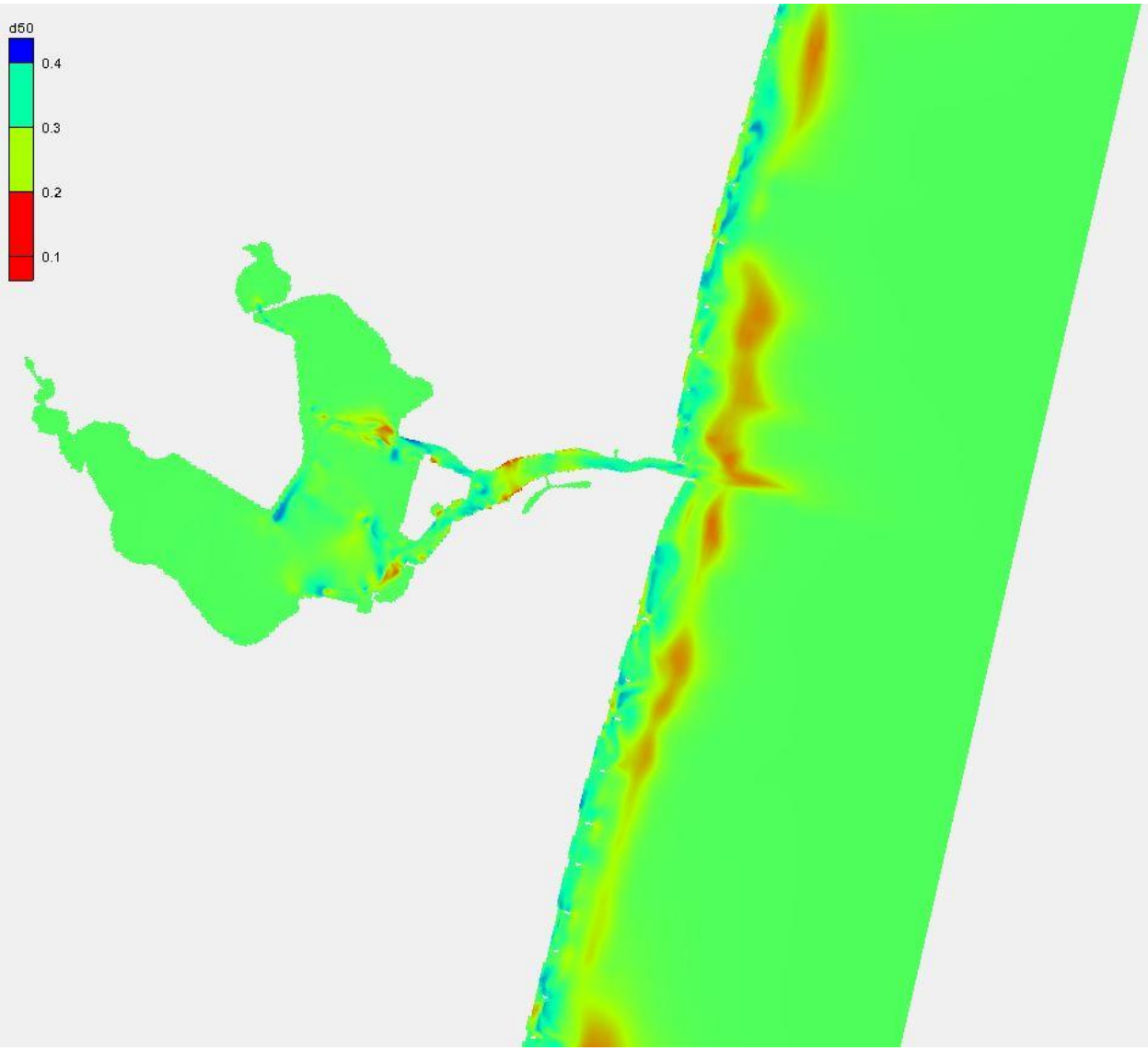

Figure 5.19 Calculated d_{50} of the bed material after a 4-month Period (January-April 2009) at Shark River Inlet, FL.

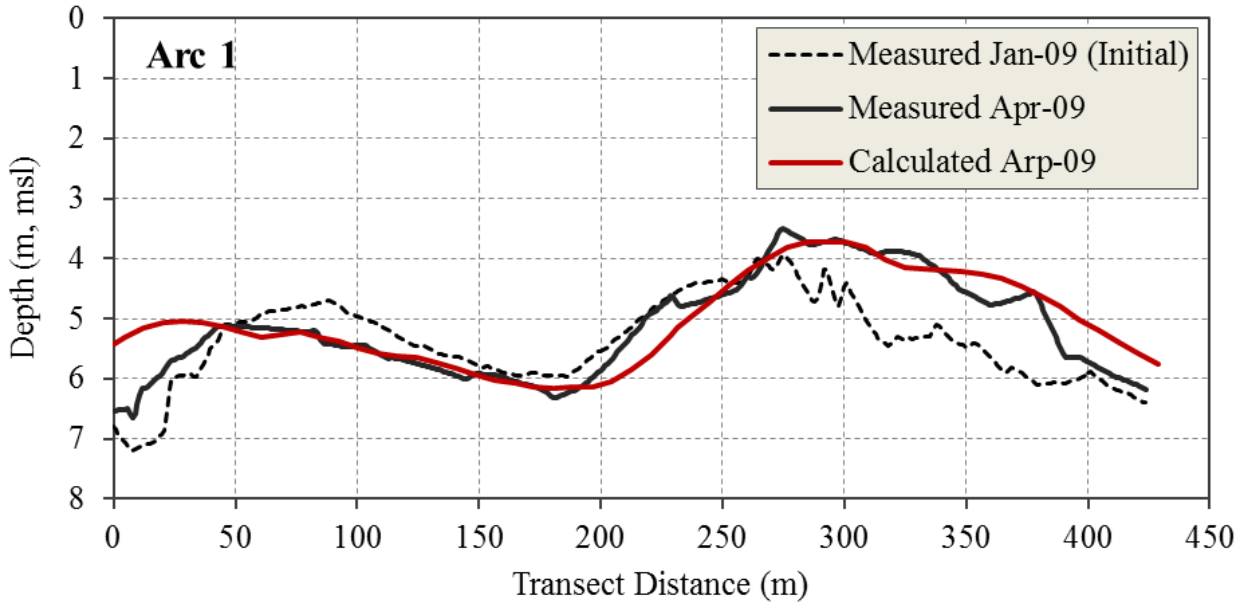

Figure 5.20 Measured and Calculated Bathymetry across Arc 1 (transect). Distance is Measured from West to East.

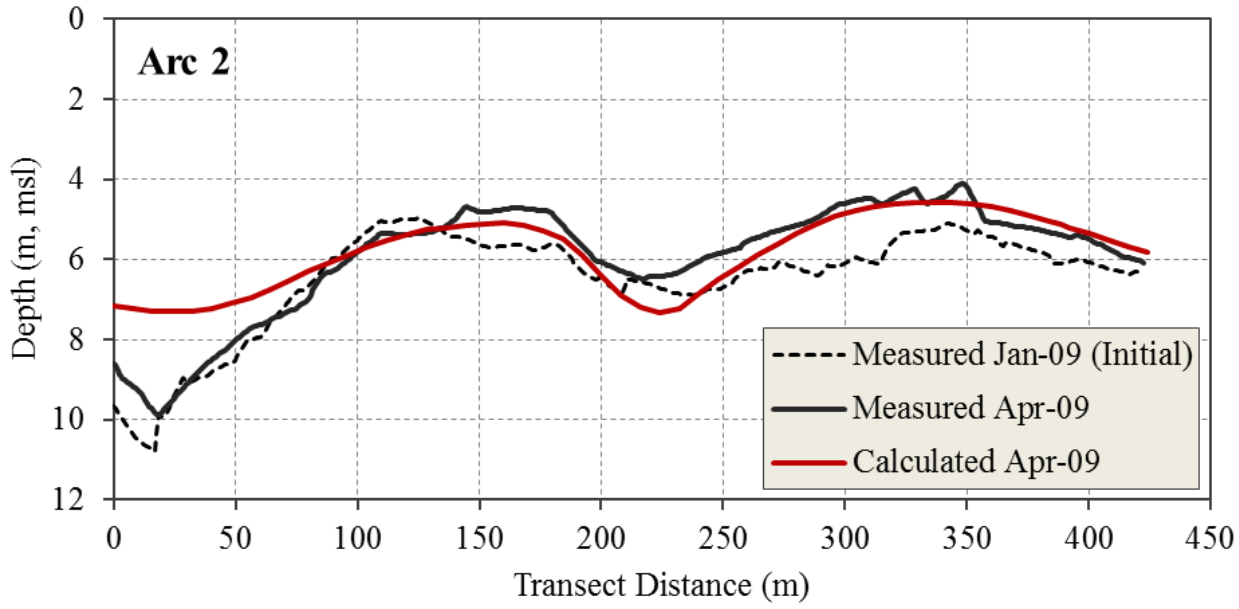

Figure 5.21 Measured and Calculated Bathymetry across Arc 2 (transect). Distance is Measured from West to East.

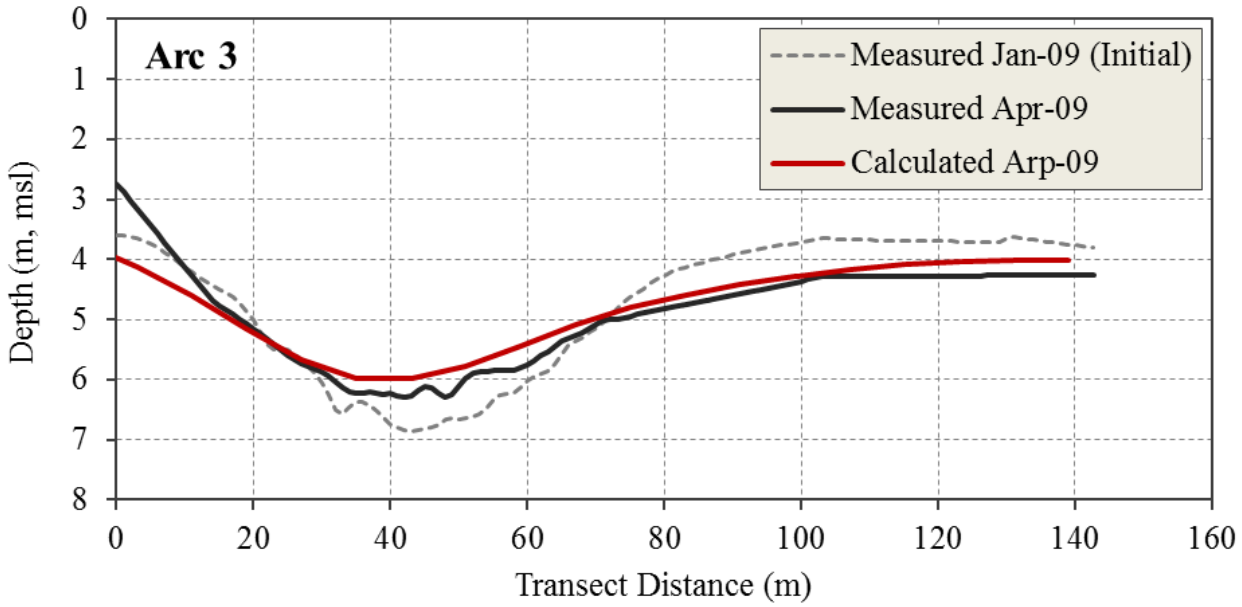

Figure 5.22 Measured and Calculated Bathymetry across Arc 3 (transect). Distance is Measured from South to North.

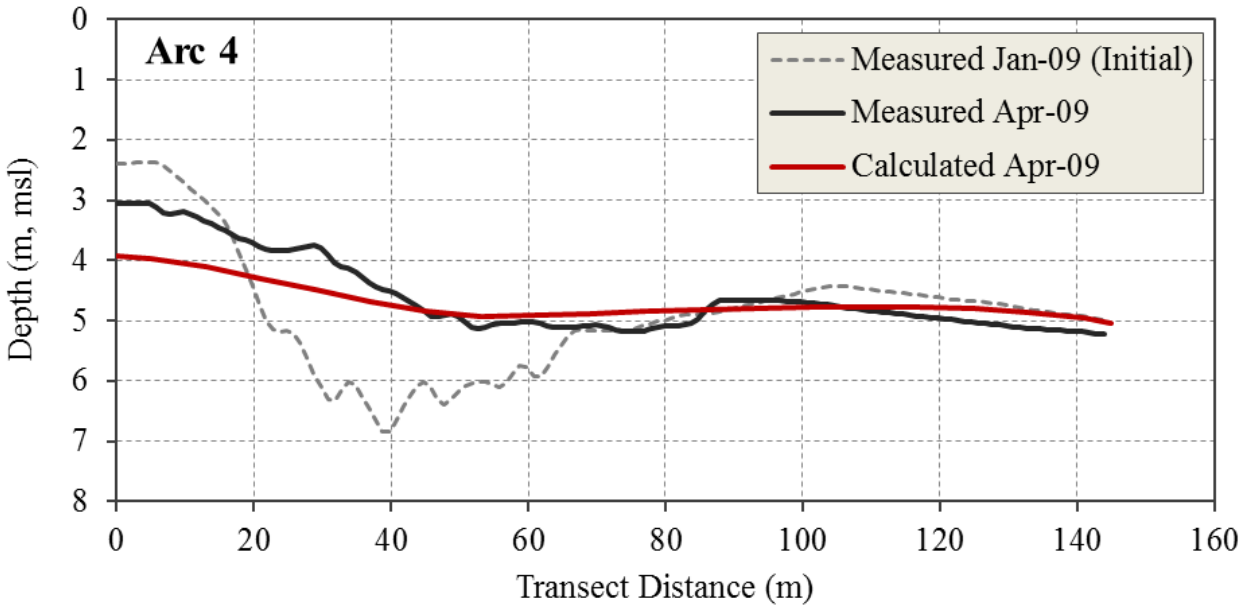

Figure 5.23 Measured and Calculated Bathymetry across Arc 4 (transect). Distance is Measured from South to North.

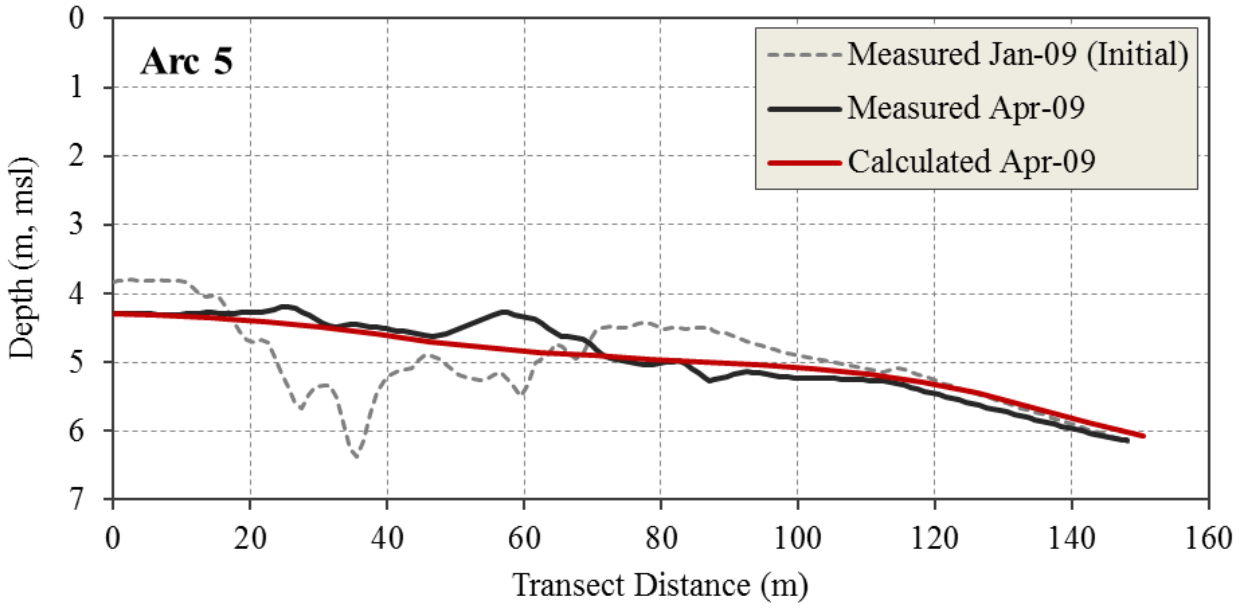

Figure 5.24 Measured and Calculated Bathymetry across Arc 5 (transect). Distance is Measured from South to North.

CHAPTER VI

CONCLUSIONS

A three-dimensional numerical model of multiple-sized sediment transport under current and waves has been developed. The hydrodynamic model simulates the current induced by short waves in coastal water by adopting the three-dimensional phase-averaged shallow water flow equations coupled with wave radiation stresses. The sediment transport model simulates the sediment transport processes under current and waves by solving the nonequilibrium sediment transport equations with a finite volume method.

In order to close the developed 3-D sediment transport model, the Wu et al. (2000b) bed-load and suspended-load formulas have been extended to multiple-sized sediment transport under non-breaking waves and currents for coastal applications. Methods have been developed to determine the bed shear stress due to waves only and combined current and waves, and in turn applied to compute the bed-load and suspended-load transport rates. The developed formulas have been tested by a large number of data, which include single- or multiplied-sized bed-load and suspended-load under current and waves. Statistics show that more than 50% of the cases are predicted within a factor of 2 of the measured values and more than 75% of the cases are within a factor of 5.

A new formula to predict the near-bed suspended-load concentration under current and waves has also been established. Different methods in literature have been tested and chosen to

determine the edge of the bed-load layer, i.e., reference level. In the presence of waves, van Rijn's (1993) two-layer logarithmic distribution is used to predict the velocity profile. The distribution of Williams et al. (1999) is used to represent the concentration profile since it was validated by its developers using measured data under combined waves and currents. Two new approaches have been also developed to determine the Schmidt number. Analysis shows the new approaches are good choices to estimate the Schmidt number, while one may assume a unit Schmidt number for simplicity. The developed formula has been tested by using sediment data under current only and combined current and waves. Statistics shows more than half of the test cases are predicted within a factor of 2 of the measured values and about 90% of the cases are within a factor of 5.

The extended Wu et al. (2000b) formulas and the new near-bed suspended-load concentration formula have been compared with other existing formulas in literature. The comparisons have been demonstrated that the developed formulas have better reliability and performance under different conditions over other formulas.

The adopted hydrodynamic model is coupled with a spectral wave deformation model, which solves the spectral wave-action balance equation and provides wave characteristics to the flow model. The developed flow model uses the multiple-level quadtree rectangular mesh on the horizontal plane and the sigma coordinate in the vertical direction. The SIMPLEC algorithm is used to couple the flow velocity and water level. The developed model has been tested by four cases: tidal flow in San Francisco Bay, tidal flow in Gironde Estuary, wind-induced current in a flume, and undertow flow induced by waves on a slopped beach. The first two cases are tidal flows in estuaries, through which the stability, efficiency and reliability of the model for unsteady flows have been quantitatively validated. The wind-induced current case has shown the validity of

mixing length model in simulating the wind-induced velocity profile. The undertow flow case has validated the coupling of the wave and flow models. The flow model has demonstrated its reliability and reasonable prediction through these four test cases.

In the sediment transport model, the suspended-load transport equation is solved using the same finite volume method as the flow model. A coupled solution procedure is implemented to solve the multiple-sized sediment transport, bed change and bed material sorting equations together. The developed sediment transport model has been validated by four test cases: erosion in a basin due to clear water inflow, channel infilling and migration with waves parallel to flow, channel infilling and migration with waves perpendicular to flow, and tidal flow and channel infilling at Shark River Inlet, NJ. In these test cases, sensitivity analyses have been conducted for the bed friction coefficient, suspended-load scale factor, Schmidt Number, bed-load adaptation length, and roughness height constant. It has been shown that the model is somehow sensitive to the bed friction coefficient, suspended-load scale factor, Schmidt number, and roughness height constant. The model is not sensitive to bed-load adaptation length in the test case where the suspended load is dominant. The developed model has been demonstrated its capability of predicting morphologic behavior through the test cases.

Overall, the developed model has been validated using a variety of measurement data in experimental and field cases, showing the predictions are in generally good agreements with the measurements. In the future, the developed model will be enhanced to consider cohesive sediment transport in coastal and estuarine waters, which has also gained attention from scientists and engineers.

BIBLIOGRAPHY

BIBLIOGRAPHY

Abou-Seida, M. M. (1965). *Bed Load Function Due to Wave Action* (Technical Report No. HEL-2-11). Berkeley, CA: Hydraulics Engineering Laboratory, University of California, Berkeley.

Ahilan, R. V., & Sleath, J. F. A. (1987). Sediment Transport in Oscillatory Flow Over Flat Beds. *Journal of Hydraulic Engineering*, *113*(3), 308–321.

Ahmed, A. S. M. (2002). *Sheet flow transport mechanism of heterogeneous sediments under nonlinear oscillatory flows* (Ph.D. Dissertation). Department of Civil Engineering, University of Tokyo, Tokyo, Japan.

Ahmed, A. S. M., & Sato, S. (2003). A Sheetflow Transport Model for Asymmetric Oscillatory Flows: Part II: Mixed Grain Size Sediments. *Coastal Engineering Journal*, *45*(03), 339–361.

Andersen, O. H., Hedegaard, I. B., Degarrd, R., Girolamo, P., & Madsen, P. (1988). Model for morphological changes under waves and current. *Proc. IAHR symposium on Math. Modeling of Sediment Transport in the Coastal Zone*. Copenhagen, Denmark.

Ariathurai, C. R. (1974). *A finite element model for sediment transport in estuaries* (Ph.D. Dissertation). University of California, Davis, CA.

Armanini, A., & Di Silvio, G. (1988). A one-dimensional model for the transport of a sediment mixture in non-equilibrium conditions. *Journal of Hydraulic Research*, *26*(3), 275–292.

Bagnold, R. A. (1963). *Mechanics of marine sedimentation* (Vol. 3). New York: Wiley-Interscience.

Bagnold, R. A. (1966). *An approach to the sediment transport problem from general physics* (Professional Paper No. 422-J) (p. 37). Washington D.C., USA: USGS.

Bailard, J. A. (1981). An Energetics Total Load Sediment Transport Model For a Plane Sloping Beach. *Journal of Geophysical Research*, *86*(C11), 10938–10,954.

Bailard, J. A., & Inman, D. L. (1981). An Energetics Bedload Model for a Plane Sloping Beach:Local Transport. *Journal of Geophysical Research*, *86*(C3), 2035–2043.

Baines W. D. & Knapp D. J. (1965). Wind driven water currents. *Journal of the Hydraulic Division*, ASCE, 9(4), 343–358.

Beck, T. M., & N. C. Kraus. (2010). *Shark River Inlet, New Jersey, Entrance Shoaling: Report 2, Analysis with Coastal Modeling System.* Technical Report ERDC/CHL-TR-10-4. U.S. Army Engineer Research and Development Center, Coastal and Hydraulics Laboratory, Vicksburg, MS.

Bijker, E. W. (1968). LITTORAL DRIFT AS FUNCTION OF WAVES AND CURRENT. *Proceedings of the International Conference on Coastal Engineering*, *1*(11).

Bosman, J. (1982). *Concentration distribution under waves and current*. Technical Report No. M1875. The Netherlands: Coastal Engineering Department, Delft University of Technology, Delft.

Bridge, J. S., & Dominic, D. F. (1984). Bed Load Grain Velocities and Sediment Transport Rates. *Water Resources Research*, *20*(4), 476–490. doi:10.1029/WR020i004p00476

Brownlie, W. R. (1981). *Compilation of alluvial channel data : Laboratory and field* (No. KH-R-43B). Pasadena, California: W. M. Keck Lab. of Hydr. and Water Resources, California Institute of Technology.

Brush, L. M., Ho, H. W., & Singamsetti, S. R. (1962). *A study of sediment in suspension*. Pub. No. 59. Inter. Assoc. Sci. Hydraul., Commiss. Land Erosion.

Buttolph, A. ., Reed, C. W., Kraus, N. C., Ono, N., Larson, M., Carmenen, B., Hanson, H., et al. (2006). *Two-dimensional depth-averaged circulation model CMS-M2D: Version 3.0, Report 2: Sediment transport and morphology change* (Technical Report No. ERDC/CHL TR-06-9). Vicksburg, MS: Coastal and Hydraulics Laboratory, ERDC, US Army Corps of Engineers.

Camenen, B. (2002). *Modélisation numérique du transport sédimentaire sur une plage sableuse*. Universite Joseph Fourier, Grenoble, France.

Camenen, B., & Larson, M. (2007). *A Unified Sediment Transport Formulation for Coastal Inlet Application* (No. ERDC/CHL-CR-07-1). Vicksburg, Mississippi: US Army Engineer Research and Development Center, Coastal and Hydraulics Laboratory.

Cayocca, F. (2001). Long-term morphological modeling of a tidal inlet: the Arcachon Basin, France. *Coastal Engineering*, *42*(2), 115–142.

Саткевич, А.А. (1934). Теоретические основи гидроаэродинамики, Т. 2, Динамика жидких тел.

Chapman, R. S., Johnson, B. H., & Vemulakonda, S. R. (1996). *User's Guide for the Sigma Stretched Version of CH3D-WES - A Three-Dimensional Numerical Hydrodynamic, Salinity, and Temperature Model* (Technical Report No. HL-96-21). Vicksburg, MS: US Army Engineer Waterways Experiment Station.

Chassignet, E. P., Arango, H., Dietrich, D., Ezer, T., Ghil, M., Haidvogel, D. B., Ma, C.-C., et al. (2000). DAMÉE-NAB: the base experiments. *Dynamics of Atmospheres and Oceans*, *32*(3–4), 155–183.

Chen, C., Liu, H., & Beardsley, R. C. (2003). An Unstructured Grid, Finite-Volume, Three-Dimensional, Primitive Equations Ocean Model: Application to Coastal Ocean and Estuaries. *Journal of Atmospheric and Oceanic Technology*, *20*(1), 159–186.

Chesher, T. J., & Great Britain. Ministry of Agriculture, F. and F. (1993). *PISCES : a morphodynamic coastal area model : first annual report*. Wallingford, Oxfordshire: HR Wallingford Ltd.

Chiu, C. L. (1967). Stochastic Model of Motion of Solid Particles. *Journal of the Hydraulics Division*, *93*(5), 203–218.

Cloin, B. (1998). *Gradation effects on sediment transport in oscillatory sheet flow* (M.Sc. Thesis). Delft University of Technology, The Netherlands.

Cookman, J. L., & Flemings, P. B. (2001). STORMSED1.0: hydrodynamics and sediment transport in a 2-D, steady-state, wind- and wave-driven coastal circulation model. *Computers & Geosciences*, *27*(6), 647–674.

Danish Hydraulic Institute. (2007a). *MIKE 21 flow model hydrodynamic module user guide*.

Danish Hydraulic Institute. (2007b). *MIKE 3 - 3D modelling of coast and sea user guide*.

Day, T. J. (1980). *A Study of the Transport of Graded Sediments*. Hydraulics Research Station.

de Meijer, R. ., Bosboom, J., Cloin, B., Katopodi, I., Kitou, N., Koomans, R. ., & Manso, F. (2002). Gradation effects in sediment transport. *Coastal Engineering*, *47*(2), 179–210.

Delft Hydraulics. (2010). *Delft3D-FLOW: Simulation of multi-dimensional hydrodynamic flows and transport phenomena, including sediment.* User Manual. The Netherlands.

Dibajnia, M., & Watanabe, A. (1992). Sheet flow under nonlinear waves and currents. *Proceedings of the International Conference on Coastal Engineering* (Vol. 1, pp. 2,015–2,029). ASCE.

Dibajnia, M., & Watanabe, A. (1996). A transport rate formula for mixed sands. *Proc. 25th Coastal Engineering Conference*, ASCE, Orlando, USA, 3791–3804.

Dibajnia, M., & Watanabe, A. (2000). Moving Layer Thickness and Transport Rate of Graded Sand. *Proc., 27th ICCE* (pp. 2752–2765). Sydney, Australia: American Society of Civil Engineers.

Ding, Y., Wang, S. S. Y., & Jia, Y. (2004). Development and validation of nearshore morphodynamic area model in coastal zone, In: *Advances in Hydro-Science and -Engineering*, Vol.VI.

Dohmen-Janssen, C.M. (1999). *Grain size influence on sediment transport in oscillatory sheet flow, phase-lags and mobile-bed effects* (Ph.D. Dissertation). Delft University of Technology, Delft, The Netherlands.

Dohmen-Janssen, C. Marjolein, & Hanes, D. M. (2002). Sheet flow dynamics under monochromatic nonbreaking waves. *Journal of Geophysical Research*, *107*(10).

Dou, G. R. (1964). *Bed-load transport*. China: Nanjing Hydraulic Research Institute.

Egiazaroff, I. V. (1965). Calculation of Nonuniform Sediment Concentrations. *Journal of the Hydraulics Division*, *91*(4), 225–247.

Einstein, H.A. (1942). Formulas for the transportation of bed load. *Trans.*, ASCE, *107*, 561–573.

Einstein, H.A. (1950). *The bed-load function for sediment transportation in open channel flows*. Technical Bulletin No. 1026, U.S. Department of Agriculture, Soil Conservation Service, Washington D.C., USA.

Einstein, Hans Albert, & Chien, N. (1954). *Second Approximation to the Solution of the Suspended Load Theory: By H. A. Einstein and Ning Chien*. U.S. Army Engineer Division, Missouri River.

Exner, F. M. (1925). Uber die Wechselwirkung zwischen Wasser und Geschiebe in Flüssen. *Sitzungsberichte. Abt. 2a, Mathematik, Astronomie, Physik und Meteorologie (Akademie der Wissenschaften in Wien, Mathematisch-Naturwissenschaftliche Klasse).*

Fortunato, A. B., & Oliveira, A. (2004). A modeling system for tidally driven long-term morphodynamics. *Journal of Hydraulic Research*, *42*(4), 426–434.

Froehlich, D. C. (1989). *Finite Element Surface-Water Modeling System: Two-Dimensional Flow in a Horizontal Plane—Users Manual* (No. FHWA-RD-88-177). Federal Highway Administration.

Garcia, M., & Parker, G. (1991). Entrainment of Bed Sediment into Suspension. *Journal of Hydraulic Engineering*, *117*(4), 414–435.

Grasmeijer, B., & Sistermans, R. (1995). *Sediment concentrations and transport in case of irregular breaking waves, Part H and I*. The Netherlands: Department of Coastal Engineering, Delft University of Technology, Delft.

Haidvogel, D. B., Arango, H. G., Hedstrom, K., Beckmann, A., Malanotte-Rizzoli, P., & Shchepetkin, A. F. (2000). Model evaluation experiments in the North Atlantic Basin: simulations in nonlinear terrain-following coordinates. *Dynamics of Atmospheres and Oceans*, *32*(3–4), 239–281.

Hassan, W. N. M., Kroekenstoel, D. F., Ribberink, J. S., & van Rijn, L. C. (2001). *Gradation effects on sand transport under oscillatory sheet-flow conditions* (Research Report). The Netherlands: Delft Hydraulics/University of Twente, Delft/Enschede.

Hassan, W. N., & Ribberink, J. S. (2005). Transport processes of uniform and mixed sands in oscillatory sheet flow. *Coastal Engineering*, *52*(9), 745–770.

Havinga, F. J. (1992). *Sediment concentrations and sediment transport in case of irregular non-breaking waves with a current* (Technical Report). The Netherlands: Coastal Engineering Department, Delft University of Technology, Delft.

Hayter, E. J., & Mehta, A. J. (1986). Modelling cohesive sediment transport in estuarial waters. *Applied Mathematical Modelling*, *10*(4), 294–303.

Hirano, M. (1971). River bed degradation with armoring. *Trans.*, JSCE, *3*(2), 55–65.

Holland, K. T., & Elmore, P. A. (2008). A review of heterogeneous sediments in coastal environments. *Earth-Science Reviews*, *89*(3–4), 116–134.

Horikawa, K., Watanbe, A., & Katori, S. (1982). Sediment Transport under Sheet Flow Condition (pp. 1335–1352). Presented at the *Coastal Engineering* (1982), ASCE.

Hsu, S.A. (1988). *Coastal meteorology*. Academic Press, San Diego, California.

Hydroqual. (2002). *A primer for ECOMSED. Version 1.3.* Users Manual.

Inui, T., Dibajnia, M., Isobe, M., & Watanabe, A. (1995). A transport rate formula for mixed-size sands and its application. *Proc. 42nd Japanese Annual Conf. on Coastal Eng.* (pp. 521–525). JSCE.

Jacobs, C., & Dekker, S. (2000). *Sediment concentrations due to currents and irregular waves: The effect of grading of the bed material* (Measurements Report). The Netherlands: Delft

University of Technology, Delft.

Jonsson, I. G. (1966). WAVE BOUNDARY LAYERS AMD FRICTION FACTORS. *Proceedings of the International Conference on Coastal Engineering*, *1*(10).

Kalkanis, G. (1964). *Transportation of bed material due to wave action*.

Karim, F., & Kennedy, J. F. (1982). *IALLUVIAL: A computer-based flow- and sediment- routing model for alluvial streams and its application to the Missouri river* (Technical Report No. 250). University of Iowa, USA: IIHR.

Katopodi, I., Ribberink, J. S., Ruol, P., Koelewijn, R., Lodahl, C., Longo, S., Crosato, A., et al. (1994). *Intra-wave sediment transport in an oscillatory flow superimposed on a mean current* (Data report No. H1684,Part III). The Netherlands: Delft Hydraulics, Delft.

King, D. B. J. (1991). *Studies in oscillatory flow bed load sediment transport* (Ph.D. Dissertation). University of California, San Diego, CA.

Letter, J. V., Roig, L. C., Donnell, B. P., Thomas, W. A., Mcanally, W. H., Adamec, S. A., & Sedd-wes, J. (1998). *Users Manual for SED2D-WES Version 4.3 Beta, A Generalized Computer Program for Two-dimensional, Vertically Averaged Sediment Transport*. Vicksburg, MS: US Army Corps of Engineers Waterways Experiment Station Coastal Hydraulics Laboratory.

Li, Z. H., Nguyen, K. D., Brun-Cottan, J.-C., & Martin, J.-M. (1994). Numerical simulation of the turbidity maximum transport in the Gironde estuary (France). *Oceanologica acta*, *17*(5), 479–500.

Lin, L., Demirbilek, Z., Mase, H., Zheng, J., & Yamada, F. (2008). *CMS-Wave: A nearshore spectral wave processes model for coastal inlets and navigation projects* (No. ERDC/CHL TR-08-13). Vicksburg, MS: Coastal and Hydraulics Laboratory, ERDC, US Army Corps of Engineers.

Longuet-Higgins, M. S., & Stewart, R. w. (1964). Radiation stresses in water waves; a physical discussion, with applications. *Deep Sea Research and Oceanographic Abstracts*, *11*(4), 529–562.

Lundgren, H. (1972). Turbulent currents in the presence of waves. *Proceedings of 13th International Conference on Coastal Engineering*, ASCE, NewYork, 623–634.

Madsen, O. S. (1991). *Simple models for turbulent wave-current bottomboundary layer flow*. Dredging Research Program, Final Rep. Washington, D.C.

Majumdar, H., & Carstens, M. R. (1967). *Diffusion of particles by turbulence : effect of particle*

size. Atlanta: School of Civil Engineering in cooperation with Water Resources Center, Georgia Institute of Technology.

Majumdar, S. (1988). Role of underrelaxation in employing momentum interpolation practice for calculation of flow with non-staggered grids. *Num. Heat Transfer*, 13, 125–132.

Mase, H. (2001). MULTI-DIRECTIONAL RANDOM WAVE TRANSFORMATION MODEL BASED ON ENERGY BALANCE EQUATION. *Coastal Engineering Journal*, *43*(04), 317–337.

Mase, H., Oki, K., Hedges, T. S., & Li, H. J. (2005). Extended energy-balance-equation wave model for multidirectional random wave transformation. *Ocean Engineering*, *32*(8–9), 961–985.

Matyukhin, V. J., & Prokofyev, O. N. (1996). Experimental determination of the coefficient of vertical turbulent diffusion in water for settling particles. *Soviet Hydrol, 3*.

Mellor, G. (2003). The Three-Dimensional Current and Surface Wave Equations. *Journal of Physical Oceanography*, *33*(9), 1978–1989.

Mellor, G. (2005). Some consequences of the three-dimensional current and surface wave equations. *Journal of physical oceanography*, *35*(11), 2291–2298.

Mellor, G. (2008). The depth-dependent current and wave interaction equations: a revision. *Journal of Physical Oceanography*, 38, 2587–2596.

Meyer-Peter, E., & Muller, R. (1948). *Formulas for bed-load transport*. Stockholm: IAHSR 2nd meeting.

Nielsen, P. (1984). Field measurements of time-averaged suspended sediment concentrations under waves. *Coastal Engineering*, *8*(1), 51–72.

Nielsen, P. (1992). *Coastal Bottom Boundary Layers and Sediment Transport*. World Scientific.

Nikuradse, J. (1933). *Stromungsgesetze in rauhen Rohrne* (*Laws of flow in rough pipes*). Berlin, Ver. deutscher Ingenieure, Forschungsheft, no. 361.

Nieuwjaar, M., & Kaaij, T. V. D. (1987). *Sediment concentrations and sediment transport in case of irregular non-breaking waves with a current*. The Netherlands: Department of Civil Engineering, Delft University of Technology, Delft.

O'Connor, B. A., & Nicholson, J. (1988). A three-dimensional model of suspended particulate sediment transport. *Coastal Engineering*, *12*(2), 157–174.

O'Donoghue, T., & Wright, S. (2004). Flow tunnel measurements of velocities and sand flux in oscillatory sheet flow for well-sorted and graded sands. *Coastal Engineering*, *51*(11–12),

Olsen, N. R. B. (2003). Three-Dimensional CFD Modeling of Self-Forming Meandering Channel. *J. Hydraul. Eng.*, 129(5), 366–372.

Patankar, S. (1980). *Numerical Heat Transfer and Fluid Flow*. Taylor & Francis.

Patel, P. ., & Ranga Raju, K. G. (1996). Fractionwise calculation of bed load transport. *Journal of Hydraulic Research*, *34*(3), 363–379.

Prandtl, L. (1925). Über die ausgebildete Turbulenz, *ZAMM*, 5, p. 136.

Powell, M.D., Vickery, P.J., and Reinhold, T.A. (2003). Reduced drag coefficient for high wind speeds in tropical cyclones, *Nature*, 422, 279–283.

Rahuel, J. L., Holly, F. M., Chollet, J. P., Belleudy, P. J., & Yang, G. (1989). Modeling of Riverbed Evolution for Bedload Sediment Mixtures. *Journal of Hydraulic Engineering*, *115*(11), 1521–1542.

Ramadan, K. A. H. (1994). *Time-averaged sediment transport phenomena in combined wave-current flows, Part I* (No. Report H1889.11). The Netherlands: Delft Hydraulics, Delft.

Ranasinghe, R., Pattiaratchi, C., & Masselink, G. (1999). A morphodynamic model to simulate the seasonal closure of tidal inlets. *Coastal Engineering*, *37*(1), 1–36.

Raudkivi, A. J. (2006). Transition from Ripples to Dunes. *Journal of Hydraulic Engineering*, *132*(12), 1316–1320.

Rhie, C. M., & Chow, W. L. (1983). Numerical study of the turbulent flow past an airfoil with trailing edge separation. *AIAA Journal*, *21*(11), 1525–1532.

Ribberink, J.S., & Chen, Z. (1993). *Sediment transport of fine sand under asymmetric oscillatory flow* (No. Report H840 (Part VII)). The Netherlands: Delft Hydraulics, Delft.

Ribberink, J. S., & Al-Salem, A. A. (1994). Sediment transport in oscillatory boundary layers in cases of rippled beds and sheet flow. *Journal of Geophysical Research*, *99*(C6), 12707–12,727.

Ribberink, J.S. (1995). *Time-averaged sediment transport phenomena in combined wave-current flows, Part II* (No. Report H1889.11). The Netherlands: Delft Hydraulics, Delft.

Ribberink, J. S. (1998). Bed-load transport for steady flows and unsteady oscillatory flows. *Coastal Engineering*, *34*(1–2), 59–82.

Ribberink, J.S., Blom, A., & van der Sheer, P. (2002). Multi-fraction techniques for sediment transport and morphological modeling in sand-gravel rivers (pp. 731–739). Presented at the *River Flow 2002, Bousmar and Zech* (eds.), Swets & Zeitinger, Lisse.

Roelvink, J. A. (1987). *Large scale investigation of cross-shore sediment transport* (No. H596). The Netherlands: Delft Hydraulics, Delft.

Roelvink, J. A., & Banning, G. V. (1994). Design and development of DELFT3D and application to coastal morphodynamics. *Hydroinformatics 94 Proc 1st international conference* (pp. 451–455). Balkema, Rotterdam.

Rouse, H. (1937). Modern conceptions of the mechanics of turbulence. *Trans.*, ASCE, 102, 463–543.

Sánchez, A., & Wu, W. (2011). A non-equilibrium sediment transport model for coastal inlets and navigation channels. *Journal of Coastal Research*, Special Issue 59, 39–48.

Sánchez, A., Wu, W., Beck, T.M., Li, H.,Rosati, J.D., Demirbilek, Z., and Brown, M. (2011). *Verification and Validation of the Coastal Modeling System, Report 4, CMS-Flow: Sediment Transport and Morphology Change*. ERDC/CHL TR-11-10. Coastal and Hydraulics Laboratory, U.S. Army Engineer Research and Development Center

Sanchez, A. (2013). *An implicit finite-volume depth-integrated model for coastal hydrodynamics and multiple-sized sediment transport*, PhD Dissertation, The University of Mississippi, USA.

Sawamoto, M., & Yamashita, T. (1986). Sediment transport rate due to wave action. *Journal of Hydroscience and Hydraulic Engineering*, *4*(1), 1–15.

Shamov, G. I. (1959). *Recnie Nanosy*. Gidrometeoroizdat, Leningrad.

SEDMOC. (1999). *SEDMOC data base TAP, Instruction Manual*. Delft Hydraulics/Delft University of Technology.

Sheng, Y. P., & Butler, H. L. (1982). Modeling oastal urrents and sediment transport. *Proceedings of the International Conference on Coastal Engineering*, *1*(18).

Sheng, Y.P., & Alymov, V. (2002). *Coastal Flooding Analysis of Pinellas County Using ALSM Data: A Comparison between UF's 2-D Method and Results vs. FEMA's Method and Results* (No. 67). Gainesville, FL: Department of Civil and Coastal Engineering, University of Florida.

Sheng, Y. P., Alymov, V., & Paramygin, V. A. (2010a). Simulation of storm surge, wave, currents,

and inundation in the Outer Banks and Chesapeake Bay during Hurricane Isabel in 2003: The importance of waves. *Journal of Geophysical Research*, *115*(C4), C04008.

Sheng, Y. P., Zhang, Y., & Paramygin, V. A. (2010b). Simulation of storm surge, wave, and coastal inundation in the Northeastern Gulf of Mexico region during Hurricane Ivan in 2004. *Ocean Modelling*, *35*(4), 314–331.

Sheng, Y.P. and Liu, T. (2011), Three-dimensional simulation of wave-induced circulation: Comparison of three radiation stress formulations, *J. Geophys. Res*., 116, C05021, doi:10.1029/2010JC006765.

Sistermans, P. G. J. (2001). Multi-Fraction Net Sediment Transports by Irregular Waves and a Current. *Proceedings of 4th Conference on Coastal Dynamics* (pp. 588–597). Presented at the Coastal Dynamics '01, American Society of Civil Engineers.

Sistermans, P.G.J. (2002). *Graded sediment transport by non-breakingwaves and a current* (Ph.D. Dissertation). Delft University of Technology, Delft, The Netherlands.

Sleath, J. F. A. (1977). *Sediment transport by waves* (No. CUED/A-Hydraulics/TR1). Cambridge, England: Engineering Department, University of Cambridge.

Smith, J. D., & McLean, S. R. (1977). Spatially Averaged Flow Over a Wavy Surface. *Journal of Geophysical Research*, *82*(12), 1735–1746.

Soulsby, R. (1997). *Dynamics of Marine Sands: A Manual for Practical Applications*. Thomas Telford.

Soulsby, R. L., & Whitehouse, R. J. S. (2005). *Prediction of ripple properties in shelf seas-Mark 2 Predictor* (Technical Report No. TR 150). Wallingford, UK: HR Wallingford. Retrieved from http://eprints.hrwallingford.co.uk/281/

Spalding, D. B. (1972). A novel finite difference formulation for differential expressions involving both first and second derivatives. *International Journal for Numerical Methods in Engineering*, *4*(4), 551–559.

Spasojevic, M., & Holly, J. (1994). *Three-Dimensional Numerical Simulation of Mobile-Bed Hydrodynamics* (Technical Report No. 367). The University of Iowa, USA: Iowa Institute of Hydraulic Research.

Steetzel, H. J. (1987). *Systematic investigation of dune revetments* (No. H298-I). The Netherlands: Delft Hydraulics, Delft.

Strickler, A. (1923). *Beitraezo zur Frage der Gerschwindigheits Formel und der Rauhigkeitszahlen fuer Strome kanale und Geschlossene Leitungen*. Mitteilungen des

Eidgenossischer Amtes fuer Wasserwirtschaft, Bern.

Struiksma, N., Olesen, K. W., Flokstra, C., & De Vriend, H. J. (1985). Bed deformation in curved alluvial channels. *Journal of Hydraulic Research*, *23*(1), 57–79.

Thuc, T. (1991). *Two-dimensional morphological computations near hydraulic structures* (Ph.D. Dissertation). Asian Institute of Technology, Bangkok, Thailand.

Ting, F. C. K., & Kirby, J. T. (1994). Observation of undertow and turbulence in a laboratory surf zone. *Coastal Engineering*, *24*(1–2), 51–80.

Toffaletti, F. B. (1968). *A procedure for computation of the total river sand discharge and detailed distribution, bed to surface* (No. 5). Vicksburg, MS: US Army Corps of Engineers.

van der A, D. A., Ribberink, J. S., van der Werf, J. J., O'Donoghue, T., Buijsrogge, R. H., & Kranenburg, W. M. (2013). Practical sand transport formula for non-breaking waves and currents. *Coastal engineering*, 76, 26-42.

van der Hout, G. (1997). *Grain-size and gradation effects on sediment transport under sheet flow conditions, Part 2: data analysis and modeling* (No. Z2137). The Netherlands: Delft Hydraulics, Delft.

van Niekerk, A., Vogel, K. R., Slingerland, R. L., & Bridge, J. S. (1992). Routing of Heterogeneous Sediments over Movable Bed: Model Development. *Journal of Hydraulic Engineering*, *118*(2), 246–262.

van Rijn, L. C. (1984a). Sediment Pick-Up Functions. *Journal of Hydraulic Engineering*, 110(10), 1494 – 1502.

van Rijn, L. C. (1984b). Sediment Transport, Part I: Bed Load Transport. *Journal of Hydraulic Engineering*, 110(10), 1431–1456.

van Rijn, L. C. (1984c). Sediment Transport, Part II: Suspended Load Transport. *Journal of Hydraulic Engineering*, 110(11), 1613–1641.

van Rijn, L. C. (1986). Sedimentation of dredged channels by currents and waves. *Journal of Waterway, Port, Coastal, Ocean Engineering*, 112, 541-559.

van Rijn, L. C. (1987). *Mathematical modelling of morphological processes in the case of suspended sediment transport*. Delft Hydraulics Communication No. 382, The Neverlands.

van Rijn, L. C. (1993). *Principles of sediment transport in rivers, estuaries and coastal seas*. Aqua Publications.

van Rijn, L. C., & F. J. Havinga. (1995). Transport of fine sands by currents and waves. *Journal of Waterway, Port, Coastal, and Ocean Engineering*, 121(2), 123-133.

van Rijn, L. C., & Walstra, J. R. (2003). *Modelling of sand transport in DELFT3D* (Technical Report No. Z3624). The Netherlands: WL Delft Hydraulics.

van Rijn, L. C. (2007a). Unified View of Sediment Transport by Currents and Waves. I: Initiation of Motion, Bed Roughness, and Bed-Load Transport. *Journal of Hydraulic Engineering*, 133(6), 649–667.

van Rijn, L. C. (2007b). Unified View of Sediment Transport by Currents and Waves. II: Suspended Transport. *Journal of Hydraulic Engineering*, 133(6), 668–689.

van Rijn, L. C. (2007c). Unified View of Sediment Transport by Currents and Waves. III: Graded Beds. *Journal of Hydraulic Engineering*, 133(7), 761–775.

Walters, R. A., & Cheng, R. T. (1979). A two-dimensional hydrodynamic model of a tidal estuary. *Advances in Water Resources*, *2*(0), 177–184.

Walstra, D.J.R., Roelvink, J.A., and Groeneweg, J. (2000). Calculation of wave-driven currents in a 3D mean flow model. *Proceedings of 27th International Conference on Coastal Engineering*, Sydney, Australia, pp.1050-1063.

Wang, S. S. Y., & Adeff, S. E. (1986). *Three*-dimensional modeling of river sedimentation processes. *Proc. 3rd Int. Symp. on River Sedimentation*. University of Mississippi, USA.

Warner, J. C., Sherwood, C. R., Signell, R. P., Harris, C. K., & Arango, H. G. (2008). Development of a three-dimensional, regional, coupled wave, current, and sediment-transport model. *Computers & Geosciences*, *34*(10), 1284–1306.

Watanabe, A., & Isobe, M. (1990). Sand Transport Rate Under Wave-Current Action (pp. 2495–2507). Presented at the *Coastal Engineering* (1990), ASCE.

Wechsler, B. A., & Cogley, D. R. (1977). *A Laboratory Study of the Turbidity Generation Potential of Sediments to be Dredged.* (Technical Report No. D-77-14). Vicksburg, MS: U.S. Army Corps of Engineers, Waterway Experiment Station.

Williams, J., Rose, C., van Rijn, L.C. (1999). Suspended sediment concentration profiles in wave-current flows. *Journal of Hydraulic Engineering*, 125(9), 906–911.

Wu, W. (1991). *The study and application of 1-D, horizontal 2-D and their nesting mathematical models for sediment transport* (Ph.D. Dissertation). Wuhan University of Hydraulic and Electric Eng., Wuhan, China.

Wu, W., & Wang, S. S. Y. (1999). Movable Bed Roughness in Alluvial Rivers. *Journal of Hydraulic Engineering*, *125*(12), 1309–1312.

Wu, W., Rodi, W., & Wenka, T. (2000a). 3D numerical modeling of flow and sediment transport in open channels. *Journal of hydraulic engineering*, *126*(1), 4–15.

Wu, Weiming, Wang, S. S. Y., & Jia, Y. (2000b). Nonuniform sediment transport in alluvial rivers. *Journal of Hydraulic Research*, *38*(6), 427–434.

Wu, W, & Wang, S. S. Y. (2006). Formulas for sediment porosity and settling velocity. *Journal of hydraulic engineering*, *132*(8), 858–862.

Wu, W.. (2007). *Computational River Dynamics*. Taylor & Francis.

Wu, W., Sanchez, A., & Zhang, M. (2011). An implicit 2-D depth-averaged finite-volume model of flow and sediment transport in coastal waters. *Proceedings of the International Conference on Coastal Engineering*, *1*(32), sediment.23.

Wu, W. (2014). "A 3-D phase-averaged model for shallow water flow with waves in vegetated water." *Ocean Dynamics*, 64(7), 1061-1071.

Xia, H., Xia, Z., & Zhu, L. (2004). Vertical variation in radiation stress and wave-induced current. *Coastal Engineering*, *51*(4), 309–321. doi:10.1016/j.coastaleng.2004.03.003

Xie, L., Wu, K., Pietrafesa, L., & Zhang, C. (2001). A numerical study of wave-current interaction through surface and bottom stresses: Wind-driven circulation in the South Atlantic Bight under uniform winds. *Journal of Geophysical Research*, *106*(C8), 16841–16,855.

Yalin, M. S. (1972). *Mechanics of sediment transport*. Pergamon Press.

Zhang, R. J. (1961). *River Dynamics*. Beijing, China: Industry Press.

Zhu, J. 1991, A low diffusive and oscillation-free convection scheme. *Communication in Applied Numerical Methods*, 7, 225–232.

Zyserman, J. A., & Fredsøe, J. (1994). Data Analysis of Bed Concentration of Suspended Sediment. *Journal of Hydraulic Engineering*, *120*(9), 1021–1042.

VITA

Qianru Lin was born in Guangzhou, China, on Octorber, 1984. She earned a Bachelor of Science in Environmental Science from Sun Yat-sen University, Guangzhou, China, in 2007 and a Master of Science in Engineering Science from the University of Mississippi in 2010.